Astroglial NMDA receptor signaling mediates fast calcium microdomains and modulates cortical neuron activity

Noushin Ahmadpour

A Thesis submitted to the Faculty of Graduate Studies of The University of Manitoba in partial fulfilment of the requirements of the degree of

Master of Science

College of Pharmacy

Rady Faculty of Health Sciences

University of Manitoba

Winnipeg

Abstract

Astrocytes express different neurotransmitter receptors that serve to integrate these cells into neuronal networks. Many of these receptors, when sensing neuronal activity, induce elevations in intracellular astrocyte Ca^{2+}, which leads to the release of gliotransmitters that modulate nearby neurons. Ionotropic N-methyl-D-aspartate (NMDA) receptors are found on astrocytes and are activated by glutamate and D-serine or glycine, and conduct Ca^{2+} into astrocytes. In brain slices, astrocyte NMDAR activation causes depolarization and Ca^{2+} elevations. However, its role in astrocytes Ca^{2+} transients and feedback modulation to neurons *in vivo* is not characterized. Therefore, in this study, we used a novel NMDAR knockdown (KD) construct to reduce NMDAR expression specifically in cortical astrocytes. Then, using dual calcium imaging of astrocytes and neurons, each expressing a unique genetically encoded calcium indicator (Lck-GCaMP6f and RCaMP1.07 respectively), we determined the impact of astrocytes NMDARs on astrocytes Ca^{2+} transients and nearby neuronal activity. Two-photon microscopy of the barrel cortex of awake mice revealed that NMDAR KD reduces fast and delayed Ca^{2+} microdomains evoked by whisker stimulation in astrocytes. Astrocytic NMDAR KD also reduces overall neuronal response to whisker stimulation which was reflected as animals impaired sensory discrimination ability.

This study for the first time, highlights the importance of NMDAR in astrocyte stimulation-evoked Ca^{2+} microdomains and provides evidence for involvement of astrocytic NMDAR in cortical network activity. This work contributes to a deeper knowledge of mechanisms underlying astrocyte Ca^{2+} microdomains and their integration in cortical circuits, and provides novel directions to study the role of astrocytes in neuronal networks.

Acknowledgment

First, I would like to express my gratitude to my supervisor, Dr. Jill Stobart whose fascination for, and knowledge of astrocytes, along with her support, guidance, and patience made this thesis possible. I am thankful to you for providing me with all the exciting hands-on experience and valuable opportunities that helped me grow professionally and personally. Thank you for always being available and supportive no matter when. For patiently reading through my endless drafts and help me improve as a science enthusiast. Lastly, thank you for always being friendly and having a smile on.

I would also like to sincerely thank my advisory committee members Dr. Mike Jackson and Dr. Lucy Marzban whose thoughtful and detailed feedback has greatly helped the improvement of this thesis and my scientific thinking.

This project would not be possible without the help of Dr. Mike Stobart who conducted the molecular portion of the study including shRNA construct design and production, FACS and qPCR of sorted astrocytes. Mike has been a pillar of the lab over the last years. I want to sincerely thank you for all your help and support. Thank you for always being available to fix issues and for sharing your valuable experience and lab tips with me.

I would like to thank Meher Kantroo who conducted the immunohistochemistry experiments of this study.

Thank you to all my amazing lab mates, Jessica, Meher, Shahin, and Bruno and all the summer students whose friendship, positive attitude and support has always been so encouraging. I feel grateful for being surrounded by such generous and supportive people over the past few years.

My amazing friends also deserve my thanks; they always believed in me, supported me, and helped me through tough times.

Lastly, I would like to thank my family for their unconditional love and support. Thank you for always patiently listening to my frustrations and encouraging me to keep trying to be a better person. For always believing in me when I don’t. I dedicate this to you; mom, dad, and Nilou.

Table of contents

List of figures

Introduction

Results

List of tables

1. Introduction

1.1 Astrocytes; A general introduction

Astrocytes are defined as a densely ramified class of central nervous system (CNS) glial cells originating from the ectoderm and neuroepithelium. These bushy cells exhibit a specialized structure and highly organized distribution throughout the CNS which makes them well-suited not only for their housekeeping functions in the brain such as maintaining the ionic, metabolic, and neurotransmitter homeostasis at synapses [1], but also for their modulatory role in neuronal activity [2–4] and regulating blood flow [5].

Despite the name 'astrocyte' that suggests a star-like shape as the typical morphological feature of these cells, most astrocytes are not star-shaped. In fact, the basis for this classic assumption is the labeling of main astrocytic intermediate filament protein, glial fibrillary acidic protein (GFAP) as an astrocyte specific marker. However, GFAP expression is highly heterogeneous throughout the astrocyte structure and across different brain regions, such that the star-like shape is not always present (Figure 1A). Astrocytes are the most diverse class of glial cells composing multiple sub-classes each with unique morphology [6], gene expression profile, physiological and functional features [7,8]. However, they share the functional properties of maintaining CNS homeostasis at all levels. The most abundant sub-class of astrocytes are protoplasmic astrocytes present in the grey matter in brain and spinal cord. In this thesis, the term "astrocyte" refers to the protoplasmic sub-type while "astroglia" is used to refer to any of the various sub-types.

The astrocyte structure is composed of three major compartments including soma, a dense network of processes, and endfoot (Figure 1A,B). The term 'astrocyte process' is an umbrella title usually used to discriminate the fibrous appendages from soma and endfoot. However, processes are composed of sub-compartments; each astrocyte has five to eight major processes known as branches which ramify into finer processes called branchlets from which very fine processes known as leaflets emanate and contact synapses [9] . At the other end of this polarized structure, endfeet which are specialized distal extensions, are in contact with the vasculature [10] (Figure 1B). Therefore, astrocytes establish close connections with synapses and vasculature which provides them with the spatial properties to modulate synaptic activity and blood flow as explained in sections below [6,11,12].

In contrast to their tight connection with synapses and vasculature, astrocytes only overlap with each other at their very peripheral processes by less than 5% of their total volume [13]. In fact, the

dense network of astrocytes fine processes (leaflets) forms polyhedral, non-overlapping territories [10,14] that repetitively occur throughout the gray matter. This organized pattern is assumed to separate the neuropil into precisely manageable portions; synapses under the territory of an astrocyte might be regulated by that specific cell [15]. This is in accordance with the fact that the astrocyte to neuron ratio has increased through evolution from 0.16 astrocytes per neuron in nematodes, *Caenorhabditis elegans* in particular, to 0.33 in mice and 1.4 in humans [15,16]. The theory is that more complex neuronal networks require more local modulations [15]. Astrocytes are tightly integrated into neuronal network with each astrocyte soma contacting several neuronal cell bodies (see Results, Figure 1B) and each astrocyte ultra-fine network of processes contacting up to 120,000 synapses in rodent hippocampus [17].

In addition to this ideal structure and organization that facilitates their integration into neuronal networks, the astrocyte membrane composition is also customized to their various functions. Astrocyte membranes are equipped with many of the neurotransmitter receptors, ion channels, and transporters that overlap with those expressed on neurons [1,18]. This allows them to receive and respond to a variety of stimuli, most importantly neurotransmitters. Many of these ion channels and receptors, induce transient increases in intracellular calcium concentrations [12,19]. These calcium signals are considered a unique form of astrocyte excitability which in turn leads to gliotransmission; release of molecules including ATP, D-serine, glutamate, and GABA which bind to their receptors on neurons and change neuronal activity [20–25].

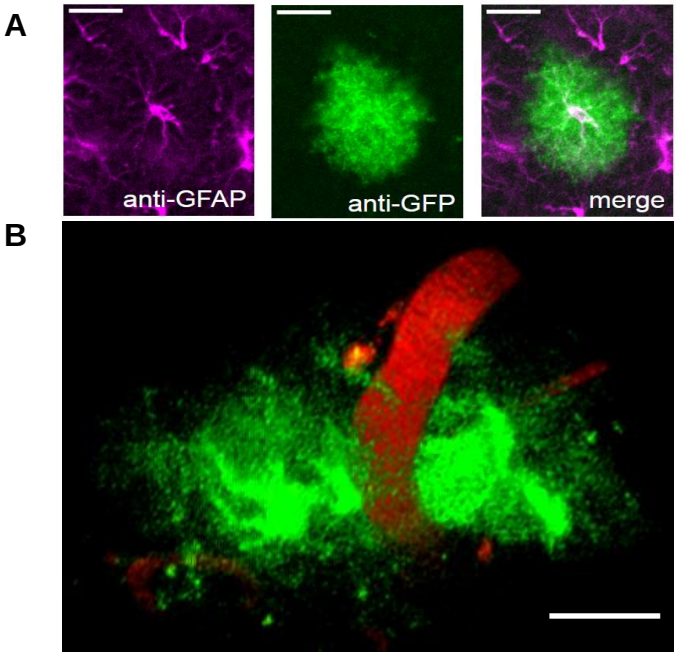

Figure 1. Astrocytes dense bushy network of processes and endfeet. A) Bushy GFP-expressing astrocyte with star-like GFAP staining. B) Two-photon images of cyto-GCaMP labelled astrocyte (green) with endfoot around blood vessel (red). (scale bar = 20um). (Unpublished).

1.2 Functional importance of astrocyte Ca^{2+}

Astrocytes are mainly known to support synaptic homeostasis through the regulation of the local ionic milieu, such as K^+ buffering, and via neurotransmitter uptake [1]. Astrocytes also provide neurons with metabolic support possibly by shuttling lactate as an energy substrate to nearby neurons [26–28], particularly during behavioral arousal states [29]. Besides homeostatic and metabolic support, astrocytes were recently suggested to release gliotransmitters or vasoactive molecules by Ca^{2+} dependent mechanisms which by acting on their corresponding receptors, modulate nearby neuronal activity or blood flow (Figure 2) [6,12]. Gliotransmitters are molecules including glutamate [22], GABA [30,31], ATP [3,4], and D-serine [2], among others, that act on neuronal receptors or nearby astrocyte receptors as a form of glial communication [32]. This suggests that astrocyte Ca^{2+} events greatly contribute to bidirectional astrocyte-neuron interactions that influence neuronal activity from synapses up to complex neural networks.

At the synaptic level, astrocytes modulate basal synaptic activity, excitatory and inhibitory neurotransmission and synaptic plasticity possibly through Ca^{2+}-mediated release of gliotransmitters [2–4,22,33–38]. Astrocytes regulate basal synaptic transmission in the hippocampus [4,34,39,40], through the release of ATP that is metabolized extracellularly to adenosine and activates presynaptic adenosine A1 and A2 receptors decreasing and enhancing neurotransmitter release, respectively[39,40]. Similarly, GABA released from interneurons causes astrocyte activation and ATP/adenosine release, which in turn, enhances excitatory pyramidal neuron inhibition through A1R-mediated $GABA_AR$ gain of function [3]. Ca^{2+} dependent release of glutamate at excitatory synapses increases synaptic strength [36] and enhances synaptic neurotransmitter release [38] and neuronal synchrony [22]. Moreover, astrocytes release D-serine which is an important co-agonist for N-methyl-D-aspartate (NMDA) receptors, that play a role in synaptic plasticity via long term potentiation (LTP) and long term depression (LTD) [2,41,42]. Co-release of D-serine and glutamate from hippocampal astrocytes enhances the induction of heterosynaptic LTD which is important for reversal learning and flexible memory [43]. Ca^{2+}-dependent release of D-serine from hippocampal astrocytes also potentiates LTP induction in excitatory neurons [2]. Glutamate, the main excitatory transmitter of the brain can also be released from astrocytes. Astrocyte-released

glutamate enhances transmitter release, induces LTP in hippocampal synapses [38], and enhances excitatory synaptic strength [36]. Episodic release of glutamate also evokes synchronous activity of neighboring hippocampal neurons through simultaneous activation of extra-synaptic NMDARs [22].

Furthermore, fine astrocytic processes covering synapses can undergo Ca^{2+}-dependent morphological remodeling of their synaptic coverage [44–46]. This potentially can influence gliotransmission and synaptic function [47] by regulating the stability of individual synapses.

Astrocytes are important for regulating tonic blood vessel tone [48], particularly during vasomotion [49]. While brain slice studies suggest astrocyte Ca^{2+} signaling is linked to changes in vascular tone [50–52], there are differential findings in *in vivo* experiments suggesting astrocytes Ca^{2+} events particularly in endfeet may [53–55] or may not [56–58] precede vasodilation during circuit activity.

Astrocytes have the potential to integrate information from multiple synapses to modulate populations of neurons and ultimately influence behaviour. Astrocytes play a regulatory role in neocortical slow oscillations that underlie resting brain waves [59,60], since Ca^{2+} signalling in astrocytes precedes a shift to slow-wave oscillations [60] and induces cortical UP states, where multiple neurons are synchronized during neocortical rhythms [59]. Also, astrocytes dynamically regulate cortical network sensory-evoked Gamma activity in a Ca^{2+}-dependent manner, which is involved in sensory integration and attention [61]. Additionally, robust, global Ca^{2+} events in astrocytes are detected as a result of norepinephrine release from the locus coeruleus [58,62–65]. This suggests that astrocytes may have an important role in network modulation during behavioral arousal states.

Astrocytic gliotransmission has also been linked to behavior. Ca^{2+}-dependent ATP release from astrocytes has anti-depressant effects in mouse models of depression possibly through P2X2 receptors [66]. Interestingly, impaired astrocyte Ca^{2+}-signalling drives autism spectrum disorder-like behaviors such as repetitive behaviors, which is rescued by astrocyte-derived ATP that potentially works through presynaptic P2X2 receptors which facilitate glutamatergic transmission on GABAergic interneurons [67]. Therefore, reduced ATP could diminish inhibitory interneurons activity leading to increased excitability and impaired excitation-inhibition balance [67,68]. Anti-depressant-like effects are also associated with endogenous D-serine which mediates synaptic plasticity through NMDAR-dependent synaptic LTD [69]. These studies support a role for astrocyte integration of higher levels of network function with an impact on behavior through gliotransmission.

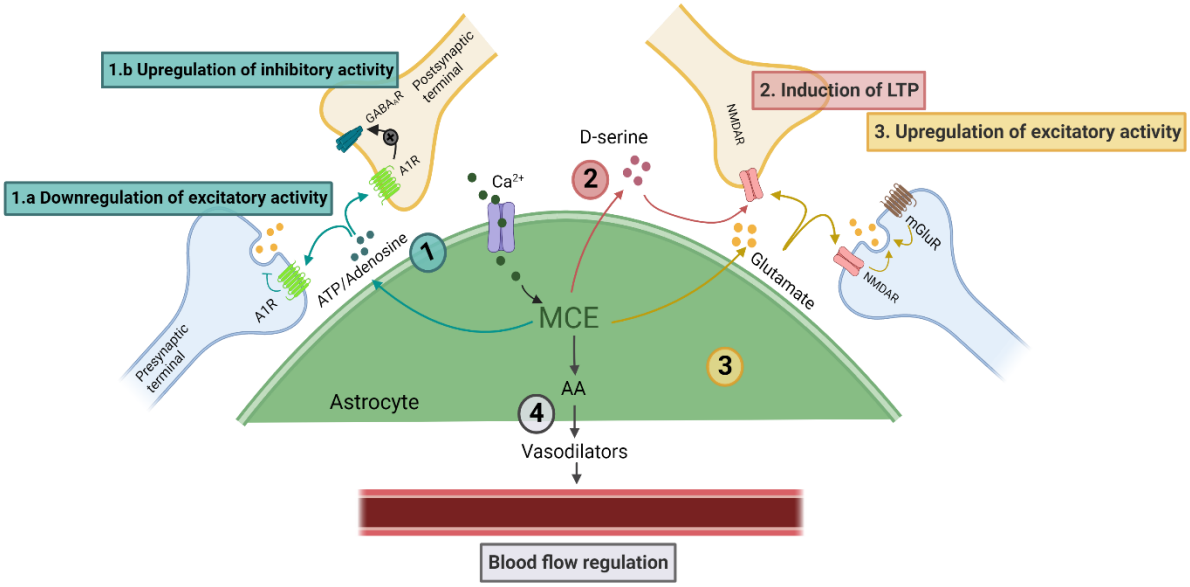

Figure 2. Known functional roles of astrocyte Ca^{2+} events. Ca^{2+} influx generates Ca^{2+} events in the astrocyte leading to gliotransmission of glutamate, D-serine or ATP that is metabolized to adenosine. These gliotransmitters impact nearby neurons: 1) ATP/adenosine at A1 or A2 receptors. For example, adenosine a. downregulates the excitatory activity by activating presynaptic A1R and b. upregulates inhibitory activity by activating postsynaptic A1R which causes a gain a function in $GABA_A$ receptor. 2) D-serine binds to postsynaptic NMDARs and enhances LTP. 3) Glutamate released from astrocytes modulates pre- and post-synaptic neurons, NMDARs and metabotropic glutamate receptors, and increase the excitatory activity. 4) In astrocyte endfeet, MCEs cause the production of arachidonic acid (AA) that is metabolized to vasodilative components, such as prostaglandins, and contribute to regulation of cerebral blood flow. Figure is reproduced from [11].

1.3 Heterogeneous Ca^{2+} events in astrocytes; Calcium dyes vs GECI

Since there are clear associations between astrocyte Ca^{2+} transients and their functional roles in the CNS, a thorough knowledge of the upstream mechanisms that give rise to astrocyte Ca^{2+} signals are necessary. Much work in the astrocyte field has been dedicated to characterizing astrocyte Ca^{2+} events, but there have been technical limitations that have hindered the interpretations of previous findings. Our understanding of mechanisms underlying astrocyte Ca^{2+} events as well as their spatial and temporal characteristics could be categorized into pre- and post-advanced imaging techniques eras. The classical knowledge on these signals was obtained using bulk-loading Ca^{2+} dyes, which are solely able to demonstrate the Ca^{2+} events occurring in astrocytes soma or thick processes but not those localized in fine processes. However, the emergence of compartment-targeting Genetically Encoded Calcium Indicators (GECIs) and *in vivo* optical imaging, particularly two-photon fluorescence imaging, has enabled selective investigation of Ca^{2+} events in specific compartments. The sections below outline the major findings with these two calcium imaging approaches.

1.3.1 Calcium dyes visualize Ca^{2+} transients in somata

Organic calcium indicator dyes have enormously contributed to our knowledge of astrocyte physiology. These dyes such as Fura-2, Indo-1, Fluo-3, Fluo-4, and Calcium Green-1, are small Ca^{2+} chelating fluorescent molecules with membrane permeable acetoxymethyl ester masks which are hydrolyzed by intracellular esterases once delivered. Despite their easy application, broad spectrum of affinities, and commercial availability, these dyes have serious limitations. Firstly, the labeling process with these dyes is not always astrocyte-specific which means that the cells might be unevenly labeled and that additional dyes to specifically label astrocytes, such as sulforhodamine 101, need to be included [10]. The most critical drawback however, is that the organic calcium dyes are only able to report on Ca^{2+} events occurring in the soma or thick processes and fail to detect the transients in finer astrocyte processes [10,70]. This is an issue because the fine processes are the compartments that contact synapses and are potentially responsible for interactions with neurons and vasculature [17,41,71,72]. In other words, bulk loading Ca^{2+} dyes has failed to detect Ca^{2+} events in almost 90% of an astrocyte's area [73]. Membrane impermeable Ca^{2+} indicator dyes have also been delivered to cells via patch pipetting [34,74], which is an improvement compared to bulk loading since it is more cell-specific. However, they also fail to load long, thin processes. Moreover, patch pipetting is an invasive method and may perturb the physiology of the cell [10].

Studies using calcium indicator dyes found that the endoplasmic reticulum (ER) is the main source of Ca^{2+} events in astrocytes, due to upstream G protein-coupled receptors (GPCRs) activation [24,52,75,76]. The most common pathway involves Gq -GPCR Gα subunits that activate phospholipase C-β which hydrolyses phosphatidylinositol biphosphate into inositol triphosphate (IP3) and diacylglycerol. IP3 then activates receptors on the ER membrane, primarily type 2 (IP3R2) which is far more expressed by astrocytes than neurons [77], causing Ca^{2+} efflux into the cytosol.

Different G protein-coupled receptors are expressed by astrocytes including muscarinic acetylcholine receptors, $GABA_{(B)}$ receptors, adrenergic receptors, and metabotropic glutamate receptors (mGluRs) [1], particularly mGluR5, have been widely reported as the major metabotropic receptors underlying Ca^{2+} signals in astrocytes [24,52,75,76]. Pharmacological studies on brain slices from hippocampus and cortex demonstrated that astrocytes Ca^{2+} waves are hindered by mGluRs antagonists [24,52,76] or intracellular Ca^{2+} store depletors [75]. These observations suggest that Ca^{2+} transients are generated by release of Ca^{2+} from intracellular Ca^{2+} stores through mGluRs. However, this was disputed by the finding that the expression of mGluR5 is restricted to juvenile astrocytes [78–80] calling in to question the relevance of this pathway in adulthood. The key role of mGluR in astrocytic Ca^{2+} events was further argued by an ultrastructural study reporting that astrocyte processes close to synapses are devoid of intracellular Ca^{2+} stores and therefore cannot respond to synaptic activity by ER-released waves [81]. The role of intracellular Ca^{2+} pathways in Ca^{2+} events was further debated by finding that knocking out the IP3R2 remarkably reduced the number of astrocyte Ca^{2+} transients [82,83], but did not have a significant impact on neuron excitability, synaptic transmission [83], synaptic plasticity [84], blood flow regulation[56,85], or behavior [86]. This generated controversy in the field, and the contribution of astrocytes to neuronal modulation was debated since perturbations in astrocyte calcium signalling had no effect on neuronal activity. This controversy was strengthened by studies rendering astrocytes as too slow compared to neuronal Ca^{2+} signal onset timescales, a few milliseconds, to modulate rapid processes such as synaptic activity or blood flow [56,63,87–89]. This controversy was alleviated by the emergence of GECIs to measure Ca^{2+} in all parts of the astrocyte, which provided a revolutionary view of astrocyte Ca^{2+} events as described below.

1.3.2 Genetically encoded calcium indicators visualize Ca^{2+} microdomain events

For a comprehensive understanding of astrocytes Ca^{2+} transients and their physiological importance, the complex morphology of astrocytes needs to be taken into consideration. GECIs can be targeted to distinct cell populations with cell-type specific promoters or expressed in desired sub-cellular compartments (e.g. mitochondria, endoplasmic reticulum, or at the plasma

membrane) when tethered to specific localization sequences. The resulting observations via two-photon microscopy demonstrated that Ca^{2+} signals with different features occur in various regions of the astrocyte. In particular, cytosolic GECIs revealed the presence of microdomain Ca^{2+} events (Ca^{2+} MDs or MCEs) that are localized to different parts of the astrocyte cytosol including somata, processes, and endfeet [90–95] and the events have different spatiotemporal characteristics [95]. This view of astrocyte Ca^{2+} transients is quite different from previous studies with organic Ca^{2+} dyes, potentially highlighting the importance of localized transients in fine processes for integrating astrocytes into neuronal networks and bidirectional astrocyte-neuron interactions.

The term “glial microdomain” was first introduced in 1999 and was defined as small highly localized elevations in Ca^{2+} in astrocytes subcellular compartments in response to stimulation, without a tendency to propagate [96]. This argued the previous notion that astrocyte Ca^{2+} signals originate in the soma and travel through the syncytium. Rather, Ca^{2+} MDs are more localized to these independent compartments modulating a few adjacent synapses [96]. Later, studies using GECIs supported and further investigated microdomains [92,97–101]. Targeting GECIs into astrocyte plasma membrane using a membrane targeting dual acylation motif (Lck) from Lck protein tyrosine kinase [102] showed that astrocytes Ca^{2+} transients occur more frequently [96,103–106] and rapidly in fine processes [54,55,103,107]. Moreover Ca^{2+} MDs happen in different spatial and temporal scales [34,55,65,85,95,105,107]. For instance, in astrocytes of the somatosensory cortex, soma-localized Ca^{2+} events show lower amplitude and longer duration while those of processes have higher amplitudes [95]. Moreover, while spontaneous Ca^{2+} transients are short-lasting and spatially localized, transients that occur following neuronal activity evoked by agonist application (in vitro studies) or whisker vibration (*in vivo* studies), are longer-lasting, spatially broader [34], and larger in amplitude [94]. Together, various characteristics observed in Ca^{2+} transients could be suggestive of different underlying signalling mechanisms.

Previous experiments with IP3R2 knock-out mice and organic Ca^{2+} dyes reported that astrocyte Ca^{2+} was completely silenced in this strain [82,83]. However, while GECI-labeled microdomains in IP3R2 knockout mice were strongly reduced in the astrocyte soma, 40% of the Ca^{2+} MDs remained in the processes [65]. This suggests that transmembrane Ca^{2+} entry causes the transients in processes, as opposed to soma transients that are evoked by IP3R2 activation. Also, recent work *in vivo* using membrane-tagged GECIs showed fast Ca^{2+} microdomains in astrocytes processes that are evoked by circuit stimulation and overlap temporally with neuronal Ca^{2+} peaks in both control and IP3R2 knock-out astrocytes [94]. This suggested that fast microdomains are probably not mediated by IP3R2 and therefore GPCR-coupled-mediated pathways. Many of the

GPCR pathways that lead to IP3R2 activation and release of Ca^{2+} form ER are activated by neuromodulators such as norepinephrine and acetylcholine. These cause astrocyte Ca^{2+} transients during behavioural arousal states [58,65,94], but contribute more to large, delayed onset MDs [94]. Together, these data suggests that other pathways, such as extracellular Ca^{2+} influx, may mediate fast onset Ca^{2+} MDs. In this study, we focus on Ca^{2+} influx through a class of ionotropic glutamate receptors.

1.4 NMDA receptor; a class of Ionotropic glutamate receptors

As the major excitatory neurotransmitter, glutamate has a wide range of receptors on both neurons and astrocytes serving as mediators of excitatory transmission [108]. Ionotropic glutamate receptors (iGluRs) are transmembrane ion channels activated by glutamate binding allowing cations to enter the cell. Based on selective agonist binding, iGluRs are categorized into three classes including N-methyl-D-aspartate (NMDA) receptors, α-amino-3-hydroxy-5-methyl-4-isoxazolepropionic acid (AMPA) receptor, and Kainate receptors. The majority of our knowledge about NMDARs comes from studies of these receptors in neurons. Neuronal NMDAR form heterotetramer structures composed of probable combinations of GluN1, GluN2 (A,B,C,D), and GluN3 (A,B) subunits, with GluN1 being the obligatory subunit [109–111]. In neurons, NMDAR activation requires binding of D-serine (or glycine) to GluN1 in addition to glutamate binding to GluN2 [112]. NMDAR is a cationic channel primarily permeable to Na^+ ions however, Ca^{2+} and K^+ also pass through this channel. Upon activation, ion gates are opened enabling the inward flow of the Ca^{2+} and Na^+ ions and outward flow of the K^+. This influx however, is also controlled by voltage, as cell depolarization is needed to detach Mg^{2+} from the pore of the NMDAR [113]. GluN1 is the most conserved and obligatory subunit [114] however, a range of combinations has been found for NMDARs in mammalian neurons each exhibiting different functional features. Depending on the subunits, receptor properties such as glutamate affinity, sensitivity to Mg^{2+}, receptor desensitization, and ion conductance differ [112]. For instance, NMDARs with GluN2C/D subunits exhibit a lower sensitivity to Mg^{2+} block compared to those possessing GluN2A/B [115–119]. Also, GluN3 subunit determines to what extent the receptor is regulated by the Mg^{2+} block [120–122] and is permeable to Ca^{2+} [116,123] as GluN3-containing receptors care less sensitive to Mg^{2+} block and both GluN3A- [120] and GluN3B-containing NMDARs [124] have less permeability to Ca^{2+} .

The first evidence on NMDAR-evoked Ca^{2+} currents in astrocytes was proposed following glutamate application to acutely isolated astrocytes [118]. Although transcripts for all seven subunits have been found in human astrocytes [125], the functional NMDARs in astrocytes are reported to be composed of GluN1, GluN2C or GluN2D, and GluN3 [119]. In terms of physiology, NMDARs on

astrocytes differ from those of neurons due to their lower sensitivity to Mg^{2+} [118,119] and Ca^{2+} permeability [1,112,126], which is likely dictated by their subunit composition. Similar to neurons, astrocytic NMDAR also requires glutamate and D-serine for activation [126]. Multiple studies have observed astrocyte Ca^{2+} transients in cortical slices, particularly in somata, in response to NMDA receptor agonists [119,127–132], and astrocytic NMDAR is shown to mediate important functions as discussed below.

1.4.1 Functional importance of astrocytic NMDAR

NMDAR-mediated Ca^{2+} MDs in astrocytes have functional implications on gliotransmission [128], synaptic strength regulation [133], antioxidant protection [134], and maintaining Ca^{2+} stores [131]. Pharmacological activation of NMDARs in neocortical slices by application of NMDA evokes Ca^{2+} transients in astrocytes followed by ATP release. Astrocyte-released ATP acts on nearby pyramidal neuron purinergic P2X receptors and evokes excitatory currents, which in turn impairs synaptic inhibitory signalling [128] (Figure 3). Astrocyte NMDAR Ca^{2+} signalling could be important for regulation of synaptic strength. In hippocampal slices, astrocyte NMDARs promote presynaptic variability through maintaining paired-pulse ratio (PPR) heterogeneity, which is seen between two presynaptic neurons that target the same postsynaptic neuron. Patch-application of BAPTA or NMDARs antagonist, MK-801, as well as knockout of GluN1 subunit of NMDAR decreased the paired-pulse ratio heterogeneity in hippocampal slices [133]. Such NMDAR-mediated astrocytic regulation of synaptic strength is mediated by a layer-specific role of NMDAR GluN2C subunit. NMDAR GluN2C subunit function effectively keeps stronger synapses stronger and weaker synapses weaker specifically in stratum radiatum [135]. Moreover, activation of astrocytic NMDA receptors may contribute to neuronal protection against oxidative stress. NMDA-induced delayed and sustained somatic Ca^{2+} transients which are mediated by ER release of Ca^{2+}, upregulate the Cdk5/Nr2f pathway, a key regulator in maintaining cell antioxidant machinery. Upregulation of this pathway increases the release of glutathione precursors from astrocytes, which are used by nearby neurons to synthesize glutathione, an important antioxidant [134]. Also, activation of astrocytic NMDARs during theta burst cortical activity decreases free Ca^{2+} in astrocytes through elevation of store uptake [131]. Therefore, NMDAR might regulate basal astrocyte Ca^{2+} concentrations, which has implications for Ca^{2+} microdomain activity and their dynamics such as their amplitude and peak frequency [136,137].

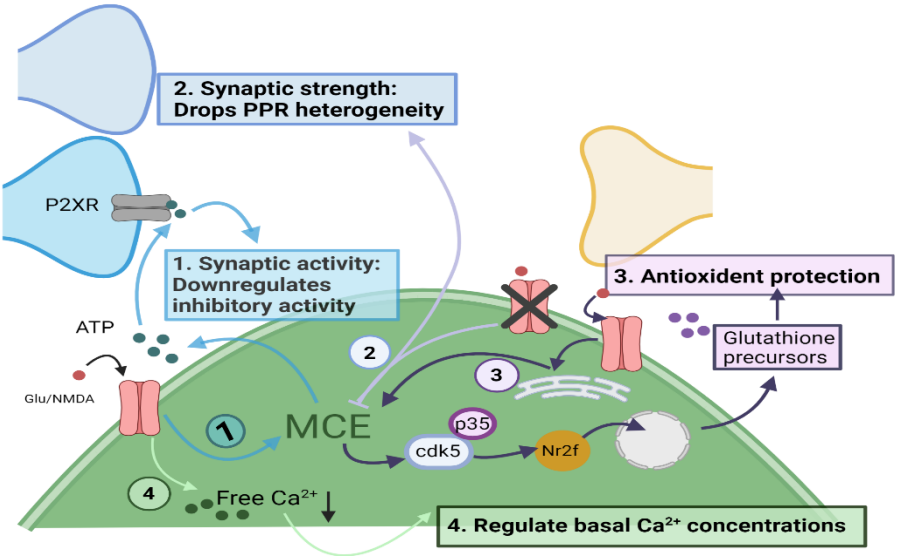

Figure 3. Functional implications of astrocyte NMDA receptors. The following may occur as a result of NMDAR activity, possibly via astrocyte calcium events: 1) Modulation of synaptic activity; ATP gliotransmission is evoked that acts on presynaptic P2XRs and thus downregulates inhibitory activity. 2) Regulation of synaptic strength: abolishing NMDAR-mediated Ca^{2+} MDs decreases the paired-pulse ratio variability 3) Protection of neurons against antioxidant stress; NMDAR activation causes endoplasmic reticulum-mediated Ca^{2+} MDs that upregulate expression of cdk5/p35. This promotes translocation of Nr2f to the nucleus and upregulates expression of glutathione precursors. Neuron use these released glutathione precursors to protect against antioxidative stress. 4) Regulation of basal astrocyte Ca^{2+} concentrations which can define Ca^{2+} MDs characteristics such as amplitude and peak frequency. Figure is reproduced from [11]**.**

Altogether, this picture suggests an important role for of NMDARs in astrocytes Ca^{2+} fast MDs with potential functional implications. However, the possible contribution of NMDAR to stimulation-evoked Ca^{2+} MDs in awake animals has yet to be investigated. In this study, we focused on an area of somatosensory cortex that is responsible for whisker information processing, called the whisker barrel cortex. As this study investigates the impact of reduced expression of astrocytic NMDAR on astrocytes, neurons, and overall circuits of this area, a general overview of whisker barrel cortex structure and function is necessary for better understanding the results and their potential meaning.

1.5 Barrel cortex neuronal structure

Rodents palpate objects in their environment by moving their whiskers back and forth at high frequencies (5-100 Hz), collecting spatial and textural information. Sensory information collected by whisker deflection is transferred to the brainstem and thalamus through glutamatergic synapses and it ultimately reaches the barrel cortex. The whisker barrel cortex which occupies almost 70% of the somatosensory cortex in rodents is an area that is responsible for processing the sensory input arriving from the whiskers. As the somatotopic map of whisker somatosensory cortex suggests, the topographic arrangement of whiskers on the snout of the animal is replicated in the brain as large scale (~200-300 µm) structures called barrels, which are clusters and columns of aggregating neurons responsible for each whisker [138,139].

Mechanosensitive nerve endings of primary sensory trigeminal ganglion neurons in the whisker follicle sense the whisker deflection and innervate the neurons in the whisker-related principal trigeminal brainstem nucleus [140]. These neurons send large excitatory inputs to neurons in the primary whisker somatosensory thalamus, the ventral posterior medial nucleus (VPM). Excitatory VPM neurons then individually innervate single barrels [141]. Each barrel column can be divided into different cortical layers including layer 1 (L1), the most superficial layer, to layer 5 and layer 6 (L5 and L6), the deepest layers. While L1 only contains inhibitory neuronal somata and other synaptic connections, all other layers contain both inhibitory and excitatory neuronal somata. Layer 4 (L4) receives the most prominent excitatory input from VPM. Excitatory neurons of each barrel in L4 then branch into the same barrel in superficial layers 2 and 3 which is referred to as L2/3 as there is no clear architectural boundaries separating them [142,143]. VPM and L4 inputs also arrive at L5 and L6. Such architecture leads to spatially localized whisker-evoked signals [144]. While deeper layers, L5 and L6, are mainly responsible for sending outputs to structures below cortex including thalamus and brain stem, L2/3 cells reciprocally interact with other neocortical regions and therefore provide a hot spot for integration of information across the neocortex [145]. By combining two-photon calcium imaging with awake head-restrained behaviour tasks, it is now possible to study the importance of L2/3 in integration of sensory information and sensory perception.

Sensory information is processed in the whisker barrel cortex microcircuits where a variety of inputs from different thalamus nuclei, other cortical areas, and neuromodulatory inputs converge [145,146]. The majority (~80%) of neurons in barrel cortex layer 2/3 (L2/3) are excitatory pyramidal neurons that release glutamate onto their synaptically connected neurons [143]. Although almost all of these excitatory neurons receive whisker stimulation-evoked excitatory inputs, only a small group (~10%) of these neurons fire robust action potentials in response to whisker stimulation

which are sufficient to reliably represent the sensory stimuli. This phenomenon, known as sparse coding, is possible by fast recruitment of inhibitory GABAergic neurons which compose the rest of the neurons in L2/3 (~20%). GABAergic neurons in L2/3 can be categorized into three main classes based on their molecular profile: Fast-spiking Parvalbumin-expressing neurons (PV), non-fast-spiking ionotropic serotonin receptor 5-HT_{3A}R and nicotinic acetylcholine receptor-expressing neurons (5-HT_{3A}R), and somatostatin-expressing neurons (SST). 5-HT_{3A}R neurons are likely to include two subclasses of GABAergic neurons including the neurogliaform cells and vasoactive intestinal peptide-expressing neurons which are the most studied sub-class of non-fast-spiking GABAergic neurons [145–149]. Almost 10% of excitatory pyramidal neurons form synapses with other nearby pyramidal neurons while they connect with inhibitory neurons at a higher rate. The connectivity between inhibitory neurons is also higher than that of excitatory neurons. Pyramidal, PV, and 5-HT_{3A}R neurons have correlated membrane potential fluctuations and are overall in tune with each other. Therefore, a precise balance between excitatory and inhibitory inputs is crucial for normal circuit function and sensory perception [145,146,150].

1.6 Summary

Studying the role of NMDAR in astrocytes Ca^{2+} signalling to date, has been focused on big soma-localized Ca2+ events and not small Ca2+ MDs localized in processes. This limitation is due to use of loading dyes that mainly label cytosol as opposed to compartment-targeting genetically-encoded Ca^{2+} indicators. Moreover, use of pharmacology in brain slices limits the ability to extract astrocytic NMDAR-mediated responses from those of neuronal NMDARs, particularly when drugs are bath applied. Overcoming these limitations, this study tries to investigate the yet-to-be-known role of astrocytic NMDARs in Ca^{2+} MDs and their relevance *in vivo* for cortical circuit function. Our overall hypothesis is that cortical astrocyte NMDARs are activated during somatosensory stimulation *in vivo* leading to Ca^{2+} MDs needed for the modulation of nearby neuronal activity. This signaling is a necessary component for sensory information processing and behavior. In this thesis, we aimed to address the following questions: *Are astrocyte NMDAR activated by nearby cortical neuron activity evoking astrocyte intracellular* Ca^{2+} *microdomains, particularly with rapid dynamics? Is astrocyte NMDAR signalling important for feedback modulation to neurons and cortical information processing?*

To address these questions, we first reduced the expression of NMDAR in cortical astrocytes by a novel microRNA-adapted shRNA approach, then visualized and recorded cell-specific GECIs labeling whisker stimulation-evoked Ca^{2+} MDs in these cells and their neighboring neurons. We then characterized the Ca^{2+} signals in the presence and absence of NMDAR, in term of their

spatial and temporal dynamics. Finally, we investigated the impact of the absence of NMDARs on sensory perception by conducting whisker-mediated behaviour tasks as outlined below.

2. Materials and Methods

2.1 Animals

All experimental procedures outlined below have been approved by the Animal Care Committee of the University of Manitoba, which is conforming to the Canadian Council on Animal Care. All animals used in this study were C57BL6/J (Table 1). A total of 16 adult mice were used for *in vivo* experiments including 9 males and 7 females. A total of 12 female adult mice were used for brain slice experiments. 9 and 10 adult female mice were used for whisker-mediated discrimination test and novel object recognition test, respectively. 19 female mice were used for fluorescence-activated cell sorting (FACS) and qPCR. For immunohistochemistry, 3 female and 3 male mice were used (for all these mice, one hemisphere was injected with non-silencing and the other was injected with GluN1 KD viral construct). Mice went underwent surgery at the age of 12 weeks to 34 weeks across all experiments. See Table 1 for animals age specific for each experiment. For *in vivo* imaging, animals were trained for head restraint following recovery from surgery for 2-4 weeks and were regularly imaged under two-photon microscope (3-5 times a week) for up to 2 months. At the time of whisker-mediated discrimination task, animals were either 7 or 17 months old. At the time of novel object recognition test, animals were 6 months old. All animals were housed under a standard 12-hr light/dark cycle. Female mice were primarily used for easier handling during animal training. However, male animals were included in immunohistochemistry and in vivo Ca^{2+} imaging to look for any sex differences. We did not observe any sex differences in these experiments therefore, female mice were used for other experiments.

Table 1. Mice line, sex, and age

Experiment	Mouse Line	Number/Sex	Age at the time of surgery	Age at the time of experiment
FACS and qPCR	C57BL6/J	10 Control, 9 GluN1 KD/Female	4-5 months	5-6 months
Immunohistochemistry	C57BL6/J	6 Control, 6 GluN1 KD/3 Male and 3 Female	4 months	6 months
Brain slice Ca^{2+} imaging	C57BL6/J	5 Control, 7 GluN1 KD/Female	5 or 7 months old	7 or 9 months old
In vivo awake Ca^{2+} imaging	C57BL6/J	8 Control; 4 Female and 4 Male / 11 GluN1 KD; 6 Female and 5 Male	3-5 months	3-5 months
Whisker-mediated discrimination task	C57BL6/J	4 Control, 5 GluN1 KD/Female	3-5 months	7 months
Novel object recognition task	C57BL6/J	5 Control; 3 Female and 2 Male/ 5 GluN1 KD; 2 Female and 3 Male	4 months	6 months

2.2 Cloning and virus production

The RCaMP1.07 gene [151,152] was cloned into a plasmid backbone containing adeno-associated virus (AAV2) inverted terminal repeats and the human synapsin (hSYN) promoter [27]. The plasmid was packaged into AAV serotype 9; AAV9-hSYN-RCaMP1.07 by The Vector Core at the University of North Carolina at Chapel Hill (UNC Vector Core). The shRNAmir silencing and non-silencing constructs were custom designed in our lab and packaged in AAV9; hGFAP-chI[3x(shmGrin1)]-Lck-GCaMP6f and hGFAP-chI[3x(shm/rNS)]-Lck-GCaMP6f, by Viral Vector Facility, University of Zurich (Table 2).

Multiple online siRNA prediction sites were used to search for optimized targeting sequences within the mouse GluN1 coding sequence to identify target regions that were consistent between the different algorithms. In the end, 3 target regions (Table 3) were chosen that include the 5' UTR, the ORF and the 3' UTR. The 19nt targets were extended 5' and 3' to a final length of 22 nucleotides and modified to a sense and antisense miR-30-based shRNA sequence according to the rules previously described by Chang et al., 2013 [153]. A non-silencing hairpin derived from the pGIPZ library was used as our control. All sequences were cloned in silico into the optimized MIR-E backbone [154], and subsequently linked together to for a chain of 3 hairpins, separated by a spacer sequence. This shRNA^{mir-e} multimer was encoded within a chimeric intron (chI) sequence between the splice donor and splice acceptor branch point sites. This entire chI-[3X(shRNA^{mir-e})] cassette, along with cloning sites, was synthesized using the ThermoFisher GeneArt Gene Synthesis service. The shRNAmir-e cassettes were digested out of the GeneArt constructs and cloned into a pssAAV-2-hGFAP-Lck-GCaMP6f backbone, generating the pssAAV-2-sGFAP-chI-[3X)shRNA^{mir-e})]-Lck-GCaMP6f. Ligated constructs were transformed into MDS42 E. coli cells by heat shock and grown in Terrific Broth (TB) + carbenicillin with vigorous shaking at 37C for 16 hours. Plasmid was isolated using the PureLink HiPure Plasmid Maxiprep kit (ThermoFisher Scientific), eluted in sterile water, and sequence confirmed (3' end of sGFAP promoter, entire hairpin cassette, and Lck-GCaMP6f). These constructs were packaged in AAV serotype 9 particles by the Viral Vector Core Facility at the University of Zurich. shRNA^{mir} design and cloning was performed by Dr. Mike Stobart.

Table 2. Viral constructs

Serotype	Description	Source
AAV9	hSYN-RCaMP1.07	UNC GTC Core
AAV9	sGFAP-chI[3x(shm/rNS)]-Lck-GCaMP6f	VVF Zurich

AAV9	sGFAP-chI[3x(shmGrin1)]-Lck-GCaMP6f	VVF Zurich

Table 3. shRNA^{mir} sequence

shRNA^{mir} 1	5'-GTTGAGCTGTATCTTCCAAGAG-3'
shRNA^{mir} 2	5'-CTATAGTTGGCAAACTTCCGGT-3'
shRNA^{mir} 3	5'-CTTGATGAGCAGGTCAACGCAG-3'

2.3 Surgery and virus injection

2.3.1 Headpost implantation

The surgery was conducted as previously described [95], in two parts 48-72 hours apart. On the first day, animals were anesthetized with isoflurane (4% for induction, %1.5-2 for maintenance) and were fixed in a stereotaxic frame (RWD; Model 68507). An incision was made along the midline on the shaved skin to expose the skull. After cleaning the bone, we made a headcap using one layer of bonding agent (Bisco Dental; All Bond Universal Adhesive) and a few layers of dental cement (Ivoclar; Tectric EVOFlow) polymerized with blue light. A custom-made aluminum head post was attached to the headcap at the back of the head. The headcap covered all areas of the skull except for the left somatosensory cortex which was later used for craniotomy and virus injection. Animals were given 0.3 ml 5% glucose to help recovery. Animals also received Meloxicam (2mg/Kg; Metacam) every 24 hours for several days after the surgery until they showed complete recovery, and Buprenorphine Slow Release (SR;0.5 mg/Kg) every 72 hours.

2.3.2 Intrinsic optical imaging

Two days after headpost implantation surgery, the somatosensory cortex was mapped using intrinsic optical imaging (IOI) through skull to localize specific whisker areas and identify proper regions for virus injection. Animals were anesthetized with isoflurane (4% for induction and 0.5-1% for maintenance) and head fixed on a platform using the implanted headpost. The skull was washed with sterilized cortex buffer (pH~7.4) to visualize the vasculature below the skull. The solution was then replaced with ultrasound gel (HealthCare Plus) and a small cover slip (5 mm diameter; Fisher Scientific) was placed on top. Images were acquired using a 12-bit CMOS camera (Basler Ace acA2040-55um) focused 300 µm down the cortical surface, under 630 nm illumination. Whisker stimulation (90Hz, 10 s), lateral deflection of a single whisker threaded into a glass capillary affixed to a piezo actuator (PiezoDrive), increased the blood flow to the

corresponding area of the somatosensory cortex which was identified by increased light absorption. IOI was repeated through the cranial window 2-3 weeks after the surgery to acquire a somatotopic map which was used for localization during 2-photon imaging.

Cortex buffer

NaCl	125 mM
KCl	5 mM
glucose	10 mM
HEPES	10 mM
CaCl2	2 mM
MgSO4	2 mM

2.3.3 Virus injection and cranial window implantation

On the second day of the surgery, following IOI, animals were anesthetized with Triple anesthesia including fentanyl (0.05mg/kg), medetomidine (0.5mg/kg), and midazolam (5mg/kg) injected subcutaneously. A craniotomy was cut over the barrel cortex. According to the intrinsic optical imaging map as a reference, using a glass micropipette pulled on a micropipette puller (Sutter Instruments; P97), and a custom-made hydraulic pump, 300 nL of virus mix was injected at 50 nL/min rate at a depth of 400 um into the responding whisker areas. The virus mix included a mixture of AAV9-sGFAP-shRNA-Lck-GCaMP6f ($1x10^{12}$ particles/ml) and AAV9-hSYN-RCaMP1.07 ($2.4x10^{12}$ particles/ml) or GluN1 KD or AAV9-sGFAP-NS-shRNA-Lck-GCaMP6f ($1x10^{12}$ particles/ml) and AAV9-hSYN-RCaMP1.07 ($2.4x10^{12}$ particles/ml) for control animals. A square coverslip (3x3 mm) was lightly pressed on the exposed brain using a stereotaxic arm and fixed with dental cement to the head cap. Animals were given 0.3 ml 5% glucose to help recovery, and antagonist (flumazenil and atipamezole, 0.5mg/kg and 2.5 mg/kg, respectively) to wake up, subcutaneously. Animals were monitored regularly for weight and given diet gel to help recovery. They received Meloxicam (2mg/Kg) every 24 hours for several days after the surgery until they showed complete recovery, and Buprenorphine Slow release (SR) (0.5 mg/Kg) every 72 hours following the surgery up to 3 times.

2.4 Tissue collection and/or dissociation for immunohistochemistry or FACS

Animals were overdosed by intraperitoneal injection of pentobarbital (150 mg/Kg) and fixed on a platform with paws and feet taped to it. An incision was made in the skin to expose the chest cavity. The diaphragm was cut open carefully without piercing the heart. Holding the base of the

sternum, the rib cage was loosened to expose the heart. A butterfly needle (23G) was inserted in the left ventricle and a puncture was made in the right atrium to allow draining off the blood. **In case of FACS**, animals were perfused with 20 ml of Hanks Buffered Salt Solution (HBSS) containing Mg^{2+} and Ca^{2+}, using a 20 ml syringe (20ml/minute). During the perfusion, lungs started to turn white which showed proper conduction of perfusion. Upon perfusion, brain was immediately removed. The injection area, 3 mm* 3mm area under the cranial window, was cut into small pieces and transferred into 2ml tubes containing 0.5 ml ice-cold HBSS. Tissue was then further cut into 0.5-1 mm pieces and placed in $HBSS^{+Ca+Mg}$ (100 mg tissue/ml). Dispase II (final concentration of 0.6U/ml; Millipore-Sigma; D4693) was added and tissue was incubated at 37 °C for 1 hour with gentle shaking (120rpm). Following incubation, tissue was gently dissociated by passing the tissue pieces through a 1ml pipette tip 7 times, followed by passing them through a 40um pipette tip cell strainer (SP Bel-Art Flowmi). Cells were then spun at 400xg at 4°C for 5 minutes. Supernatant was removed and cell were washed twice with ice-cold $HBSS^{+Ca+Mg}$ at 400xg for 5 minutes removing supernatant between each wash keeping the pellet untouched. After the second wash, cells were gently resuspended in ice-cold $HBSS^{+Ca+Mg}$ containing DNaseI (5U; Fisher Scientific; RQ1) and placed on ice until sorted on the FACS. Tissue collection for FACS was performed by Mike Stobart.

Hanks Buffered Salt Solution (HBSS)

NaCl	140 mM
KCl	5 mM
MgCl2 * 6H2O	5 mM
MgSO4-7H2O	0.4 mM
CaCl2	1 mM
Na2HPO4-2H2O	0.3 mM
NaHCO3	4 mM
KH2PO4	0.4 mM
D-Glucose	6 mM

In case of immunohistochemistry, animals were perfused with 20 mL oxygenated aCSF (20ml/minute) followed by 60 ml 2% paraformaldehyde (PFA; Millipore-Sigma; P6148) (in 2X Phosphate-buffered saline (PBS), pH adjusted to 7.2-7.4) using a 20 ml and a 60mL syringe, as well as a three-way valve. Immediately after PFA fixation, animals were decapitated and the brain was removed from the skull, cut into hemispheres in aCSF on ice and transferred to 4% PFA on

ice where it was fixed for 3 hours. Upon fixation, tissue was rinsed by pouring off the liquid and washed by ice-cold 1X PBS, 3 times. Once the tissue was washed, 30% sucrose (in 1X PBS) was added to the tube, and it was stored in 4°C overnight until the tissue sank. Tissue was then embedded in Optimal cutting temperature compound (OCT compound; Tissue Tek) and solidified on dry ice and stored in -80 until used for IHC.

2X Phosphate-buffered saline (PBS)

Stock I	
Na2HPO4 anhydrous	14.2 g
(base) NaCl	79.5 g
dH2O	1000.0 ml
Stock II	
NaH2PO4 monohydrate	13.8 g
(acid) NaCl	79.5 g
dH2O	1000.0 ml
Working solution:	
dH20	800 ml
Stock II	35 ml
Stock I	165 ml

2.5 Immunohistochemistry (IHC)

Fixed tissue was cut on a cryostat (Leica) into 40 um sections and collected in a 24-well plastic dish filled with ice-cold PBS. Prior to staining, sections were washed 2 X 10mins with TBST (Tris-buffered saline+ polysorbate/Tween 20) (0.3% Triton X100) in a 12-well cell culture dish while incubated on a rocking platform at room temperature. Sections were then incubated with TBS + 0.3% Triton X-100 (0.3% TBST) + 5% Donkey Normal Serum (DNS) + IgG Fab blocking reagent (90uL/ml; Jackson Immunoresearch) for 1 hour at room temperature, to prevent nonspecific antibody binding particularly since our primary antibody is produced in mice. Subsequently, sections were washed with TBST for 5 minutes for a total of 3 washes. Finally, sections were incubated in 0.3% TBST + 1% NDS + primary antibodies overnight at 4°C on a rocking platform. In this case, we did a triple staining. The primary antibodies target GFAP, GFP, and NeuN (Table 4). On the second day, sections were washed with 0.05% TBST 3 times for 10 minutes each.

Then, they were incubated with secondary antibodies (Table 5) and 0.05% TBST for 1 hour at room temperature. Following incubation, sections were washed twice with 0.05% TBST (10 minutes each wash) and once with TBS for 10 minutes. Sections were then washed in 0.1X PBS and mounted on glass slides with a coverslip. Images of sections were acquired on a confocal microscope (Zeiss LSM 810). Immunohistochemistry was performed by Meher Kantroo.

Table 4. Primary Antibodies

Primary Antibody	Dilution	Source
Chicken-anti-GFP	1:1000	Aves
Rabbit-anti-mouse/rat-GFAP	1:3000	Dako
Mouse-anti-mouse/rat-NeuN	1:200	Milipore

Table 5. Secondary Antibodies

Secondary Antibody	Dilution	Source
Goat-anti-Chicken-IgG-488	1:1000	Invitrogen
Donkey-anti-Mouse-IgG-647	1:1000	Invitrogen
Donkey-anti-Rabbit-IgG-568	1:1000	Invitrogen

2.6 Sorting astrocytes using FACS

Single cell sorting using FACS machine (BD FACSAriaIII) was conducted by technicians at the Flow Cytometry core facility at the University of Manitoba. Lck-GCaMP fluorescence was used for sorting. To analyze recorded FACS events the FACSDiva (Version 6.1.3) software was used. For each signal, the side scatter was plotted against the fluorescence intensity.

2.7 Quantification of GluN1 expression using qRT-PCR

2.7.1 RNA isolation and amplification

qRT-PCR was performed by Dr. Mike Stobart. Upon sorting, cells were spun at 1000xg for 5 mins, the supernatant removed, and the cells were lysed with 350uL of RNA Purification kit (ThermoFisher) lysis buffer containing βME + 25ng carrier RNA. Cells were resuspended and incubated for 5 minutes with lysis buffer, followed by rapid freezing on dry ice. Lysed cell samples were stored at -80°C until RNA extraction.

We proceeded according to the Purelink RNA Micro Kit (ThermoFisher). Samples were thawed on ice in lysis buffer. Then, tubes were vortexed on high speed for 10 seconds, and passed through a 200ul pipette tip for 10 times. To each tube, 350ul of 70% ethanol was added, vortexed

briefly to mix, and then the entire sample was applied to the PureLink Micro Kit Column and spun at 5,000xg for 1 minute. 350ul wash buffer I was added to each column, and spun through at 5,000xg for 1 minute, followed by addition of 20uL reconstituted and diluted (10uL DNase + 10ul 2X DNase Buffer) PureLink DNase and incubation for 15 minutes at room temperature. Following this, 350uL wash buffer I was added, and tubes were spun at 5,000xg for 15 seconds. Columns were then washed twice with 500ul Wash Buffer II, spun at 5,000xg, and finally spun at 10,000xg for 1 minute. The columns were transferred to RNase-Free 1.5 ml collection tubes and 10ul RNase-Free water was applied to the center of each column. Tubes were incubated for 1 minute, then spun at 10,000xg for 2 minutes to elute.

2.7.2 First Strand cDNA Synthesis

The MessageAmp II aRNA Amplification Kit (ThermoFisher) was used for RNA amplification. From each purified RNA sample, 4ul was transferred to a 0.5 ml RNase-Free tube on ice. To each tube, 4ul of 1st Strand RT mix was added.

1st Strand RT mix

Nuclease-free Water	0.4 µl
T7 Oligo(dt) Primer	0.4 µl
10X First Strand Buffer	0.8 µl
dNTP Mix	1 µl
RNase Inhibitor	0.4 µl
ArrayScript Reverse Transcriptase	0.4 µl

Tubes were flicked to mix, pulse centrifuged, and incubated in a pre-heated 42°C incubator for 2 hours.

2.7.3 Second Strand cDNA Synthesis

Upon completion of 1st Strand cDNA synthesis, 32uL of Second Strand cDNA RT mix was added to each tube.

2nd Strand RT mix

Nuclease-free Water	25.2 µl
10X Second Strand Buffer	4 µl
dNTP Mix	1 µl
DNA Polymerase	0.8 µl
RNase H	0.4 µl

Tubes were gently flicked to mix, and pulse centrifuged. Then the tubes were placed in a thermal cycler, pre-cooled to 16°C and incubated for 2 hours.

2.7.4 cDNA purification

To each sample, 100uL cDNA Binding Buffer was added. Tubes were mixed by pipetting and the entire volume was applied to an assembled cDNA Filter Cartridge. Tubes were spun at 5,000xg for 1 minute, samples were washed with 500uL Wash Buffer and spun at 5,000xg for 1 minute, followed by a final spin at 10,000xg for 1 minute. The Cartridge was transferred to a clean cDNA Elution Tube and 7.5uL of 55°C pre-heated Nuclease-free water was applied directly to each membrane. Tubes were incubated at room temperature for 2 minutes, then centrifuged at 10,000xg for 1 minute.

2.7.5 in Vitro Transcription to Synthesize aRNA

For each sample, 6.4uL of eluted cDNA was transferred to a fresh 0.5 ml RNase-free tube. To each tube, 9.6uL of in Vitro Transcription (IVT) master mix (prepared at room temperature, flicked to mix, and briefly spun) was added.

in Vitro Transcription (IVT) master mix

T7 ATP	1.6 µl
T7 CTP	1.6 µl
T7 GTP	1.6 µl
T7 UTP	1.6 µl
T7 10X Reaction Buffer	1.6 µl
T7 Enzyme Mix	1.6 µl

Tubes were then placed in the reheated PCR machine (37°C). The thermocycler was programmed to incubate at 37°C X 14 hours, followed by cooling to 4°C.

2.7.6 aRNA purification

For purifying aRNA, we used Trizol as opposed to the included columns with MessageAmp II aRNA Amplification Kit (ThermoFisher Life Technologies), as the columns reduce the amount recovered by almost 50%. To each 40uL reaction tube, 500uL Trizol was added and mixed by inversion. Then, 100uL Chloroform was added to each tube and mixed by vigorous inversion for 15 seconds, followed by incubation at room temperature for 3 minutes. The tubes were then

centrifuged at 12,000xg for 15 minutes at 4°C. The upper aqueous phase was transferred to a new 1.5 ml RNase-Free Low Retention Tube (Thermo Scientific) and 250uL Isopropanol was added. Samples were incubated at room temperature for 10 minutes then centrifuged at 12,000xg for 10 minutes at 4°C. The supernatant was removed, and the pellet was washed twice with 500uL 75% Ethanol by spinning at 7,500xg for 5 minutes. Following the second wash and removal of the supernatant, the pellet was allowed to air-dry at room temperature for 5-10 minutes (until all visible drops were gone) and 80uL RNase-Free water was added to each tube.

2.7.7 aRNA reverse transcription

Reverse transcription of aRNA was done according to SuperScript IV VILO (ThermoFisher). 2.5µg of aRNA was reverse transcribed. To each PCR tube, 2.5ug aRNA was added and the volume adjusted to 10uL with RNase-free water. To each tube 10uL of master mix was added:

aRNA reverse transcription master mix

5X SuperScript IV VILO MasterMix	4 µl
Nuclease-free Water	6 µl

Reactions were incubated at 25°C for 10 minutes, 50°C for 1 hour, and 85°C for 5 minutes.

2.7.8 cDNA purification

Reactions were purified using the Qiagen PCR Purification kit. To each reaction, 100 µl of PB buffer was added. Each sample was then applied to a column placed in a 2 ml collection tube (provided by the kit) and spun at 10,000xg at room temperature for 1 minute. The flow-through was discarded and the column was placed back in the collection tube. 750 µl PE buffer was added to each column, tubes were spun at 10,000xg for 1 minute, and the flow-through was discarded. Tubes were spun for another 1 minute to remove the residual wash buffer. Columns were placed in clean 1.5 ml tubes and 50 µl Buffer EB (10 mM Tris·Cl, pH 8.5) was added to the center of the QIAquick membrane. Tubes were centrifuged at same speed and temperature for 1 minute.

2.7.9 RNA analysis using qPCR

Quantitative PCR (qPCR) was done to assess and compare the relative abundance of GluN1 mRNA in astrocytes with GluN1 KD shRNAmir and GluN1 NS shRNAmir. Four sets of primers were used to amplify housekeeping genes. All primers were designed (using NCBI primer blast software) to span exon-exon junctions (Table 6). For each reaction, 5uL (2ng/ul) of cDNA was transferred to a 96 wells plate and reactions were done as in Tables 7 and 8, on a QuantStudio 6

Flex. SYBR Green was used for quantification of PCR products (PowerUp SYBR MasterMix; Life Technologies; A25742). All reactions were done in triplicate.

Table 6. Primers used for qPCR

Primer name	Sequence (5'-3')
MusHPRT F667	ACAGGCCAGACTTTGTTGGA
MusHPRT R765	CACAAACGTGATTCAAATCCCTGA
MusACTB F902	TCCTTCTTGGGTATGGAATCCTG
MusACTB R987	AGGTCTTTACGGATGTCAACG
Atp5pb F	GTCCAGGGGTATTACAGGCAA
Atp5pb R	TCAGGAATCAGCCCAAGACG
Ywhaz F	ATCCCCAATGCTTCGCAACC
Ywhaz R	ACTGGTCCACAATTCCTTTCTTG
MusGluN1 1237F	CAACATCTGGAAGACAGGACC
MusGluN1 1308R	CCAGTCACTCCATCTGCATAC
Tubb3 F	ACCATGGACAGTGTTCGGTC
Tubb3 R	AGCACCACTCTGACCAAAGATA
S100b F	CTTCCTGCTCCTTGATTTCCTCCA
S100b R	CGAGAGGGTGACAAGCACAAG

Table 7. q-PCR set up for assessing relative abundance of GluN1 in astrocytes

Component	Volume
PowerUp	10 µl
Primer Forward (PF)	1 µl
Primer Reverse (PR)	1 µl
cDNA	5uL (2ng/uL)
Water	3 µl

Table 8. Thermocycler program for qPCR

Repetition	Temperature	Time
1	50°C	2 minutes
1	95°C	2 minutes
45	95°C	5 seconds
1	60°C	30 seconds

Analysis was done in QuantStudio 6 Flex software. All samples were gender and age matched (age of injection and days post injection, see table 1). Using Normfinder and Bestkeeper softwares, 3 of the housekeeping genes found to be the most stable were used in the final analysis including Actb, Atp5pb and Hprt. Relative expression of GluN1 gene in GluN1 KD astrocytes was calculated based on previously generated standard curves (8-point dilution series), was

normalized to the expression of the 3 housekeeping genes, and finally compared to the average non-silencing relative gene expression. Results are reported as mean±SEM. Two-sample T-test was used for statistic analysis.

2.8 Cortical slice preparation

Adult female C57BL6/J mice mentioned above were used for brain slice experiments after being used for *in vivo* imaging (will be discussed later). Animals were anesthetized in an induction chamber using isoflurane and decapitated. Brain tissue was removed form the skull and rapidly placed in ice-cold carbogen-saturated slicing buffer. The hemisphere injected with virus was cut and mounted on a vibratome inside a slicing chamber containing the same ice-cold oxygenated buffer. Sagittal slices of 300 um thickness were cut (50 Hz, 1.25 Amp) and transferred to and incubated in previously oxygenated 32°C recovery solution for 1 hour. Before imaging, slices were incubated with oxygenated aCSF containing SR101 (100 nM) for 15 minutes at 32°C for astrocyte labeling.

2.9 Drug application and two-photon Ca^{2+} imaging of brain slices

Slices labeled with SR101 are then placed in the bath under Ultima In Vitro Multiphoton Microscope (Bruker Fluorescence Microscopy) where oxygenated aCSF was constantly flowing (3 ml/min). Lck-CCaMP6f was excited at 930 nm (to include SR101) and a high resolution (512*512 pixels) scanning of the slice was done to identify Lck-GCaMP6f-expressing astrocytes. Once the recording area was determined, a cocktail of neuronal activity blockers including TTX, CNQX, and CdCl2 was bath applied to the slice for 20 minutes. Then, images (256x256 pixels, 2.58 frames per second (fps)) were recorded for 15 minutes where an NMDA and D-serine cocktail was applied for the first 5 minutes and then washed out with aCSF for the next 10 minutes. Another 15-minute image with the same speed and resolution was recorded afterwards while phenylephrine (PE) was applied for the first 5 minutes and washed out using aCSF for the next 10 minutes. Since it takes 3-4 minutes for the buffer to reach the slice and it takes more time for the drug to reach an impactful concentration, the first 5 minutes was considered as baseline and the next 10 minutes was considered as drug application window for the analysis.

NMDG-cutting buffer

NMDG (N-methyl-D-Glucamine)	93 mM
KCl	3 mM
MgCl2 * 6H2O	5 mM
CaCl2 * 2H2O	0.5 mM

NaH2PO4	1.25 mM
NaHCO3	30 mM
HEPES	20 mM
Glucose	25 mM
Sodium Ascorbate	5 mM
Sodium Pyruvate	3 mM

Recovery solution

NaCl	95 mM
KCl	3 mM
MgCl2 * 6H2O	1.3 mM
CaCl2 * 2H2O	2.6 mM
NaH2PO4	1.25 mM
NaHCO3	30 mM
HEPES	20 mM
Glucose	25 mM
Sodium Ascorbate	5 mM
Sodium Pyruvate	3 mM

ACSF (Artificial cerebrospinal fluid)

NaCl	125 mM
KCl	2.5 mM
NaH2PO4	1.25 mM
MgCl2	1 mM
CaCl2	2 mM
NaHCO3	25 mM
glucose	25 mM

Carbogen

Oxygen	95 %
Carbon dioxide	5 %

Neuronal blockers cocktail

TTX (Tetrodotoxin)	1 μM
CNQX (Cyanquixaline)	10 μM

$CdCl_2$	100 µM
Drug cocktail	
NMDA	50 µM
D-serine	10 µM
Phenylephrine	10 µM

2.10 Behavior training

Following full recovery from surgery (usually one week after surgery), animals started to be trained for awake two-photon imaging. Animals were handled twice a day for 3-5 days until they were comfortable being handled with experimenter. Then, they were introduced to the head fixation tube multiple times a day for 3-4 days with being restrained using the implanted head post. Restraint started from several seconds and increased to several minutes as the animal got used to the setup. Finally, when animals were acclimatized to the head fixation tube, they were water-deprived overnight and were presented to the whole awake imaging setup where they are presented with water from a lick spout while their head is restrained, and whiskers being vibrated. Starting with short trials (12.5 seconds), a water drop was presented in sync with an auditory cue at the end of each trial (10^{th} second). The aim was to train the animal to sit still and accept whisker stimulus during the trial and receive water as a reward. The whisker stimulus was presented by threading a single whisker into a glass capillary affixed to a piezo element (T223-H4CL-303X; Piezo Systems) vibrated at 90 Hz. The length and the number of trials were increased to 25 s and up to 50 trials per session, as the animal showed signs of being accustomed to the setup. Animals were trained two sessions a day, 3-5 days a week, for a total time of 2-4 weeks depending on their performance.

2.11 Awake 2-photon imaging

Water-deprived animals were imaged while head-restrained in the water reward task setup under a custom-built two-photon laser-scanning Ultima In Vitro Multiphoton Microscope (Bruker Fluorescence Microscopy) with a 20x water immersion objective (Olympus). The chronic window was cleaned with a damp dental applicator and water and ultrasound gel was applied. RCaMP1.07 and Lck-GCaMP6f were excited at 990 nm with a Ti:sapphire laser and emission light was detected with GaAsP photomultiplier modules (PMTs) with 850/50 nm band pass filter (red) or a 750/70 band pass filter (green). The microscope was controlled by a customised version of Prairie View. At the start of each imaging session, we needed to find fields of view in cortical

layer 2/3 with neurons responding to whisker stimulation according to IOI map. To do that, short trials (12.5 s) with 3 s of whisker stimulation (90Hz) were used (depth 110-280 um). Once the cells were selected, a high resolution (512x512 pixels, 1.17 fps) image was collected of the field of view for reference (the goal was to avoid imaging same cells twice). Then, trials were switched to long 25-second trials including 5 seconds of baseline, 5 seconds of whisker stimulation (90 Hz) followed by 12 seconds without stimulation and fast time series (128*128 pixels; 13.84 fps) were collected. For each field of view, a total of 10 trials were performed including 5 trials without stimulation alternating with 5 stimulation trials. The whisker stimulus was presented by threading whiskers (according to IOI map) into a glass capillary affixed to a piezo element vibrated at 90 Hz. Animals were imaged 3-4 days a week for up to 2 months.

2.12 Image analysis

Image analysis was done as previously described by [95], using ImageJ and MATLAB R2020b (MathWork). For *in vivo* data analysis, neuronal regions of interest (ROIs), neuronal soma, were hand-selected using ImageJ. ROIs within astrocytes processes (*in vivo* and in vitro image analysis) or neuronal dendrites (*in vivo* image analysis) were automatically identified using a custom-designed image processing toolbox for MATLAB (Cellular and Hemodynamic Image Processing Suite (CHIPS) [155]. CHIPS did so by implementing an activity-based algorithm. Active pixels were defined as those that exceed the threshold of mean pixel intensity plus 7 (*in vivo* images, Lck-GCaMP6f AND RCaMP1.07) or 5 (in vitro images, Lck-GCaMP6f) times the standard deviation (SD) of the same pixel during the last 5 seconds and had a peak within 0.07-1 (*in vivo*, RCaMP1.07), 0.1-1s (*in vivo* Lck-GCaMP6f) or 0.1-8 s (in vitro, Lck-GCaMP6f) compared to the last 5 seconds. Active pixels were grouped within space (spatial radius of 4 um) and time (0.2 s for RCaMP1.07 and 0.5 s Lck-GCaMP). The 3D mask of active pixels was summed along the temporal dimension, normalized, and thresholded ($q = 0.2$) to make a 2D activity ROI mask. Raw image data from pixels within each 2D ROI were statistically compared to pixels surrounding the ROI (p value < 0.05 by one-way ANOVA) to exclude false positives. Activity masks created by algorithm and manually selected ROI mask were compared and the overlapping areas were excluded from the activity mask making sure each ROI was unique. Ca2+ MDs thus were defined as ROIs with the minimum area of 4 um^2 and maximum area of 1000 um^2. For each ROI, a signal vector (dF/F) was calculated relative to the baseline fluorescence in the first 5 s of the trial. For each event, different features such as amplitude and peak onset latency were measured and finally exported as .csv files for statistical analysis. The peak onset latency was calculated from the smoothed signal trace (5 frame moving average) as the first time point when the signal went

over the threshold (the mean of the 5 s baseline plus 2.5 times SD) after the start of stimulation. We categorized astrocytes Ca^{2+} events as fast and delayed based on the median onset latency of their respective neurons during stimulation (control; 1.71s and GluN1 KD 1.78s). For all analysis, activities within the stimulation window (0<onset latency<8s) were compared to the equivalent in trials with no stimulation except for fraction of active pixels (Figure 3 G,H) which compared the events during the whole trial.

The amplitude of both control and GluN1 KD neurons Ca^{2+} MDs showed a consistent peak around 1.2 df/f and had a tail of high responsive neurons. The amplitude distribution was described by a log normal distribution (R^2 > 0.95). Therefore, we categorized neurons based on this stable distribution using 98^{th} and 88^{th} percentile of control neurons amplitude: High responding neurons (amplitude≥ 3.47 dF/F), Mid responding neurons (1.92≤amplitude<3.47 dF/F), and low responding neurons (amplitude<1.92 dF/F).

We also used a seed-based correlation analysis to correlate the signal vector (dF/F) for each ROI with the vectors from all other ROIs in the same field of view and examined the mean Pearson's correlation coefficient across each trial within stimulation window (0-8s).

2.13 Behavior tasks

Whisker-mediated discrimination task (WMDT) and Novel Object Recognition Task (NORT) were performed as described by Wu et al., 2013 [156]. Both tasks include two general phases: habituation and testing phase. During the habituation phase, animals were introduced to an empty lab-made arena ($40cm^3$) for 10 minutes a day for two consecutive days. The animal's performance inside the arena was monitored and those with signs of stress (not exploring, spending most if the time in the corners) were excluded from the study. For WMDT, following the last session of habituation, animals were lightly anesthetized using isoflurane (4% induction, 1-1.5% maintenance) and all the whiskers on the whisker plate ipsilateral to the chronic window were trimmed back to the face using fine-tipped scissors. On the contralateral side of the nose, all whiskers except for those corresponding to the virus injection area were also trimmed. During the learning phase, animals were introduced to the arena with two stands (4 cm x 15 cm) covered with the same grade of sandpaper; 150 or 220 (WMDT) or two of the same objects (dark blue bulldogs, 3D-printed at Stobart lab) (NORT), placed in the middle of the arena with an equal distance from each other and walls. Animals were allowed to explore for 5 minutes. After the learning phase, animals were transferred to a resting cage for 5 minutes. During this time, the stands with sandpaper/objects were removed form the arena and two new stand/objects were replaced: one familiar sandpaper/object (exactly same as the one in learning phase) and a novel sandpaper/object

(150P or 220P sandpaper, an orange mouse). During the testing phase, animals were allowed to explore the arena with one familiar and one novel object for 3 minutes. The animal's performance was recorded using a camera. To minimize the impact of olfactory cues, three copies of each object were used. Also, the arena and the objects were cleaned with 70% ethanol between the learning and testing phase (WMDT) and between animals (WMDT and NORT).

2.14 Behavior task analysis

Videos were analysed either manually or using a deep learning software, DeepLabCut [157] which allows for pose estimation of user-defined body parts using deep learning. DLC was first trained with 10 short clips of the learning phase. The trained network was then used to estimate the position of animal's nose as well as the objects in each frame of the video. Finally, a .csv file was created including the position of marked targets across videos. In either case, the amount of time animals spent around each object in each phase was measured. Investigation time was defined as the total time the animal was facing towards the sandpaper/object with their nose being at 2cm or closer to the object. Climbing over the objects or stands was not considered as investigation. Any animal that did not explore any objects in the learning phase, explored only one object in the testing phase, or had a total investigation time of less than 2s in the learning or testing phase was excluded from the analysis. The percentage of time spent investigating the novel sandpaper/object versus the familiar one was defined as discrimination ability. This number was statistically tested against a 50% chance level using one-sample t-test.

2.15 Statistical analysis

All statistics for Ca^{2+} analysis was performed in R (Version 1.2.1335) using the lme4 package for linear mixed-effects models. For *in vivo* Ca^{2+} analysis, our fixed effects included animal type (control or GluN1 KD), stimulus condition (with or without stimulation), astrocyte type (fast or delayed), neuronal populations (High or mid or low responding neurons), and sex (male or female) as well as the interaction of these effects. As random effects, we had intercepts for individual animals, fields of view, ROIs, and trials. For in vitro Ca^{2+} analysis, fixed effects included type (control or GluN1 KD), stimulus condition (Drug or baseline) and the interaction between these two. Random effects included animals. Likelihood ratio tests comparing models with fixed effects against models without fixed effects were performed to determine the model with the best fit while accounting for the different degrees of freedom. All data were reported and plotted as uncorrected means and standard error of the means. p values for different parameter comparisons were obtained using the multcomp package with Tukey post hoc tests. One-sample t-test and two-

sample t-test were performed in Excel (Microsoft office 16) and R (Version 1.2.1335) for qPCR and behavior task respectively.

3. Results

3.1 A novel miRNA-adapted shRNA (shRNA$^{mir\text{-}e}$) construct silences GluN1 expression specifically in astrocytes

To reduce the expression of NMDA receptors in cortical astrocytes, we used a novel miRNA-adapted shRNA construct to specifically knock down the GluN1 subunit which is the essential subunit of NMDAR. This multimer shRNA$^{mir\text{-}e}$ targeted three unique regions in the mouse GluN1 sequence and was cloned into an adeno-associated virus backbone, pssAAV2-sGFAP-Lck-GCaMP6f, to drive the astrocyte-specific expression of a plasma membrane-tagged GECI (Lck-GCaMP6f) as well as silencing GluN1. A non-silencing shRNA^{mir} AAV construct was used as a control (Figure 1A). AAV9 viruses from these constructs (300nl of 1 x10^{12}vg/ml; AAV9-sGFAP-NS-shRNA^{mir}-Lck-GCaMP6f or AAV9-sGFAP-shRNA^{mir}-Lck-GCaMP6f) were injected into the somatosensory cortex of adult C57BL6/J mice (Figure 1A). Immunohistochemistry for GCaMP6f (anti-GFP), astrocytes (anti-GFAP), and neurons (anti-NeuN) showed that both GCaMP AAV constructs co-localized with GFAP and not NeuN, confirming the astrocyte-specifc expression of the constructs (Figure 1B). These GCaMP AAVs did not cause any astrogliosis [94].

To quantify GluN1 expression, astrocytes from dissociated brains were sorted by flow cytometry using their GCaMP6f fluorescent signal (Figure 1 A,C). RNA from the pool of sorted astrocytes showed a 70% reduction in the abundance of GluN1 mRNA by qPCR comparing GluN1 knock down astrocytes relative to controls (Figure 1D).

A

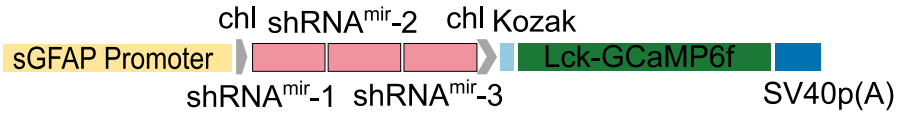

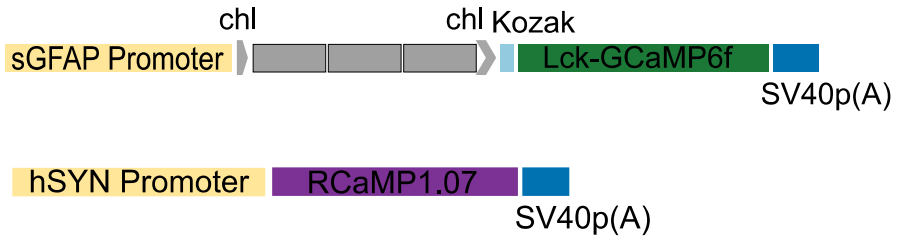

B

AAV9-sGFAP-shRNA^{mir}-Lck-GCaMP6f

AAV9-sGFAP-NS-shRNA^{mir}-Lck-GCaMP6f

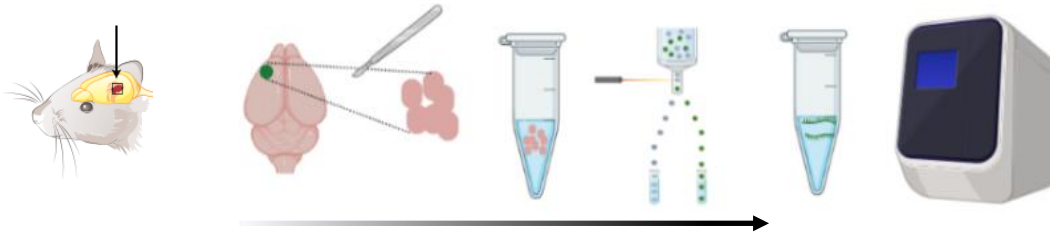

C

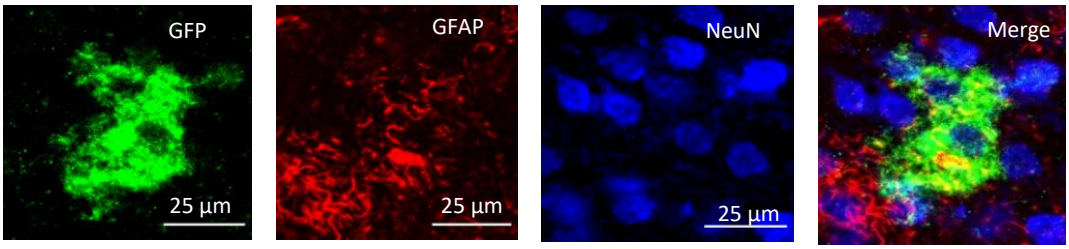

D

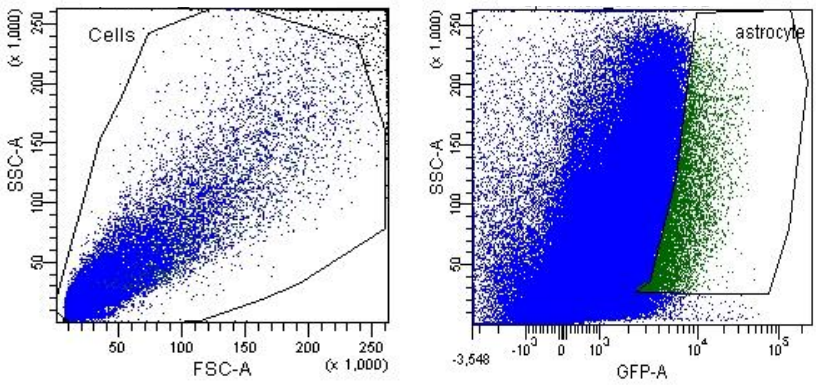

Population	#Events	%Parent	%Total
All Events	1,140,371	####	100.0
Cells	1,043,278	91.5	91.5
astrocyte	4,975	0.5	0.4

E

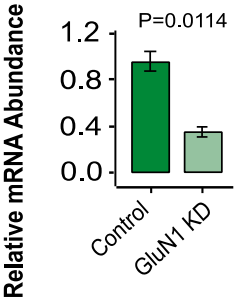

Figure 1. Astrocyte-specific knockdown of NMDA receptor

A) Schematic representation of astrocyte-specific GluN1 KD and non-silencing shRNA^{mir} construct with green membrane-tagged GECI, AAV9-sGFAP-shRNA^{mir}-Lck-GCaMP6f and AAV9-sGFAP-NS-shRNA^{mir}-Lck-GCaMP6f, and neuron-specific red GECI, AAV9-hSYN-RCaMP1.07.

B) During cranial surgery, AAVs were injected in C57BL/6 mice cortices. Tissue from the injection area was collected and used for fluorescence-activated cell sorting and single cell RNA sequencing to study the relative abundance of GluN1 in control and KD astrocytes.

C) Immunohistochemistry shows that Lck-GCaMP6f expression is astrocyte-specific and it (GFP) colocalizes with astrocytes (GFAP) and not neurons (NeuN). Scale= 25µm

D) Example dot plots of astrocytes expressing GFP sorted using FACS. Blue dot show non-fluorescent cells and green dots represent labeled astrocytes which comprise a small portion of all events (bottom).

E) GluN1 KD construct reduces GluN1 mRNA abundance by 70% compared to control non-silencing virus, AAV9-sGFAP-NS-shRNA^{mir}-Lck-GCaMP6f. Abundance is represented as mean ± SEM. P-value is calculated using one-sample t-test. (n= 5 control, and 5 GluN1 KD mice)

3.2 GluN1 KD reduces astrocyte responses to NMDAR agonists

To show a functional reduction in astrocyte NMDAR following GluN1 KD, we examined agonist-induced Ca2+ responses in cortical astrocytes. Acute cortical slices were cut 8 weeks after injection of control or GluN1 silencing AAV constructs into the somatosensory cortex of adult mice. Two-photon imaging of Lck-GCaMP-expressing astrocytes (Figure 1A) revealed that bath application of NMDAR agonists, NMDA (50 uM) and D-serine (10 uM), in the presence of neuronal activity blockers (1uM TTX, 10uM CNQX, 100uM $CdCl_2$), evoked Ca^{2+} events within regions of interest (ROIs; i.e. microdomains) in both control and GluN1 KD astrocytes (Control; Baseline: 1.10±0.15 peaks/ROI/min, NMDA+D-serine: 4.29±0.51 peaks/ROI/min, $p<0.001$ & GluN1 KD; Baseline: 1.17±0.11 peaks/ROI/min, NMDA+D-serine: 2.60±0.23 peaks/ROI/min, $p<0.001$; Figure 2B left, green bar, also Figure 2C left). However, the number of Ca^{2+} responses evoked by NMDA +D-serine in GluN1 KD astrocytes was significantly lower than control cells (2.60±0.23 vs 4.29±0.51 peaks/ROI/min, $p=0.04$; Figure 2C left). Furthermore, the area under the Ca^{2+} trace curve (AUC) for individual MDs was reduced in GluN1 KD astrocytes (Figure 2C right, Figure 2E).

To ensure the astrocytes were viable following GluN1 KD, we bath applied phenylephrine (PE) (alpha-1 adrenergic receptor agonist), a known agonist for release of Ca^{2+} from intracellular astrocyte stores. PE evoked Ca^{2+} events in both control and GluN1 KD astrocytes (Control; Baseline: 1.21±0.19 peaks/ROI/min, PE: 3.43±0.50 peaks/ROI/min, $p<0.001$ & GluN1 KD; Baseline: 1.20±0.17 peaks/ROI/min, PE: 2.93±0.38 peaks/ROI/min, $p<0.001$; Figure 2B right, purple bar, also Figure 2D top), with no significant difference in the number of evoked events (2.93±0.38 vs 3.43±0.50 peaks/ROI/min, Figure 2D top). However, as the trace AUC shows (Figure 2D bottom), Ca^{2+} responses to PE were smaller in GluN1 KD astrocytes compared to controls (Figure 2E). This suggests that there is a potential interaction between astrocytic ionotropic NMDARs and Gq-GPCR signalling.

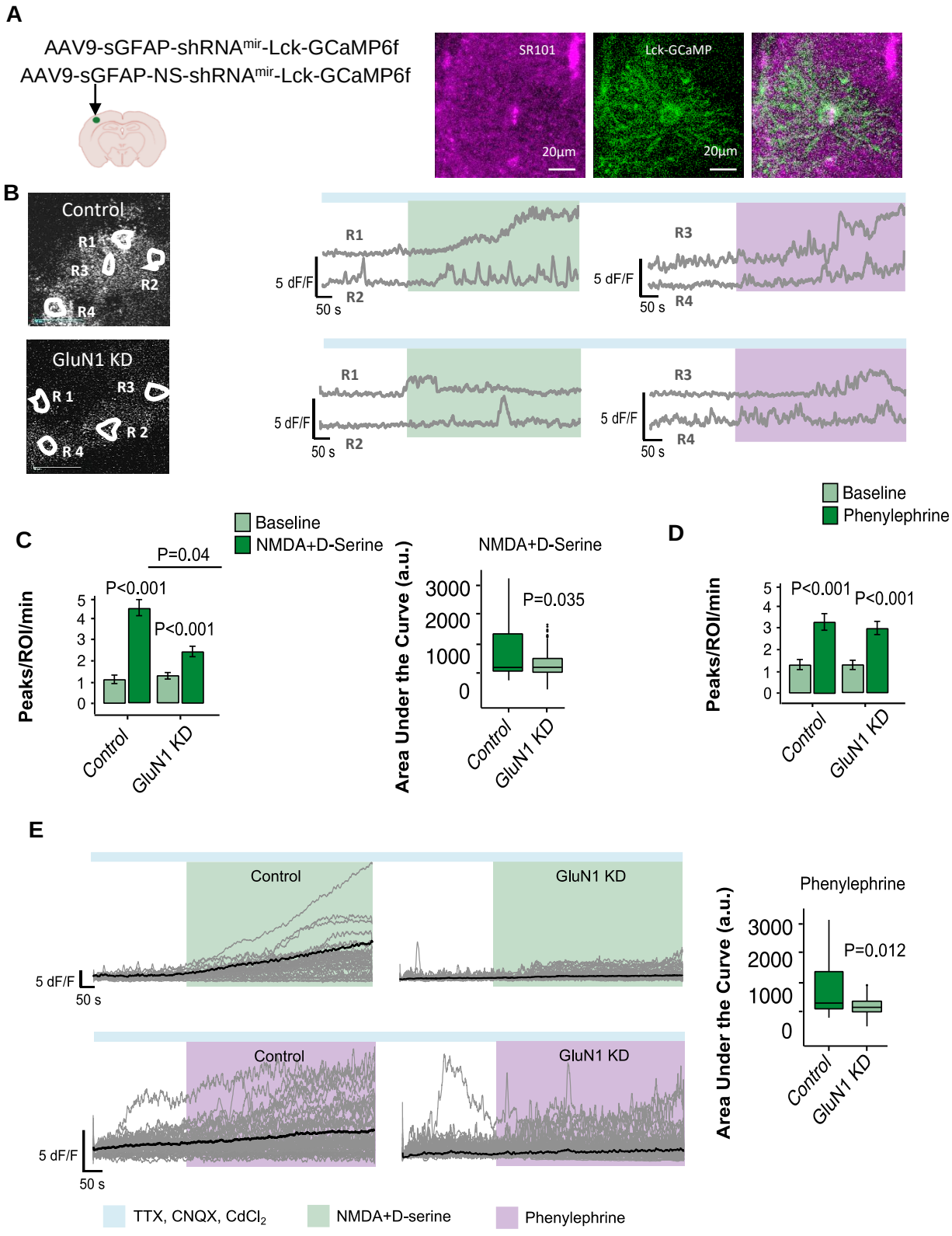
A
AAV9-sGFAP-shRNA^mir-Lck-GCaMP6f
AAV9-sGFAP-NS-shRNA^mir-Lck-GCaMP6f
SR101
Lck-GCaMP
20µm
20µm
B
Control
R1
R3
R2
R4
GluN1 KD
R 1
R3
R 2
R 4
5 dF/F
50 s
C
Baseline
NMDA+D-Serine
P=0.04
P<0.001
P<0.001
Peaks/ROI/min
Control
GluN1 KD
NMDA+D-Serine
Area Under the Curve (a.u.)
P=0.035
D
Baseline
Phenylephrine
P<0.001
P<0.001
E
Control
GluN1 KD
TTX, CNQX, CdCl2
NMDA+D-serine
Phenylephrine
Phenylephrine
P=0.012

Figure 2. Functional reduction in astrocyte calcium responses to NMDAR agonists

A) During cranial surgery, adeno-associated viruses for astrocyte-specific expression of Lck-GCaMP6f and GluN1 KD, AAV9-sGFAP-shRNA^{mir}-Lck-GCaMP6f, together with AAV9-sGFAP-NS-shRNA^{mir}-Lck-GCaMP6f, a non-silencing version as a control, were injected. 3-4 weeks post-injection, brain slices of 300 µm were cut and incubated with SR101 (100 nM) to help localize the GCaMP6f-expressing astrocytes before drug application. Example expression of GCaMP6f in an astrocyte colocalized with SR101 (Right).

B) Example traces from ROIs (example ROIs are named as R1-R4) detected in control and GluN1 KD astrocytes responding to bath application of NMDA (50 µM) and D-serine (10 µM) (green box) (5 minutes baseline, 10 minutes drug application), and phenylephrine (10 µM) (purple box) (5 minutes baseline, 10 minutes drug application) in the presence of a cocktail of inhibitors to block neuronal activity (TTX, CNQX, and CdCl2) (blue bar). Scale= 50 µm

C) Ca^{2+} peaks per ROI per minute (left) and Area Under the Curve (AUC) (right) of traces evoked by NMDA+D-serine in control and GluN1 KD astrocytes. Bar plots are represented as mean ± SEM. (Control: n= 70 traces from 5 slices, 5 mice, GluN1 KD: n= 100 traces from 7 slices, 7 mice)

D) Ca^{2+} peaks per ROI per minute (top) and Area Under the Curve (AUC) (bottom) of traces evoked by phenylephrine in control and GluN1 KD astrocytes. (Control: n= 43 traces from 5 slices, GluN1 KD: n= 59 traces from 7 slices)

E) Traces from Ca^{2+} MDs evoked by bath application of NMDA+D-serine (top) and phenylephrine (bottom). (NMDA+D-serine; Control: n= 70 traces from 5 slices, from 5 mice, GluN1 KD: n= 100 traces from 7 slices, from 7 mice & Phenylephrine: Control: n= 43 traces from 5 slices, from 5 mice, GluN1 KD: n= 59 traces from 7 slices, from 7 mice)

All statistics are calculated using linear mixed model and Tukey post hoc tests.

3.3 GluN1 KD reduces stimulation-evoked Ca^{2+} MDs in astrocytes

To investigate the impact of GluN1 KD on dynamics of Ca^{2+} MDs in cortical astrocytes and neurons *in vivo*, we injected a combination of GECIs into the somatosensory cortex layer 2/3 of C57BL6/J mice prepared with a cranial window. For GluN1 KD animals, a mix of AAV9-sGFAP-shRNA^{mir}-Lck-GCaMP6f and AAV9-hSYN-RCaMP1.07 was injected to drive the astrocyte-specific expression of green membrane-tagged GECI, Lck-GCaMP6f, and the shRNAmir construct to silence the GluN1 expression, as well as neuron-specific expression of red cytosolic GECI, RCaMP1.07. For controls, a mix of AAV9-sGFAP-NS-shRNA^{mir}-Lck-GCaMP6f and AAV9-hSYN-RCaMP1.07 was used to induce the expression of astrocyte specific Lck-GCaMP6f, non-silencing (NS) shRNAmir construct and neuron-specific RCaMP1.07. Following recovery from surgery, animals were trained for accepting head fixation and receiving a water reward to minimize movement for awake imaging. After behavior training, awake animals were imaged under two-photon microscope while specific whiskers were stimulated (vibrated at 90 Hz, 8s) (Figure 3A,B). To analyse the Ca^{2+} signaling data collected from astrocytes and neurons during awake two-photon imaging, regions of interest (ROIs) were either hand-selected (for neuronal somata) or identified by an unbiased algorithm that detects pixels exceeding a certain threshold (see Materials and Methods 2.12 Image analysis) within astrocytes processes and neuronal dendrites[94,158] (Figure 3C). Hand-selected and algorithm-selected ROIs were compared, and the overlapping regions were excluded. Ca^{2+} microdomains (MDs) were detected in astrocyte processes and their surrounding neurons in trials with stimulation and without stimulation in both control and GluN1 KD animals (Figure 3C). Astrocyte Ca^{2+} MDs detected in no stimulation trials are referred to as spontaneous MDs. Importantly, whisker stimulation evoked more Ca^{2+} MDs (ROIs) per field of view (FOV) compared to spontaneous ROIs per FOV in control astrocytes (mean±SEM of 3.21±0.23 vs 2.01±0.12 ROIS/FOV, $p<0.0001$, Figure 3D). However, sensory stimulation failed to increase the ROIs frequency in GluN1 KD astrocytes (2.26±0.17 vs 1.93±0.12 ROIs/FOV, $p=0.56$; Figure 3E). In fact, the number of stimulation-evoked MDs in GluN1 KD astrocytes was significantly lower than that of control astrocytes (3.21±0.23 vs 1.93±0.12 ROIs/FOV, $p<0.0001$; Figure 3D and Figure S1 A). It is noteworthy that we only included the MDs happening within the stimulation window (0-8s) to focus more on Ca^{2+} responses to the sensory stimulation. Similarly, we observed that the fraction of active pixels, the proportion of astrocytes active pixels to the total astrocyte area in each FOV, increased with sensory stimulation in control astrocytes (0.041±0.006 vs 0.082±0.007, $p<0.001$; Figure S1 B), but not in GluN1 KD astrocytes (0.023±0.003 vs 0.017±0.002, $p=0.88$; Figure S1 B). Note that for the proportion of active pixels the whole length of trial was considered and the mean of all 5 trials was calculated for each FOV.

Investigating the magnitude of Ca^{2+} MDs revealed that while whisker stimulation increased the amplitude of Ca^{2+} events in control astrocytes, it did not change the amplitude of MDs in GluN1 KD astrocytes (1.93±0.05 vs 2.22±0.05 dF/F; p=0.0006, 2.05±0.09 vs 1.99±0.06 dF/F; p=0.74; Figure 3E). We also examined the robustness of astrocyte Ca^{2+} MDs responses to whisker stimulation across multiple trials. To do so, we determined the fraction of astrocyte area/pixels in each FOV that were active in more than one stimulation trial and their proportion to the total astrocytes area. We found out that larger fractions of control astrocytes responded repeatedly to multiple trials of stimulation compared to trials without a stimulation (0.049±0.005 vs 0.060±0.005, p=0.03; Figure 3F,G) however, such an increase in response robustness evoked by sensory stimulation was not observed in GluN1 KD astrocytes suggesting that same Ca^{2+} MDs could not be activated by stimulation (0.038±0.008 vs 0.036±0.008, p=1.3; Figure 3F,G) with reduced expression of GluN1. As expected, the fraction of repeatedly active pixels responding to stimulation was significantly smaller in GluN1 KD astrocytes than control astrocytes (0.060±0.005 vs 0.036±0.008, p=0.01; Figure 3F,G). We could not detect any significant sex differences in our observations; data collected from both male and female populations showed the same trend as observed in the pooled data: more Ca^{2+} MDs were evoked by whisker stimulation control astrocytes but not GluN1 KD astrocytes (Females; Control: 2.14±0.24 vs 3.89±0.40, p=0.001, GluN1 KD: 2.34±0.33 vs 1.96±0.22 & Males; Control: 1.95±0.14 vs 2.90±0.27, p=0.002, GluN1 KD: 2.19±0.18 vs 1.91±0.14 ; Figure 3H), and stimulation-evoked MDs were more in control vs GluN1 KD astrocytes (Females; 3.89±0.40 vs 1.96±0.22, p<0.001 & Males; 2.90±0.27 vs 1.91±0.14, p=0.004; Figure 3H).

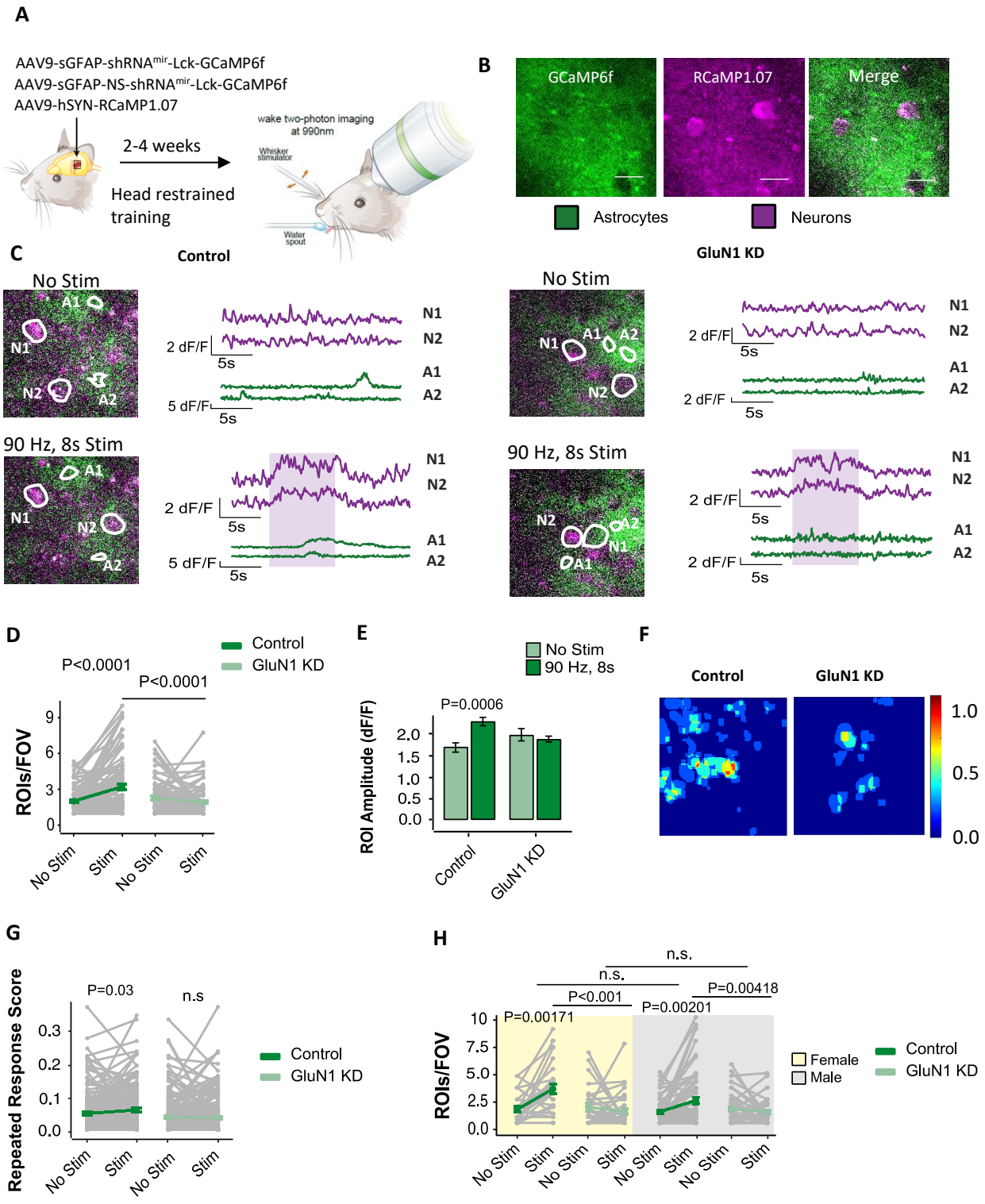
A
AAV9-sGFAP-shRNAmir-Lck-GCaMP6f
AAV9-sGFAP-NS-shRNAmir-Lck-GCaMP6f
AAV9-hSYN-RCaMP1.07
2-4 weeks
Head restrained training
wake two-photon imaging at 990nm
Whisker stimulator
Water spout
B
GCaMP6f
RCaMP1.07
Merge
Astrocytes
Neurons
C
Control
GluN1 KD
No Stim
90 Hz, 8s Stim
A1
A2
N1
N2
2 dF/F
5 dF/F
5s
D
Control
GluN1 KD
P<0.0001
P<0.0001
ROIs/FOV
No Stim
Stim
E
No Stim
90 Hz, 8s
P=0.0006
ROI Amplitude (dF/F)
F
Control
GluN1 KD
G
P=0.03
n.s
Repeated Response Score
H
n.s.
P<0.001
P=0.00418
P=0.00171
P=0.00201
Female
Male

Figure 3. Reduction of stimulation-evoked Ca^{2+} MDs in GluN1 KD astrocytes *in vivo*

A) During surgery, AAVs for astrocyte-specific expression of Lck-GCaMP6f and silencing and non-silencing GluN1 KD construct, as well as neuron-specific expression of RCaMP1.07, were injected before chronic cranial window implantation. Animals were trained to accept head restraint using a water reward for awake two photon imaging. Images of GCaMP6f and RCaMP1.07 were collected during 90 Hz whisker deflection and analyzed using our MATLAB toolbox, Cellular and Hemodynamic Image Processing Suite. ROIs were identified by an algorithm for grouping active pixels or hand-selecting cellular structures (neurons somata). Signals from ROIs were analyzed for different parameters including frequency and amplitude.

B) Example expression of astrocytic Lck-GCaMP6F and neuronal RCaMP1.07. Scale= 20 µm

C) Example ROIs (left) and their traces (right) during no stimulation (top) or whisker stimulation (90 Hz, 8 s) (bottom) for control (left) and GluN1 KD (right) astrocytes (green) and neurons (purple). Astrocytes ROIs are marked as A1,2 and neurons are marked as N1,2. Traces are smoothed by a moving average filter of 3-frame. Purple bar shows stimulation window.

D) Mean number of ROIs per FOV during the 8 s stimulus for Lck-GCaMP6f. (Control: n=103 FOV, 8 mice, GluN1 KD: 97 FOV, 11 mice)

E) Mean ROI amplitude during the 8 s stimulus for Lck-GCaMP6f. (Control: n= 1127 ROIs, 8 mice, GluN1 KD: n= 448 ROIs, 11 mice)

F) Example response heatmaps for control (left) and GluN1 KD (right) generated by overlaying ROI masks from all trials with stimulation. The scale depicts astrocyte regions that were detected in multiple trials with 1.0 (red) indicating a response in all trials and zero (blue) indicating no ROIs detected.

G) Robustness of astrocyte responses to stimulation over repeated trials. Repeated response score indicates in each FOV the fraction of the astrocyte area (pixels) that was active in two or more trials. (Control: n=156 FOV, 8 mice, GluN1 KD: 180 FOV, 11 mice)

H) Mean number of ROIs/FOV during the 8 s stimulus for Lck-GCaMP6f for male and female animals. No sex differences were detected. (Control: n=103 FOV, 4 female and 4 male, GluN1 KD: n=97 FOV, 6 female mice, 5 male mice)

Bar plots are represented as mean ± SEM. All statistics are calculated using linear mixed model and Tukey post hoc tests.

3.4 GluN1 KD in cortical astrocytes reduces fast Ca^{2+} MDs in astrocytes as well as overall activity in surrounding neurons

Combining two different GECIs (as explained above) allowed us to study the dynamics of Ca^{2+} signaling within neurons surrounding astrocytes at the same time. Investigating the RCaMP1.07 Ca^{2+} signals recorded during awake two-photon microscopy, we observed that whisker stimulation increased the number of Ca^{2+} MDs within neuronal cell bodies and dendrites (together) surrounding control astrocytes (i.e. control neurons) compared to no stimulation trials (2.62±0.24 vs 4.77±0.43 ROIs/FOV, p<0.0001; Figure 4A). However, such stimulation-induced elevation in MDs was not detected in neurons surrounding GluN1 KD astrocytes (i.e. GluN1 KD neurons) (3.84±0.32 vs 3.13±0.16 ROIs/FOV; Figure 4A), and the overall sensory stimulation-derived Ca^{2+} ROIs were significantly lower in GluN1 KD compared to control neurons (4.77±0.43 vs 3.13±0.16 ROIs/FOV, p=0.01; Figure 4A), suggesting an overall decrease in cortical neurons responding to whisker stimulation [159,160]. Similar to astrocytes Ca^{2+} MDs, no significant sex differences were observed between the two populations and each group showed similar trends as the pooled data (Females; Control: 3.22±0.67 vs 7.61±1.17 ROIs/FOV, p<0.001, GluN1 KD: 4.24±0.56 vs 3.18±0.28 ROIs/FOV & Males; Control: 2.39±0.22 vs 3.77±0.37 ROIs/FOV, p=0.005, GluN1 KD: 3.54±0.39 vs 3.10±0.20 ROIs/FOV; Figure 4B). Although there is an overall decrease in the number of Ca^{2+} events happening in GluN1 KD neurons in response to stimulation, we observed that the magnitude of the remaining stimulation-evoked Ca^{2+} MDs in these neurons was larger than that of control neurons (1.09±0.01 vs 1.25±0.02 dF/F, p=0.0127; Figure 4C).

Comparing the dynamics of spontaneous neuronal Ca^{2+} events that happened in the absence of whisker stimulation, we interestingly observed that the frequency as well as the amplitude of spontaneous events was higher in GluN1 KD neurons compared to control neurons (2.62±0.24 3.84±0.32 ROIs/FOV, p=0.0037 and 1.23±0.03 vs 1.70±0.09 dF/F, p=0.0006; Figure 4D,E), suggesting that the spontaneous activity was higher in neurons surrounding GluN1 KD astrocytes.

We next investigated the timing of the Ca^{2+} signals relative to the start of the stimulation by comparing peak onset time/latency (OL). We defined onset latency as the earliest timepoint when the fluorescence intensity (dF/F) reached 2.5 times standard deviation (SD) of the baseline signal intensity (Figure 4F). Both control and GluN1 KD neurons showed similar distribution of onset time with a peak around 0.2 s from the start of the stimulation (Figure 4G), and no significant differences was observed between the mean onset latency of the two (2.53±0.03 vs 2.60±0.04 s, p=0.90; Figure 4H).

Generally, astrocytes Ca^{2+} MDs are reported to have slower temporal dynamics compared to neuronal Ca^{2+} events meaning that they are delayed compared to neuronal Ca^{2+} MDs [56,94,106]. However, it has been shown that astrocytes also host a population of MDs that happen in temporal scales comparable to neurons [94,161]. To examine the impact of GluN1 KD on different populations of stimulation-evoked Ca^{2+} MDs with different temporal dynamics, we categorized astrocytes Ca^{2+} MDs into fast and delayed MDs based on their onset latency relative to neuronal population onset latency. Astrocytes Ca^{2+} MDs (within the stimulation window 0-8s) with onset latency faster that the median onset latency of corresponding neuronal type (Control: 1.71s, GluN1 KD: 1.79s; Figure 4G, dashed lines) were considered as fast, and those with onset latency slower than median neuronal onset latency were identified as delayed Ca^{2+} MDs. We observed that both control and GluN1 KD astrocytes host a population of fast MDs (29.37% and 44.57% of total ROIs, respectively; Figure 4I) which occur on a similar time scale as neurons. Importantly, knocking down GluN1 in astrocytes led to a significant decrease in the frequency of this fast onset population of MDs (1.96±0.14 vs 1.46±0.08 ROIs/FOV; Figure 4J) as well as the delayed ones (2.76±0.20 vs 1.55±0.07 ROIs/FOV, $p<0.0001$; Figure 4J).

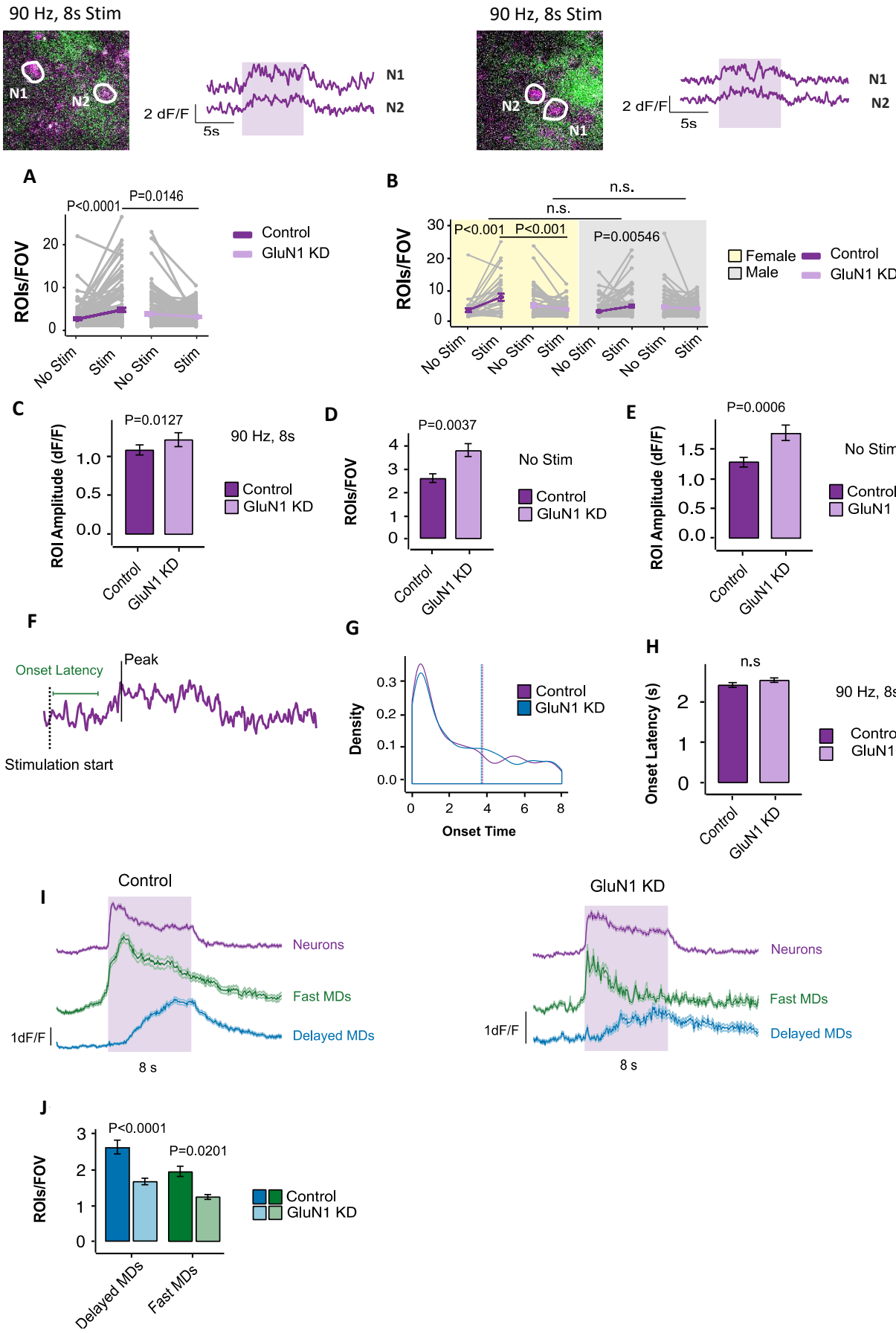
90 Hz, 8s Stim
N1
N2
2 dF/F
5s
N1
N2
90 Hz, 8s Stim
N2
N1
2 dF/F
5s
N1
N2
A
P<0.0001
P=0.0146
ROIs/FOV
Control
GluN1 KD
No Stim
Stim
No Stim
Stim
B
n.s.
n.s.
P<0.001
P<0.001
P=0.00546
ROIs/FOV
Female
Male
Control
GluN1 KD
No Stim
Stim
No Stim
Stim
No Stim
Stim
No Stim
Stim
C
P=0.0127
ROI Amplitude (dF/F)
90 Hz, 8s
Control
GluN1 KD
Control
GluN1 KD
D
P=0.0037
ROIs/FOV
No Stim
Control
GluN1 KD
Control
GluN1 KD
E
P=0.0006
ROI Amplitude (dF/F)
No Stim
Control
GluN1 KD
Control
GluN1 KD
F
Onset Latency
Peak
Stimulation start
G
Density
Control
GluN1 KD
Onset Time
H
n.s
Onset Latency (s)
90 Hz, 8s
Control
GluN1 KD
Control
GluN1 KD
I
Control
Neurons
Fast MDs
Delayed MDs
1dF/F
8 s
GluN1 KD
Neurons
Fast MDs
Delayed MDs
1dF/F
8 s
J
P<0.0001
P=0.0201
ROIs/FOV
Control
GluN1 KD
Delayed MDs
Fast MDs

Figure 4. Overall reduction of stimulation-evoked Ca^{2+} MDs in neurons surrounding GluN1 KD astrocytes *in vivo*

A) Mean number of ROIs/FOV during the 8 s stimulus for RCaMP1.07. (Control: n=122 FOV, 8 mice, GluN1 KD: 144 FOV, 11 mice)

B) Mean number of ROIs/FOV during the 8 s stimulus for RCaMP1.07 for male and female animals. No sex differences were detected. (Control: n=122 FOV, 4 female and 4 male, GluN1 KD: n=144 FOV, 6 female mice, 5 male mice)

C) Mean ROI amplitude during the 8 s stimulus for RCaMP1.07. (Control: n=1799 ROIs, 8 mice, GluN1 KD= 1210 ROIs, 11 mice)

D) Mean number of spontaneous ROIs/FOV for RCaMP1.07. This is identified as number of ROIs/FOV during the equivalent of 8 s stimulus in no stimulation trials. (0-8s) (Control: n= 122 FOV, 8 mice, GluN1 KD: n= 144 FOV, 11 mice)

E) Mean ROI amplitude of spontaneous ROIs for RCaMP1.07. (Control: n=728 ROIs, 8 mice, GluN1 KD= 1014 ROIs, 11 mice)

F) Timing relative to stimulus onset was analyzed for RCaMP1.07 signals. Onset latency (OL) is defined as the earliest time point at which the fluorescent signal [dF/F] reached 2.5 SD of the baseline.

G) Histogram of onset latency for control (purple) and GluN1 KD (blue) and the mean onset latency for each is presented. (Vertical dashed lines: purple; Control mean OL = 1.7177s, blue; GluN1 KD mean OL= 1.7899s)

H) Mean OL for RCaMP1.07 in control and GluN1 KD. No significant difference detected. (Control: n=1799 ROIs, 8 mice, GluN1 KD: n= 1210 ROIs, 11 mice)

I) Mean traces for neurons, fast MDs, and delayed MDs (SEM traces are shown in light color) collected during 8s stimulation. Fast MDs were identified as those with an onset latency within median of neuronal onset latency (1.7177s for control neurons and 1.7899s for GluN1 KD neurons, see Figure 4C). MDs with OL greater than that were identified as delayed. Purple box shows stimulation window. (Control, Delayed MDs: n= 796 ROIs & Fast MDs: n= 331 ROIs & Neurons: n= 1799 ROIs) (GluN1 KD, Delayed MDs: n= 240 & Fast MDs: n= 193 ROIs & Neurons: n= 1210 ROIs)

J) Mean number of fast and delayed MDs/FOV during the 8 s stimulus for GCaMP6f. (Control, Delayed MDs: n= 796 ROIs from 103 FOV & Fast MDs: n= 331 ROIs from 76 FOV & Neurons: n= 1799 ROIs from 122 FOV, from 8 mice). (GluN1 KD, Delayed MDs: n= 240 ROIs from 78 FOV & Fast MDs: n= 193 ROIs from 56 FOV & Neurons: n= 1210 ROIs from 144 FOV, from 11 mice)

All bar plots are represented as mean ± SEM. All statistics are calculated using linear mixed model and Tukey post hoc tests.

3.5 GluN1 KD in cortical astrocytes changes the proportion of different neuronal populations and neuronal correlation

Somatosensory cortical neurons are known to have a high degree of heterogeneity in their response to sensory stimulation [149,162–164] with only a small population (less than 10%) being highly responsive to sensory stimulation [149,164]. Thus, we looked for such heterogeneity in neuronal Ca^{2+} responses within the 8s stimulation window. For both control and GluN1 KD, most neurons showed a small magnitude (dF/F) response to stimulation conforming to sparse firing [162,163,165,166]. However, a small group of neurons showed high amplitude responses to sensory stimulation. Response amplitudes showed a similar log-normal distribution for both control and GluN1 KD neurons with a consistent peak around 1.2 dF/F and a tail of sparse high amplitude responses (Figure 5A). Based on this consistent magnitude distribution, we defined three classes of neurons; we defined cells with an amplitude higher than 98th percentile of control neuronal population (> 3.47 dF/F; Figure 5A) as high responsive cells, cells with amplitudes smaller than 88th percentile of control neuronal population (<1.92 dF/F; Figure 5A) as low responsive cells, and the remaining neurons with amplitudes between these two thresholds (1.92≤ & <3.47 dF/F ;Figure 5A) as mid responsive cells (Figure 5A). In all of these populations, control and GluN1 KD neuronal response magnitude were quite similar and did not show any significant differences (Figure 5B). When considering the total neuronal population, we observed a remarkable reduction in the number of responding neurons surrounding GluN1 KD astrocytes (Figure 4A). Classing neurons based on their response magnitude revealed that this reduction is in the number of low responsive neurons (4.37±0.37 vs 2.80±0.15 ROIs/FOV, $p<0.001$; Figure 5C), while the frequency of stimulation-activated high responsive and mid responsive neurons did not show a remarkable difference between control and GluN1 KD (High responsive: 1.34±0.16 vs 1.41±0.18 ROIs/FOV, Mid responsive: 1.48±0.11 vs 1.58±0.14 ROIs/FOV; Figure 5C). Furthermore, when considering the proportion of responding neuron types in the GluN1 KD population, we observed a shift in the distribution where there was an increase in the proportion of high (1.94 vs 3.06%; Figure 5D) and mid responsive neurons (8.80 vs 13.55%; Figure 5D) accompanied by a decrease in low responsive cells (89.27 vs 83.38%; Figure 5D) in GluN1 KD. This suggests a shift in the distribution of somatosensory cortical neurons responding to stimulation around GluN1 KD astrocytes.

Despite the heterogeneity in population responses to sensory stimulation, neurons in the whisker barrel cortex increase their levels of functional synchronicity as a response to stimulation [149,163,167]. Therefore, we investigated the impact of GluN1 KD on neuronal synchronization. Pairwise

Pearson's correlation coefficients between each pair of neurons per FOV were calculated from Ca^{2+} traces for each cell. Overall, pooled data from control neurons (during the 8 s stimulation) showed an increase in correlation with whisker stimulation (0.113±0.002 vs 0.147±0.001; p=0.025; Figure 5E,F), while neurons surrounding GluN1 KD astrocytes showed a drop in their correlation upon sensory stimulation (0.143±0.001 vs 0.113±0.001, p<0.001; Figure 5E,F), suggesting an overall reduction in activity coordination and synchronicity in the circuit (Figure 5F).

We then investigated the synchronicity within highly responsive neuronal populations. In general, high responsive cells showed higher levels of coordination compared to all other cells. While high responsive control neurons became significantly synchronized in their response to whisker stimulation (-0.39±0.003 vs 0.33±0.02, p<0.001; Figure 5G), GluN1 KD high responsive neurons completely lost their coordination with each other (0.7±0.003 vs -0.14±0.02; p<0.0001; Figure 5G). GluN1 KD high responsive neurons showed higher levels of spontaneous activity coordination compared to control high responsive cells, suggesting an unusually high spontaneous synchronization (0.63±0.006 vs -0.04±0.01, p<0.001; Figure 5G).

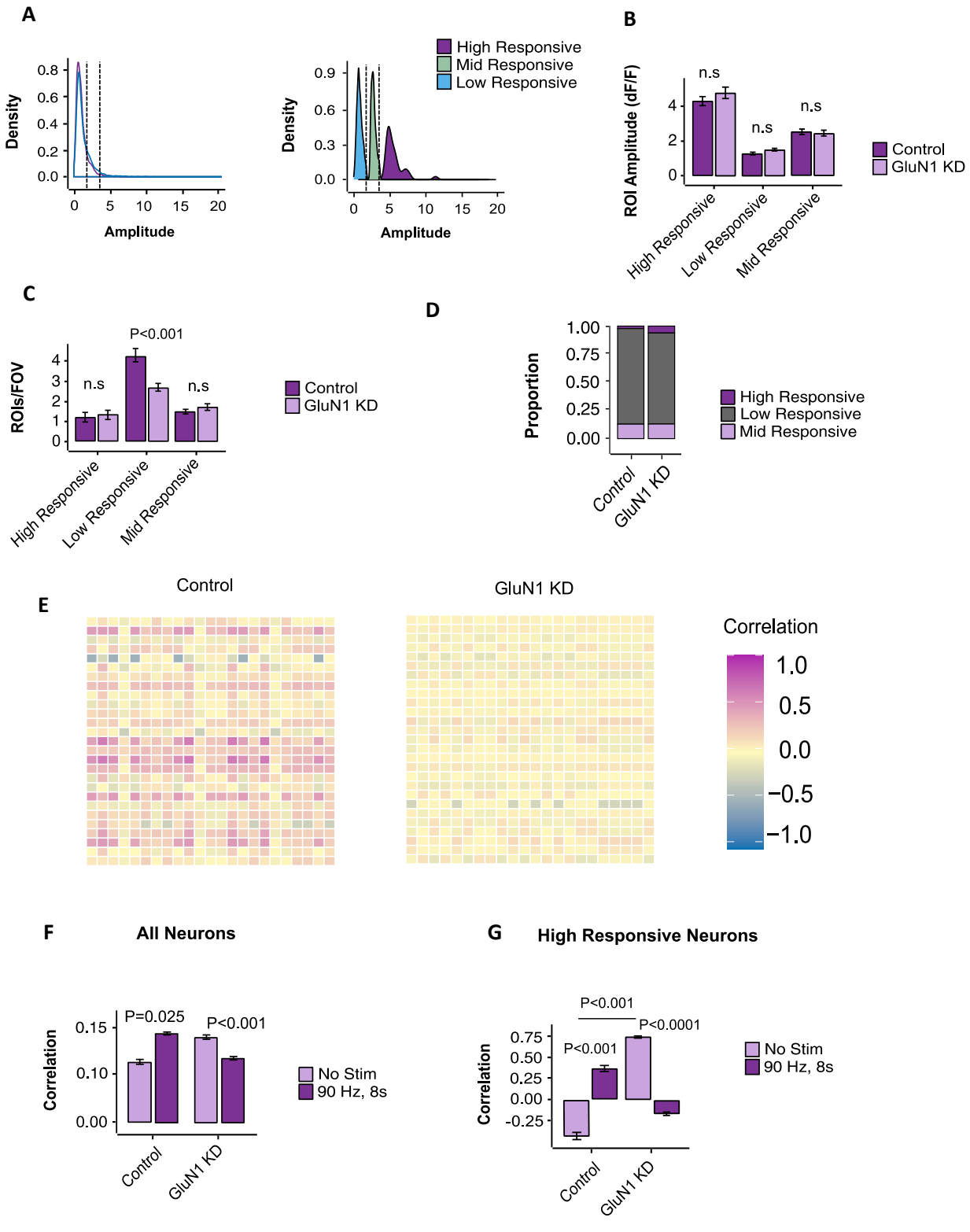
A
Density
Amplitude
High Responsive
Mid Responsive
Low Responsive
B
ROI Amplitude (dF/F)
n.s
Control
GluN1 KD
High Responsive
Low Responsive
Mid Responsive
C
ROIs/FOV
P<0.001
n.s
Control
GluN1 KD
D
Proportion
High Responsive
Low Responsive
Mid Responsive
E
Control
GluN1 KD
Correlation
1.0
0.5
0.0
−0.5
−1.0
F
All Neurons
Correlation
P=0.025
P<0.001
No Stim
90 Hz, 8s
G
High Responsive Neurons
P<0.001
P<0.0001
P<0.001

Figure 5. Changes in neuronal correlation and different classes of neurons encoding sensory stimulus

A) ROI amplitude for RCaMP1.07 for both control and GluN1 KD has a log normal distribution. Thus, based on 98 percentile (dashed line on the right, 3.47 dF/F) and 88th percentile (dashed line on the left, 1.92 dF/F) (left) of ROI amplitude in control neurons, we categorized neuronal responses into three different populations including High responding neurons (amplitude≥ 3.47 dF/F), Mid responding neurons (1.92≤amplitude<3.47 dF/F), and low responding neurons (amplitude<1.92 dF/F) (light).

B) Mean ROI amplitude during the 8 s stimulus for RCaMP1.07 in three different neuronal population. Both control and GluN1 KD neuronal responses are similarly categorized with significant differences between all population within each type. No difference was detected between control and GluN1 KD in none of population. (Control, High Responsive: n= 35 ROIs, Mid Responsive: n= 158 ROIs, Low Responsive: n= 1606 ROIs, 8 mice). (GluN1 KD, High Responsive: n= 37 ROIs, Mid Responsive: n= 164 ROIs, Low Responsive: n= 1009 ROIs, 11 mice)

C) Mean number of different neuronal populations activated by stimulation in each FOV. (Control, High Responsive: n= 20 FOV, Mid Responsive: n= 58 FOV, Low Responsive: n= 121 FOV, 8 mice). (GluN1 KD, High Responsive: n= 19 FOV, Mid Responsive: n= 69 FOV, Low Responsive: n= 141 FOV, 11 mice)

D) Proportion of different neuronal population activated by stimulation in control and GluN1 KD. High responsive neurons; control: 1.94 vs GluN1 KD: 3.06, Mid responsive neurons; control: 8.80 vs GluN1 KD: 13.55, Low responsive neurons; control: 89.27 vs GluN1 KD: 83.38.

E) Example correlation heatmap for control (left) and GluN1 KD (right) neurons activated by stimulation within one FOV. Mean Pearson's correlation coefficient for each pair of ROIs in the FOV (per trial) is presented from -1 (blue, negative correlation) to 1 (purple, positive correlation). (Control: n= 621 Comparisons from 50 ROIs, 1 FOV) (GluN1 KD: n= 2092 Comparisons from 49 ROIs, 1 FOV)

F) Overall correlation between stimulation-activated neurons. Pearson's correlation coefficient is calculated for each pair of activated neurons within 8s stimulation window, within a FOV in each trial. (Control: n= 1269820 Comparisons from 19633 ROIs, 8 mice) (GluN1 KD: n=1198752 Comparisons from 120321 ROIs, 11 mice)

G) Mean neuronal correlation within high responsive population in control and KD animals. (Control, No Stim: n= 1175 Comparisons from 15 ROIs, Stim 90 Hz: n= 222 Comparisons from 31 ROIs, 8 mice). (GluN1 KD, No Stim: n= 3266 Comparisons from 62 ROIs, Stim 90 Hz: n= 367 Comparisons from 36 ROIs, 11 mice)

All bar plots are represented as mean ± SEM. All statistics are calculated using linear mixed model and Tukey post hoc tests.

3.6 Altered neuronal activity caused by astrocytic GluN1 KD leads to sensory perception impairments

Normal whisker sensitivity is one of multiple tests that can confirm the optimal function of this neuronal circuit. We assumed that by knocking down GluN1 in astrocytes and consequently changing patterns of neuronal activity, the sensory circuit in the barrel cortex is perturbed which will lead to impaired whisker sensitivity. To investigate the impact of GluN1 KD on sensory perception, we performed a whisker-mediated discrimination task [156] (WMDT) (Figure 6A) where the animal's ability to discriminate between different textures (grades of sandpaper) was evaluated. After being habituated to the task arena, all whiskers were trimmed, except for those corresponding to the virus injection area. Animals were first introduced to two grades of the same sandpaper for 5 minutes, and after spending another 5 minutes in a resting cage, they were introduced to one familiar grade of sandpaper and a novel grade of sandpaper (texture). The ratio of time animals spent investigating the novel texture versus the familiar texture was defined as the exploration ratio or discrimination ability. Control animals spent more time investigating the novel object where the difference between the average particle size was 62 µm (72%±0.16; Figure 6B) or 32 µm (60%±0.15; Figure 6C) suggesting that they were able to discriminate between the two. However, animals with GluN1 KD spent less than half of their total investigation time exploring the novel object (30%±0.07 or 34%±0.1), suggesting that GluN1 KD mice, as opposed to control mice, were not able to discriminate between textures separated by a difference of 62 µm (Figure 6B) or 32 µm (Figure 6C) in average particle size.

To rule out the possibility that the observed outcome is due to a memory impairment, we performed a novel object recognition task where the animal's ability of detect a novel object using multiple sensory inputs is examined. The task was performed similar to WMDT (Figure 6A); however, instead of different textures, we used two objects different in size, shape, and color. The whiskers were left intact for this behavior test. Control and GluN1 KD animals similarly spent a significant portion of their total investigating time around the new object (Control: 81%±0.11, GluN1 KD:74%±0.13; Figure 6D). This rules out an impairment of memory, which we would expect given our localized AAV construct injection.

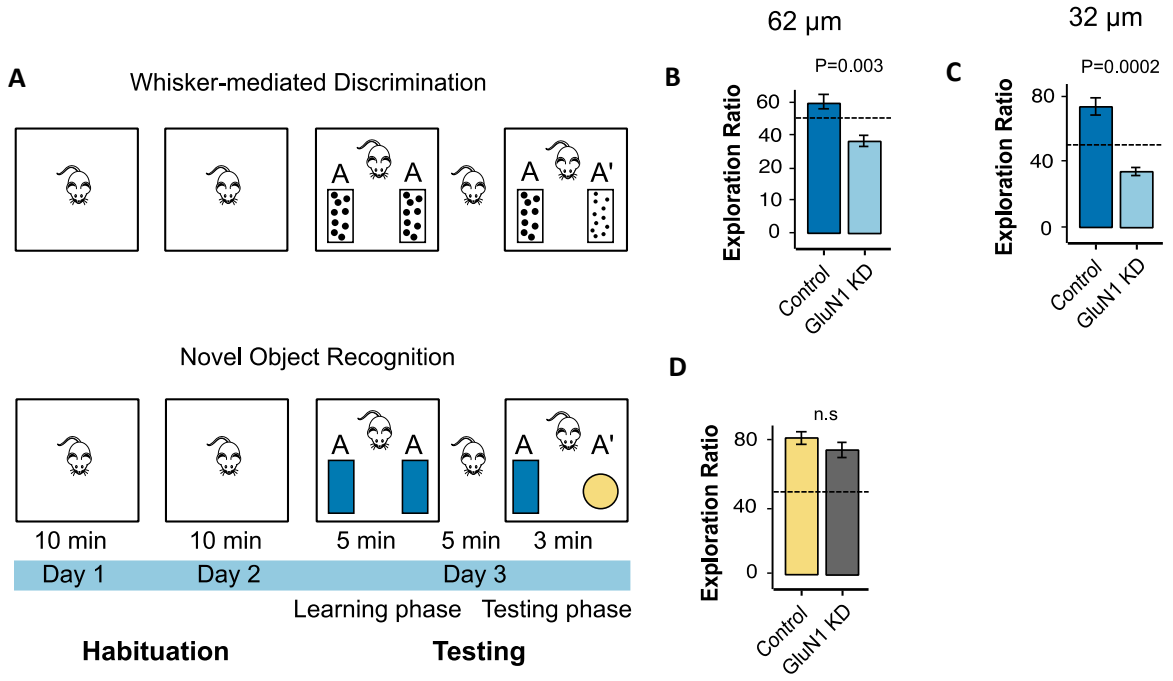

Figure 6. GluN1 KD leads to impairment in sensory perception

A) Diagram of whisker-mediated discrimination test (WMDT) (top) and novel object recognition test (NORT) (bottom) tests. During habituation, animals are placed in the arena for 10 mins per day for two days. At the end of habituation phase, whiskers get trimmed back to the face except for those corresponding to virus injection area (only for WMDT). During testing, animal goes through a learning phase where it is allowed to explore the arena with exact same grades of sandpaper (WMDT)/objects (NORT) for 5 minutes. Animal is then removed and placed in a resting cage for 5 minutes. Then, animal is put back in the arena that now contains one familiar grade of sandpaper/object, same as those in learning phase, and one novel grade of sandpaper/object. Animal's activity is recorded. Percentage of time spent investigating the novel sandpaper/object versus the familiar one is defined as discrimination ability. Investigation is defined as animal facing the sandpaper/object with their nose being at 2cm or closer to the object.

B) Exploration ratio, ratio of time spent around novel sandpaper to total investigation time, for sandpapers with average particle size difference of 62 µm. Dashed line marks chance level (50%). (Control: n= 4 mice, GluN1 KD: n=5 mice)

C) Exploration ratio, ratio of time spent around novel sandpaper to total investigation time, for sandpapers with average particle size difference of 32 µm. Dashed line marks chance level (50%). (Control: n= 4 mice, GluN1 KD: n=5 mice)

D) Exploration ratio, ratio of time spent around novel object to total investigation time. Objects were different in shape, color, and size. Dashed line marks chance level (50%). (Control: n= 5 mice, GluN1 KD: n=5 mice)

Bar plots are represented as mean ± SEM. All statistics are calculated using two-sample t-test.

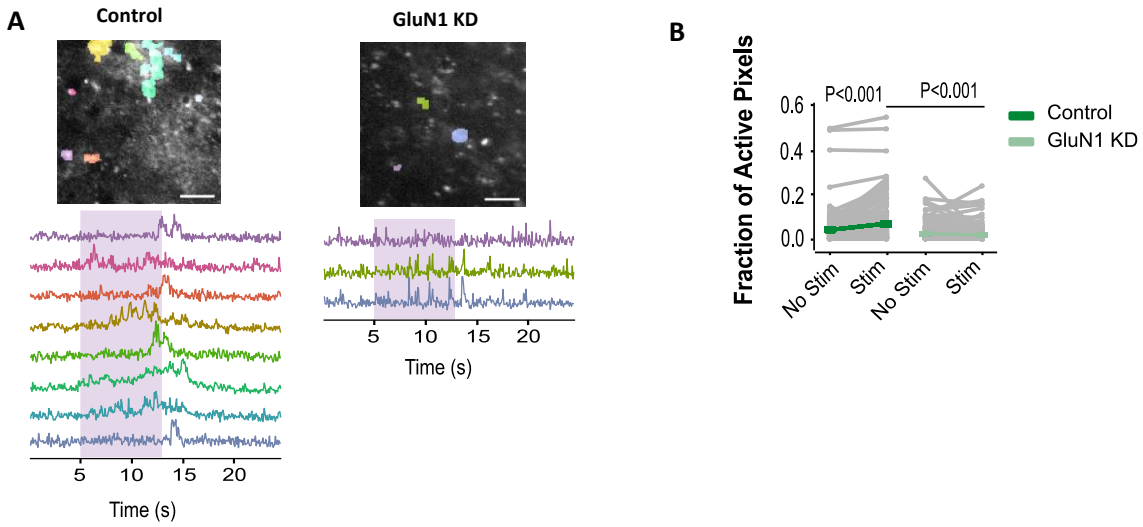

Figure S1. Reduction of stimulation-evoked Ca^{2+} MDs in GluN1 KD astrocytes *in vivo*

A) Example total ROIs and traces evoked by stimulation detected in a whole field of view (FOV) during a whole trial (25 secs, 8s stimulation) in control (left) and GluN1 KD (right) animals.

B) Fraction of active pixels, the ratio of pixels with an increased fluorescent signal to total pixels in a FOV, in control and GluN1 KD mice.

4. Discussion

The current study reveals for the first time the presence of functional NMDARs in cortical astrocytes in awake animal that respond to whisker stimulation-evoked synaptic activity, influence the activity of nearby cortical neurons, and contribute to sensory perception. Previous studies have shown that NMDARs evoke Ca^{2+} events in astrocytes [127,130,132] and there is growing evidence supporting the important role of astrocytes Ca^{2+}-dependent integration in information processing [11]. However, this study is the first to investigate the potential link between the two, shedding light on the role of astrocytic NMDAR in regulation of cortical neuron response to physiological stimulation and ultimately network-mediated sensory perception.

Using a novel microRNA-adapted shRNA that targets the essential NMDAR subunit, we reduced the mRNA abundance of GluN1, specifically in cortical astrocytes, by 70% (Results, Figure 1A-D). Two-photon calcium imaging of membrane-tagged astrocyte-specific Lck-GCaMP6f in cortical astrocytes in brain slices showed a significant reduction in agonist-induced Ca^{2+} MDs in cortical astrocytes with reduced NMDAR expression, confirming the functional reduction of Ca^{2+} MDs following GluN1 KD (Results, Figure 2B,C,E). Such reduction was not due to unviability of the slices as they showed a robust response to phenylephrine application (Results, Figure 2B,D,E). Furthermore, two-photon calcium imaging of membrane-tagged astrocyte-specific Lck-GCaMP6f in cortical astrocytes of awake adult mice revealed that NMDAR reduction significantly supresses astrocytes Ca^{2+} MD responses to cortical synaptic activity (Results, Figure 3C-G). Such reduction is sex-independent (Results, Figure 3H). Using two-photon calcium imaging of neuron-specific cytosolic RCaMP1.07 we demonstrated an overall reduction in the neurons responding to whisker stimulation in GluN1 KD male and female animals (Results, Figure 4A,B) with the remaining Ca^{2+} MDs showing larger amplitudes (Results, Figure 4C). However, we found that the spontaneous neuronal activity, in the absence of whisker stimulation, was significantly higher in neurons near GluN1 KD astrocytes (Results, Figure 4D,E). Onset latency of neuronal responses to stimulation was not impacted by GluN1 KD (Results, Figure 4G,H). Moreover, we identified a population of stimulation-evoked astrocytic Ca^{2+} MDs happening on similar time scales as neurons in both control and GluN1 KD animals (Results, Figure 4I). GluN1 KD supressed both evoked fast and delayed Ca^{2+} MDs in astrocytes (Results, Figure 4J). We observed that in control and GluN1 KD animals only a small population of neurons largely respond to stimulation and the majority of responsive cells show low magnitude responses (Results, Figure 5A,B). Astrocytic GluN1 KD reduces the number of these low responding neurons but not the highly responsive cells (Results, Figure 5C). Overall, responding neurons around GluN1 KD astrocytes seem to undergo a

redistribution with high and mid responsive neurons composing larger proportions of the total responding cells compared to controls (Results, Figure 4D). GluN1 KD-derived neuronal impairment was also reflected in neuronal activity synchronization. Neurons around GluN1 KD astrocytes became decorrelated upon whisker stimulation while control neurons became more synchronized (Results, Figure 5E-G). Finally, we demonstrated that astrocytic GluN1 KD lead to sensory perception impairments and not memory impairments, as KD animals could not discriminate between different textures (Results, Figure 6A-C) but did distinguish between two totally different objects using multiple sensory cues (Results, Figure 6A,D).

Thus, we have provided strong direct evidence for the astrocytic NMDAR to mediate stimulation-evoked Ca^{2+} MDs with spatial and temporal dynamics necessary to modulate synaptic activities, normal neuronal response to sensory stimulation, and sensory perception. The detailed mechanisms underlying these observations require further comprehensive studies; however, we provide some ideas for future directions and discuss potential mechanisms below.

4.1 Astrocyte fast and delayed stimulation-evoked Ca^{2+} MDs are mediated by NMDAR

Astrocytes highly integrate into neuronal networks via their fine processes which enwrap synapses. These processes express a variety of receptors, ion channels, and metabolite transporters that respond to nearby neuronal activity. Many of these receptors evoke transient Ca^{2+} increases in astrocytes which are known to mediate important functions such as modulation of basal synaptic activity, excitatory and inhibitory neurotransmission, and synaptic plasticity [11]. Multiple studies have observed astrocyte Ca^{2+} transients, particularly in somata, in response to NMDA receptor agonist application on cortical slices [119,127,128,130–132,168]. However, the role of NMDAR in Ca^{2+} MDs has yet to be investigated. For the first time in this thesis, we investigated the impact of NMDAR reduction on Ca^{2+} MDs using a novel miRNA-adapted shRNA that targets GluN1. This miRNA-adapted shRNA construct was regulated by GFAP promoter to only impact NMDAR in astrocytes (Results, Figure 1A). Immunohistochemistry confirmed the astrocyte-specific expression of our construct (Results, Figure 1B). We also showed a 70% reduction in expression of GluN1 on mRNA levels in cortical astrocytes (Results, Figure 1C,D), confirming the functionality of this shRNA construct. Furthermore, our pharmacology studies demonstrated a functional reduction of NMDAR in astrocytes and NMDAR mediating Ca^{2+} MDs (Results, Figure 2). While application of NMDA and D-serine to cortical slices in the presence of neuronal blockers evoked robust Ca^{2+} MDs in control Lck-GCaMP expressing astrocytes, GluN1 KD strongly supressed agonist-induced Ca^{2+} MDs in these cells (Results, Figure 2B,C,E). Robust Ca^{2+} MD

response to phenylephrine confirmed the viability of the cells (Results, Figure 2D). However, GluN1 KD astrocytes showed smaller responses (AUC) to phenylephrine (Results, Figure 2D,E) which might be suggestive of a potential interaction between NMDAR and Gq-GPCR signalling as discussed below. These findings reveal the functionality of our shRNA construct, confirms the previous findings on NMDA-induced Ca^{2+} response in astrocytes[118,119,130,131], and importantly through combination of this novel shRNA construct and membrane-tagged Lck-GCaMP, provide direct evidence that astrocytic NMDAR mediates Ca^{2+} MDs.

Astrocytic Ca^{2+} MDs are evoked in response to nearby neuronal activity [3,4,91,94,95,169]. However, the role of astrocytic NMDAR in astrocyte Ca^{2+} responses *in vivo* is unknown. In this study, we demonstrated for the first time that NMDAR mediates sensory stimulation-evoked Ca^{2+} MDs in cortical astrocytes, since supressing receptor expression significantly dropped the frequency and amplitude of these events is response to whisker stimulation (Results, Figure 3D,E). Despite being deemed as too slow to modulate rapid synaptic activity or blood flow regulation, astrocytes host a population of fast Ca^{2+} MDs within their fine processes, responding to physiological stimuli on a time scale which closely follows neuronal activity [53–55,94,170]. This suggests that astrocyte Ca^{2+} MDs, particularly localized to fine processes close to synapses, possess the necessary temporal and spatial dynamics to rapidly modulate neuronal activity. We demonstrated that, in addition to delayed MDs, NMDARs contribute to fast astrocyte Ca^{2+} MDs (that occur within the median neuronal onset latency in our study) because GluN1 KD astrocytes showed a significantly lower number of stimulation-evoked fast MDs compared to control astrocytes (Results, Figure 4J). Therefore, astrocytes lacking NMDARs may no longer possess the calcium transients needed for quick alteration of synaptic activity.

Multiple pathways may potentially lead to NMDAR-mediated Ca^{2+} MDs. Canonical function of NMDAR is known as a cationic channel with partial selectivity for Ca^{2+} [171]. The most direct mechanism underlying NMDAR-mediated Ca^{2+} MDs therefore, could be direct influx of Ca^{2+}. This would be best visualized using membrane-tagged GECIs that capture fast MDs and localized, rapid Ca^{2+} fluctuations near the plasma membrane, which is one reason why we used Lck-GCaMP6f in this study. Another possible mechanism for NMDAR-mediated Ca^{2+} MDs could be the reverse function of the Na^+/Ca^{2+} exchanger (NCX). An increase in intracellular Na^+ can switch NCX to reverse mode where it brings Ca^{2+} in for Na^+ efflux and creates Ca^{2+} MDs [172–174]. One possible mechanism that increases intracellular Na^+ and triggers NCX reverse function is glutamate-induced activation of N+-permeable channels[175–177] such as NMDARs [177,178]. Reverse NCX function-mediated Ca^{2+} events in astrocytes can also lead to release of gliotransmitters[179,180]

such as ATP/adenosine[181]. Adenosine can activate presynaptic adenosine receptors and supress glutamatergic signaling [181]. Moreover, NMDAR-mediated Ca^{2+} MDs might be due to activation of voltage gated Ca^{2+} channels (VGCCs). VGCCs are activated by membrane depolarization and mediate Ca^{2+} influx [1,182]. NMDAR activity in astrocytes possibly activates VGCCs, as NMDAR depolarizes the membrane, and is important for maintaining presynaptic heterogeneity possibly through release of gliotransmitters [133]. Uptake of extracellular K^+ also can activate VGCCs [183]. Therefore, VGCCs in astrocytes are possibly activated during synaptic activity when there are high levels of extracellular K^+ and glutamate leading to astrocyte depolarization. Finally, NMDAR activity can act through metabotropic pathways and lead to release of Ca^{2+} from intracellular stores [112,184–187]. For instance, glutamate and NMDA-induced Ca^{2+} events in cultured astrocytes are shown to be partially blocked by an NMDAR antagonist, sensitive to lack of extracellular Ca^{2+}, and inhibited by ER SERCA ATPase (transfers Ca^{2+} into the ER lumen) blocker[186,187]. This suggests involvement of metabotropic and NMDAR signaling during astrocyte NMDA-induced Ca^{2+} responses. Similarly, NMDA-induced Ca^{2+} responses in astrocytes are sensitive to NMDAR antagonists, but also an IP3R antagonist [184]. In addition to pathways that elevate astrocyte Ca^{2+}, NMDAR have been linked to a reduction in astrocyte Ca^{2+} levels. Specifically, activation of astrocytic NMDARs during theta burst cortical activity decreases free Ca^{2+} in astrocytes through elevation of store uptake via SERCA [131]. Thus, astrocyte NMDAR are potentially critically important for regulating Ca^{2+} at multiple points within the cell from Ca^{2+} influx to store release. Any of these mechanisms may contribute to astrocyte Ca^{2+} MDs, but our results suggest that both extracellular Ca^{2+} influx and interactions with pathways that cause release of internal Ca^{2+} stores are a factor in this NMDAR signaling.

These pathways might possibly explain our observations. First, we observed a significant reduction of evoked Ca^{2+} MDs including fast and delayed MDs (Results, Figure 3D,E). One possible explanation could be the non-canonical, metabotropic-like function of NMDAR. As explained above, NMDAR's ionotropic function in astrocytes concurs with metabotropic signaling pathways and probably involves release of Ca^{2+} from ER. Reduced NMDAR activity in GluN1 KD astrocytes might lead to reduced IP3R-mediated release of Ca^{2+} and therefore, reduction of delayed Ca^{2+} MDs.

Second, a reduction in delayed Ca^{2+} MDs (Results, Figure 3D,E and Figure 4J) as well as Ca^{2+} store-mediated Ca^{2+} response (AUC) to phenylephrine (Results, Figure 2D) could be due to reduced stores Ca^{2+} levels as a result of decreased NMDAR activity. NMDAR contributes to intracellular Ca^{2+} levels through multiple mechanisms as explained above. Disruption of any of

these mechanisms can lead to reduced intracellular Ca^{2+} stores content. This is particularly important since astrocytic NMDARs elevate Ca^{2+} store filling during high cortical activity [131]. Therefore, NMDAR might regulate basal astrocyte Ca^{2+} concentrations, which has implications for Ca^{2+} microdomain activity and their dynamics such as amplitude and peak frequency [136,137]. On the same note, reduction of repeatedly evoked Ca^{2+} MDs in GluN1 KD astrocytes (Results, Figure 3F,G) might be further indicative of potential impairments in replenishment of Ca^{2+} stores since Ca^{2+} MDs subpopulations can be reproduced within the same cellular region by repeated trials of whisker stimulation [95]. Consistently, we observed repetitive Ca^{2+} MDs evoked by repeated stimulation in control astrocytes.

Third, it should be noted that fast MDs were shown to be largely independent of IP3R2 and Ca^{2+} release from stores [94], and have been suggested to result from extracellular calcium influx [11]. Reduced fast Ca^{2+} MDs is suggestive of impaired fast ionotropic function of NMDAR in GluN1 KD astrocytes, and a loss of extracellular Ca2+ influx.

While the detailed mechanism remains unclear, overall, such reduction of stimulation-evoked fast and delayed Ca^{2+} MDs in GluN1 KD astrocytes is suggestive of impaired canonical ionotropic and metabotropic-like function of NMDAR in these cells. Decreased whisker stimulation-evoked Ca^{2+} MDs in GluN1 KD could impact the inherent temporal properties of astrocytes to modulate neuronal activity through gliotransmission. In terms of functional significance, astrocytes Ca^{2+} transients are followed by release of gliotransmitters including GABA, ATP, glutamate, and D-serine [2–4,22,31,33,35–38]. Reduced Ca^{2+} events therefore, might decrease gliotransmitter release in GluN1 KD astrocytes and change synaptic activities, as described in sections below.

4.2 Altered stimulation-evoked neuronal activity following GluN1 KD in astrocytes

Ca^{2+} signals in neurons are widely used to study a variety of neuronal events [159,160]. The amplitude of Ca^{2+} transients is linearly proportional to neuronal action potential firing; therefore, elevations in Ca^{2+} integrate neuronal firing [188,189]. L2/3 neurons of the barrel cortex have Ca^{2+} transients when whiskers are stimulated. However, only a small group of these neurons respond to whisker stimulation with robust large amplitude Ca^{2+} signals [149,164]. This is consistent with electrophysiology measurements indicating that although almost all pyramidal neurons receive whisker stimulation-evoked excitatory inputs, only a small group (~10%) of these neurons fire robust action potentials in response to whisker stimulation which are sufficient to reliably represent the sensory stimuli[145–147,190,191]. This sparse coding is regulated by fast recruitment of inhibitory GABAergic neurons[143,145–147].

We observed an overall reduction in neuronal activity in response to whisker stimulation (Results, Figure 4A), particularly in the number of low responsive neurons, in GluN1 KD animals (Results, Figure 5C). Considering that most neurons in L2/3 are pyramidal neurons, and whisker stimulation evokes an increase in excitatory activity in L2/3 as we observed in control animals, a decrease in low responsive neurons could potentially be representative of a reduction in recruitment of pyramidal neurons with few depolarizing spikes and small amplitude Ca^{2+} responses, but do not robustly fire action potentials in response to whisker stimulation. Also, despite the sparse horizontal connection of pyramidal neurons in L2/3 [143,146], it is suggested that sparse coding is potentially mediated by convergence of multiple rare strong synaptic inputs from the L2/3 pyramidal neurons onto one postsynaptic neuron in the same layer, thus, driving it to fire [143]. These strong inputs link neurons into strongly connected functional "Hebbian cell assemblies" that are strengthened through correlated activity in presynaptic and postsynaptic neurons [143,192]. This highlights the importance of same-layer excitatory connections and could suggest that broad recruitment of excitatory pyramidal neurons is necessary for normal reliable sparse coding and stimuli representation. While the importance of low responsive cells in L2/3 is still mysterious, it is suggested that these cells are recruited during plasticity [164,193,194]. Low responsive neurons have been shown to undergo a strong retuning as a response to whisker trimming, strengthening their response to stimulation of the neighboring, untrimmed whisker [164]. This suggests an important role for low responsive neurons in recoding sensory stimuli after a change in sensory experience. Thus, reduced recruitment of low responsive neurons in GluN1 KD animals could also lead to altered retuning of sensory responses in case of changes in sensory experience. However, this is beyond the scope of this study and needs further investigation.

Pyramidal neurons are densely innervated by different types of GABAergic neurons. In fact, the connectivity rates of excitatory and inhibitory neurons are much higher than excitatory neurons with each other [195,196]. Pyramidal neurons receive almost simultaneous excitatory and inhibitory inputs, the net result of which is hyperpolarized potential for most neurons [145,146]. PV neurons, also known as fast-spiking (FS) inhibitory neurons, largely mediate sparse firing. Pharmacological and optogenetic inhibition of PV neurons increases firing rates in pyramidal neurons [148,197–199]. Therefore, the observed reduced recruitment might be suggestive of enhanced inhibitory activity by PV neurons on pyramidal neurons in GluN1 KD animals. This is particularly important since the L2/3 GABAergic neuronal network significantly change their activity levels with whisker movement. PV neuron activity is largely inhibited during free whisking (when animals freely move their whiskers) [199,200] and whisker stimulation (when whiskers are deflected by experimenters) [201]. Similarly, SST neurons which densely innervate pyramidal neurons and have strong inhibitory

inputs on them [202,203], also reduce firing rates during free whisking [148,200,204,205], whisker stimulation [148], and active whisker-object touch [148]. This suggests that pyramidal neurons in L2/3 undergo a form of disinhibition creating escape spots for pyramidal neurons and making sensory processing possible. Reduced disinhibition in GluN1 KD pyramidal neurons might contribute to a reduced response to stimulation. Such disinhibition could be potentially mediated by VIP neurons as they strongly inhibit SST neurons which inhibit PV neurons [204,206–208]. However, we cannot confirm the involvement of any of these populations with our current technique as we did not label specific neuronal populations. Moreover, we do not have any information about baseline neuronal activity before GluN1 KD; thus, we cannot rule out the possibility of differences across individual cell activity and random labeling of neurons.

Enhanced inhibitory levels due to reduced disinhibition in GluN1 KD animals can also support the behavioral impairments we observed in these animals. Mice with GluN1 KD astrocytes could not discriminate between textures with slight or mild average particle size difference (Results, Figure 6 B,C) . We demonstrate that this lowered ability to distinguish between similar textures is not due to short-memory impairment since animals with GluN1 KD astrocytes performance in NORT, where they are evaluated for discrimination ability based on not solely whisker touch but different sorts of sensory cues, was same as control animals (Results, Figure 6D). Glutamatergic transmission is necessary for stimulus perception [209], and sensory perception is encoded by robust activity of a small population of pyramidal neurons [149]. Optogenetic inhibition of PV neurons in mice performing a deflection detection task where they reported stimuli detection through licking a waterspout for water reward, increased excitatory activity and enhanced the performance, whereas optogenetic activation of PV neurons reduced the performance [201,209]. Therefore, reduced excitatory activity, possibly through enhanced PV activity may cause impaired sensory perception and/or discrimination. Such enhanced PV activity might be due to reduced SST activity, since they inhibit PV neurons [207]. However, with our current behavior tasks we could not pinpoint to what extent sensory acuity impaired in GluN1 KD animals. Future studies with WMDT that have larger texture differences could determine if the discrimination ability is partially lost. Also, it is possible that the impaired discrimination was due to a total loss of sensory perception (as explained below) in the first place where animals with GluN1 KD could not perceive the novel texture. In either case, our results suggest that reduced excitatory activity due to astrocytic GluN1 KD have behavioral implications for sensory information processing.

4.3 Altered spontaneous neuronal activity near GluN1 KD astrocytes

The primary somatosensory cortex including the whisker barrel cortex is under a widespread blanket of inhibition which shows local and transient “holes” when required to encode sensory information[206]. Indeed, locally-infused $GABA_A$ receptor antagonist increases spontaneous pyramidal neuron activity [199]. This extended inhibition exists in quiet wakefulness periods when whiskers are not deflecting and changes when whiskers are stimulated. Quiet wakefulness in L2/3 can be characterized by low activity of pyramidal neurons and high activity of PV neurons[145,146]. Tonic spontaneous inhibition during quiet wakefulness is largely mediated by spontaneous activity of SST neurons. In fact, optogenetic inhibition of SST neurons during quiet wakefulness strongly increased action potential firing in nearby pyramidal neurons in L2/3 [148,197]. Reduced SST activity is also correlated with increased Ca^{2+} signaling in barrel cortex layer 1 excitatory dendrites which promotes top-down sensorimotor integration [148]. Similarly, PV neurons show reduced action potential firing rates with free whisking. Optogenetic inhibition of PV neurons also increases spontaneous firing rates in L2/3 [198]. Our results indicate a significant increase in spontaneous activity of GluN1 KD neurons in the absence of whisker stimulation compared to control neurons (Results, Figure 4D,E). This increased spontaneous activity suggests a decrease in the tonic spontaneous inhibition on pyramidal neurons leading to increased excitability levels in the network. This may occur as a consequence of reduced inhibition of SST and/or PV neurons.

This enhanced spontaneous excitability may have implications on sensory perception. During quiet wakefulness in the absence of whisker movement, spontaneous excitatory activity levels are low, and neurons show large slow membrane potential fluctuations [146,162]. Whisker deflection evokes a high contrast activity compared to baseline firing, reduces membrane potential variance, and drives a strong network response to whisker movement [146]. In fact, this **contrast** is important for sensory information coding and improves signal-to-noise ratios for sensory processing [210]. During active whisker touch (where animals actively whisk and touch an object), the membrane potential precontact determines the neuronal response to touch. Comparing the response evoked by whisker touch in neurons relative to their precontact (free whisking) membrane potential revealed that touch-evoked responses are larger at spontaneously hyperpolarized membrane potentials and are hyperpolarizing at spontaneously depolarized membrane potentials thus have an inhibitory impact [147]. Brief whisker deflection delivered during free whisking evokes smaller sensory responses than during quiet wakefulness and probably leads to reduced detection performance [211]. Therefore, increased spontaneous excitability and pre-stimulation depolarized membrane potentials in GluN1 KD neurons could suppress whisker deflection-evoked responses

and disrupt encoding of sensory stimuli which is translated into animals inability to discriminate between similar textures.

4.4 Altered correlation of neuronal activity near GluN1 KD astrocytes

Increased spontaneous activity may explain the enhanced spontaneous correlation we observed between high responsive neurons in GluN1 KD animals (Results, Figure 5G). During quiet wakefulness nearby neurons exhibit synchronous slow large-amplitude membrane potential fluctuations which become supressed and less correlated during free whisking [148,162,199,210]. During whisker active touch and whisker stimulation, neurons exhibit robust highly correlated depolarizations [147,149,163,167], which are more temporally precise [147]. In GluN1 KD neurons, their high spontaneous correlation may be partially due to reduced inhibition on their activity. Moreover, high responsive neurons in GluN1 KD animals decorrelated upon whisker stimulation, while neurons in control animals became more correlated (Results, Figure 5G), which is consistent with previous studies [147,149]. Within-population decorrelation of high responsive GluN1 KD neurons with whisker stimulation may also suggest enhanced inhibitory activity because neurons that normally fire together with a functional synchronization reminiscent of Hebbian "cell assemblies" (See section 4.2) are not able to correlate their membrane potential dynamics due to the hyperpolarizing inhibitory impacts. A similar trend was observed for pairwise correlation of all neuronal populations within each field of view (Results, Figure 5F). Overall, pooled data from all neuronal populations showed that control neurons became more correlated with whisker stimulation consistent with previous studies [149,163,167] while GluN1 KD neurons decorrelated suggesting supressed action potential firing in pyramidal neurons. Although whisker deflection increases correlation, pyramidal neurons do show, in smaller scales, correlation in the absence of stimulation [149,163,167]. Consistently, our results from pooled data including all neuronal populations from both control and GluN1 KD animals showed some level of spontaneous correlations. However, we found control neurons that are highly responsive to stimulation (large amplitudes) to be spontaneously decorrelated. This may occur if animals were whisking during no stimulation trials, leading to strong thalamic inputs and a desynchronized cortical state.

There are several limitations to our interpretation of the neuronal changes following astrocyte GluN1 KD. First, as we did not use GECI expression in specific neuronal populations, i.e., pyramidal, PV, SST, or VIP, our results are not informative about relative changes in activity in different neuronal populations. Second, we have no knowledge of the neuronal activity in GluN1 KD prior to virus injection thus control animals are our only reference. Therefore, we are not able to determine how specific cells changed their response after GluN1 KD (e.g. were high responding

cells always high responding?). Third, we did not monitor whisker movements, so we can not confirm when animals were actively whisking, which will be important to consider in the future given the effect that such behaviour has on sensory processing. However, it is tempting to hypothesize based on our results showing increased spontaneous activity and supressed recruitment of neurons in response to stimulation, that the excitatory-inhibitory balance in these animals is impaired as inhibitory and excitatory conductance in cortex are closely correlated ensuring balanced inhibitory and excitatory neuronal activity and reliable sensory stimulus encoding [145,146,199]. This impaired balance is also represented as the reorganization of the proportion of different neuronal populations responding to whisker stimulation in GluN1 KD animals compared to controls (Results, Figure 5D).

What could be the role of GluN1 KD astrocytes in such imbalance between excitatory and inhibitory neurons activity? We hypothesize that this is mediated by impaired gliotransmission caused by reduced sensory-evoked Ca^{2+} MD events in GluN1 KD astrocytes.

4.5 Possible gliotransmission-based mechanisms for GluN1 KD astrocytes leading to altered neuronal function

Astrocyte-released ATP regulates basal synaptic transmission, pyramidal neuron inhibition, and heterosynaptic depression [3,4,39,128,187,212]. ATP can reduce excitatory activity through two potential mechanisms. First, through increasing SST neurons activity. In the hippocampus, SST neuron activation evokes Ca^{2+} events in astrocytes which lead to release of ATP which is converted extracellularly into adenosine. Resulting adenosine then acts on postsynaptic A1 receptors and upregulates SST neuron synaptic inhibition of pyramidal neurons [3]. Moreover, astrocyte-released ATP/adenosine inhibits excitatory transmission through activation of presynaptic A1 receptors [39,40,213–215]. On the other hand, ATP can also increase excitatory activity by adenosine receptor A2- or P2X receptor-mediated suppression of inhibitory neurons. Astrocyte-released ATP activates presynaptic A2 receptors after being converted to adenosine and enhances excitatory synaptic transmission in hippocampus. Activation of A2 receptors on hippocampal GABAergic interneurons decreases their activity, leading to enhanced pyramidal neuron synchronous firing [216]. Also, cortical astrocyte-derived ATP supresses $GABA_A$-mediated inhibitory synaptic signaling through activation of P2X receptors[128]. Overall, balanced activation of A1 receptors, inhibitors of synaptic transmission, and A2 receptors, facilitators of synaptic transmission, by astrocyte-derived adenosine tightly maintains an excitation-inhibition balance. Adenosine supresses the inhibitory and excitatory transmission to pyramidal neurons by activating A1 receptors; however, this suppression is modulated by activation of A2 receptors as blocking these receptors magnifies

the suppression, suggesting a bidirectional concentration-dependent modulation of excitatory-inhibitory balance by adenosine [217].

ATP-mediated reduced excitatory activity could be relevant for enhanced spontaneous activity in GluN1 KD neurons. We suggested above in section 4.3, that the increased spontaneous activity in GluN1 KD neurons might indicate a leak in this SST-mediated tonic inhibition. Importantly, SST neurons largely mediate the tonic inhibition of cortical pyramidal neurons during quiet states. Since astrocyte-released ATP upregulates SST inhibition on pyramidal neurons, one may consider such enhanced spontaneous activity a result of reduced ATP gliotransmission in GluN1 KD astrocytes. Moreover, ATP-mediated enhancement of synaptic transmission can be relevant for reduced neuronal response to whisker stimulation in GluN1 KD neurons. Reduced levels of astrocyte-released ATP could lead to reduced excitatory synaptic transmission, pyramidal neuron disinhibition and recruitment in GluN1 KD neurons. Similarly, reduced astrocyte-released ATP that can cause reduced excitatory activity could potentially contribute to desynchronization of GluN1 KD neurons upon whisker stimulation.

Also, astrocyte-derived ATP/adenosine plays different roles in modulating long term potentiation in pyramidal and PV neurons. A2 receptor activation by endogenous adenosine upregulates glutamatergic synapses on PV neurons [212], while astrocyte-derived ATP down regulates NMDAR-mediated long-term potentiation (LTP) in excitatory neuron through recruitment of P2X receptors [218]. Astrocyte-released ATP/adenosine is also necessary for heterosynaptic depression of pyramidal neurons in hippocampus, which is a correlate of LTP that enhances the contrast between activated and non-activated synapses and improves the synaptic efficacy [39,215]. On a related note, astrocytes NMDAR mediates heterosynaptic plasticity by maintaining the heterogeneity of paired pulse ratio, the ratio of release probability for the second pulse to the first pulse, which is seen between two presynaptic neurons that target the same postsynaptic neuron, in hippocampus [133,135]. Heterosynaptic plasticity in the cortex is important for synaptic strength regulation [219,220] and enhancing excitation-inhibition balance [150]. Heterosynaptic plasticity is involved in learning, learning capacity, experience-dependent regulation of synapses, and information processing [221–223]. Therefore, the importance of astrocyte-derived ATP/adenosine in ensuring a proper excitation-inhibition balance and synaptic modulation and plasticity which in turn mediates efficient and precise information processing is well established. Thus, potential reduced ATP release from GluN1 KD astrocytes might change synaptic plasticity through impaired synaptic potentiation or depression possibly contributing to the deficient sensory perception we observed.

The NMDAR co-agonist, D-serine, is shown to be released from astrocytes [2,12,42]. Therefore, astrocytes have the ability to impact NMDAR-mediated synaptic modulations such as LTP and LTD [2,41,42]. Co-release of D-serine and glutamate from hippocampal astrocytes enhances the induction of heterosynaptic long term depression (LTD) which is important for reversal learning and flexible memory [43]. Ca^{2+}-dependent release of D-serine from hippocampal astrocytes also potentiates LTP induction in excitatory neurons [2]. Glutamate, the main excitatory transmitter of the brain can also be released from astrocytes. Astrocyte-released glutamate enhances transmitter release, induces LTP in hippocampal synapses [38], and enhances excitatory synaptic strength [36]. Together, evidence strongly supports the contribution of Ca^{2+}-dependent release of D-serine as well as glutamate from astrocytes to modulation of synaptic strength and plasticity. Synaptic plasticity requires fine adjustment of excitatory and inhibitory balance to ensure experience-dependent synaptic modifications required for enhancing the representation of sensory stimuli [219,220,224]. Impaired astrocyte-released D-serine and/or glutamate could reduce induction of LTP and/or LTD in pyramidal and/or PV and/or SST neurons and lead to inefficient representation of sensory stimuli and impaired discrimination ability in GluN1 KD animals. In case pyramidal neurons are the primary target of such reduction in plasticity, this mechanism also fits with the reduced number of low responsive neurons in GluN1 KD, which are recruited by plasticity[164,193,194] (See section 4.2). Reduced release of D-serine and/or glutamate from astrocytes could cause decreased recruitment of low responsive neurons in synaptic weight redistribution (i.e. fewer low responsive neurons responding to whisker stimulation) and lead to impaired representation of stimuli and sensory perception. Moreover, episodic release of glutamate also evokes synchronous activity of neighboring hippocampal neurons through simultaneous activation of extra-synaptic NMDARs [22]. Thus, reduced release of glutamate from GluN1 KD astrocytes could contribute to decorrelation of high responsive neurons in GluN1 KD animals upon whisker stimulation.

Astrocytic gliotransmission has also been linked to behavior. Ca^{2+}-dependent ATP release from astrocytes has anti-depressant effects in mouse models of depression possibly through P2X2 receptors [66]. Interestingly, impaired astrocyte Ca^{2+}-signaling drives autism spectrum disorder-like behaviors such as repetitive behaviors and aberrant social novelty preference, which is rescued by astrocyte-derived ATP that potentially works through presynaptic P2X2 receptors which facilitate glutamatergic transmission on GABAergic interneurons [225]. Therefore, reduced ATP could reduce inhibitory interneuron activity leading to increased excitability and impaired excitation-inhibition balance [67,68]. Anti-depressant-like effects are also associated with endogenous D-serine which mediates synaptic plasticity through NMDAR-dependent synaptic

LTD [69]. These studies support astrocyte integration into higher circuit levels and impacts on behavior through release of gliotransmitters. Therefore, a link between impaired gliotransmission of ATP and/or D-serine and sensory perception in GluN1 KD animals is possible. Another possible mechanism could be that lower levels of ATP released from GluN1 KD astrocytes could cause lower novelty preference [67] in GluN1 KD animals through increased excitatory activity which could contribute to impaired texture discrimination in these animals however, this needs further investigation.

4.6 Other possible mechanisms for GluN1 KD astrocytes leading to altered neuronal function

Astrocytes Ca^{2+} signaling contributes to multiple other functions of astrocytes beyond gliotransmission. By disrupting astrocyte Ca^{2+} MDs and NMDAR signaling with our GluN1 KD approach, we may also alter the following mechanisms. First is the remodeling of peri-synaptic astrocyte processes. The fine synapse-covering processes undergo Ca^{2+}-dependent structural changes as the result of LTP-inducing synaptic activity, increasing their coverage and enhancing the potentiated synapse's stability [44]. Therefore, reduced Ca^{2+} signaling in GluN1 KD astrocytes may impair synaptic contact by astrocytes. Second, NMDA-induced somatic Ca^{2+} transients in cultured cortical astrocytes upregulate the Cdk5/Nr2f pathway, a key regulator of genes for cell antioxidant machinery that leads to increased release of glutathione precursors from astrocytes. These precursors are used by nearby neurons to synthesize glutathione, an important antioxidant, thus potentially contributing to neuronal protection against oxidative stress [134]. Therefore, GluN1 KD may impair neuronal responses to oxidative stress, leading to network dysfunction and possibly cell death. Finally, astrocytes are known to supply neurons with energy metabolites, such as lactate [26,27], and astrocyte metabolism and mitochondrial function have been linked to Ca^{2+} transients [64]. Therefore, a reduction in astrocyte MDs following GluN1 KD may reduce the astrocyte energy supply, creating a "hungry", energy-deficient neuronal population, and leading to circuit dysfunction.

5. Conclusion

In conclusion, the results of this study provide evidence for the first time that astrocytic NMDAR mediates fast as well as delayed stimulation-evoked Ca^{2+} MDs in response to synaptic activity in awake mice, and contributes to normal cortical neuronal function, and sensory perception. We hypothesize that inhibitory neuron activity and cortical excitation-inhibition balance is disrupted when astrocyte NMDA receptors are lost. However, the underlying mechanisms of the observed results warrant future comprehensive research. Based on the literature, our results suggest the

involvement of gliotransmission, most probably ATP. A reduction in ATP following GluN1 KD potentially contributes to enhanced inhibition of pyramidal neurons and reduced disinhibition leading to reduced neuronal response to stimulation and ultimately, impaired sensory perception behavior. This is strong evidence for involvement of astrocytes in regulating cortical networks.

The limitations of this study include: 1) we do not have a reference for neuronal function before virus injection and GluN1 KD. Therefore, we are only able to draw a comparative conclusion. Future studies using Cre-induced GluN1 KD in astrocytes enables studying neuronal activity in same cells before and after reduction of NMDAR. 2) We did not consider the state of the animal right before delivering whisker stimulation. In fact, whether the animal was freely whisking or not has a determining role in the cellular response to stimulation [210]. Future studies will employ an infrared camera to always observe the whisking state of the animal during whisker stimulation. 3) More behavior tasks are required to determine the extent of discrimination inability in GluN1 KD animals and also to investigate if they are unable to detect the sensory stimulation. WMDT with larger texture differences could determine to what extent discrimination ability is distorted. If GluN1 KD animals are able to discriminate between average particle size difference of >=150 um, they do possess some levels of discrimination. 4) Active touch is possibly processed differently than passive stimulation. While passive whisker stimulation sufficiently fulfilled the needs of this study which is providing physiological stimulation and synaptic activity, drawing more precise conclusions about behavioral impacts and the involved microcircuits requires more detailed behavior tasks. For example, performing two alternative forced-choice whisker discrimination where animals must discriminate between two different frequency vibration of right and left whiskers and lick the corresponding water spout for a water reward can indicate if animals can perceive the stimulus, but also their level of sensory impairment. 5) Our technique does not allow us to identify the type of neuron that was recorded in this study. Labeling specific neuronal populations, pyramidal, PV, and SST neurons, by driving GECIs expression under cell-specific promoter could overcome this limitation and provide more detailed insight into the astrocytic NMDAR impacts on different neuronal populations which is essential for better understanding of cortical circuit activity.

Growing evidence suggest important roles for astrocytes in healthy brain function and as potential future targets of brain disorders. Astrocyte-released ATP [66] and D-serine [69] have anti-depressant impacts in depression mouse models and ATP can rescue repetitive behavior, an autism spectrum disorder-like behavior [67]. Recently, astrocytes were shown to dynamically regulate cortical network sensory-evoked Gamma activity, which is importantly involved in sensory

integration and attention, in a Ca^{2+}-dependent manner[61]. A deep understanding of mechanisms underlying astrocytes Ca^{2+} MDs and their influence on neuronal network in healthy brain therefore is crucial for moving forward to using these cells as therapeutic targets in disease. This study reveals for the first time the physiological and behavioral importance of NMDARs in astrocytes function in neuronal networks and opens doors for future studies investigating the role of these receptors in diseases such as schizophrenia where astrocytic NMDARs are hypofunctional [226].

6. References

1. Verkhratsky A, Nedergaard M. Physiology of astroglia. *Physiol Rev*. 2018;98(1):239-389. doi:10.1152/physrev.00042.2016

2. Henneberger C, Papouin T, Oliet SHR, Rusakov DA. Long-term potentiation depends on release of d-serine from astrocytes. *Nature*. 2010;463(7278):232-236. doi:10.1038/nature08673

3. Matos M, Bosson A, Riebe I, et al. Astrocytes detect and upregulate transmission at inhibitory synapses of somatostatin interneurons onto pyramidal cells. *Nat Commun*. 2018;9(1). doi:10.1038/s41467-018-06731-y

4. Panatier A, Vallée J, Haber M, Murai KK, Lacaille JC, Robitaille R. Astrocytes are endogenous regulators of basal transmission at central synapses. *Cell*. 2011;146(5):785-798. doi:10.1016/j.cell.2011.07.022

5. Attwell D, Buchan AM, Charpak S, Lauritzen M, MacVicar BA, Newman EA. Glial and neuronal control of brain blood flow. *Nature*. 2010;468(7321):232-243. doi:10.1038/nature09613

6. Verkhratsky A, Butt A. *Glial Physiology and Pathophysiology*. John Wiley and Sons; 2013. doi:10.1002/9781118402061

7. Matyash V, Kettenmann H. Heterogeneity in astrocyte morphology and physiology. *Brain Res Rev*. 2010;63(1-2):2-10. doi:10.1016/j.brainresrev.2009.12.001

8. Kimelberg HK. The problem of astrocyte identity. *Neurochem Int*. 2004;45(2-3):191-202. doi:10.1016/j.neuint.2003.08.015

9. Khakh BS, Sofroniew M V. Diversity of astrocyte functions and phenotypes in neural circuits. *Nat Neurosci*. 2015;18(7):942. doi:10.1038/NN.4043

10. Tong X, Shigetomi E, Looger LL, Khakh BS. Genetically encoded calcium indicators and astrocyte calcium microdomains. *Neuroscientist*. 2013;19(3):274-291. doi:10.1177/1073858412468794

11. Ahmadpour N, Kantroo M, Stobart JL. Extracellular Calcium Influx Pathways in Astrocyte Calcium Microdomain Physiology. *Biomolecules*. 2021;11(10). doi:10.3390/BIOM11101467

12. Bazargani N, Attwell D. Astrocyte calcium signaling: The third wave. *Nat Neurosci*. 2016;19(2):182-189. doi:10.1038/nn.4201

13. Ogata K, Kosaka T. Structural and quantitative analysis of astrocytes in the mouse hippocampus. *Neuroscience*. 2002;113(1):221-233. doi:10.1016/S0306-4522(02)00041-6

14. Haustein MD, Kracun S, Lu XH, et al. Conditions and constraints for astrocyte calcium signaling in the hippocampal mossy fiber pathway. *Neuron*. 2014;82(2):413-429. doi:10.1016/j.neuron.2014.02.041

15. Nedergaard M, Ransom B, Goldman SA. New roles for astrocytes: Redefining the functional architecture of the brain. *Trends Neurosci*. 2003;26(10):523-530. doi:10.1016/j.tins.2003.08.008

16. Halassa MM, Fellin T, Takano H, Dong JH, Haydon PG. Synaptic islands defined by the territory of a single astrocyte. *J Neurosci*. 2007;27(24):6473-6477. doi:10.1523/JNEUROSCI.1419-07.2007

17. Bushong EA, Martone ME, Jones YZ, Ellisman MH. Protoplasmic Astrocytes in CA1 Stratum Radiatum Occupy Separate Anatomical Domains. 2002;22(1). /pmc/articles/PMC6757596/. Accessed March 9, 2020.

18. Kimelberg HK. Receptors on astrocytes-what possible functions? *Neurochem Int*. 1995;26(1):27-40. doi:10.1016/0197-0186(94)00118-E

19. Verkhratsky A, Steinhäuser C. Ion channels in glial cells. *Brain Res Rev*. 2000;32(2-3):380-412. doi:10.1016/S0165-0173(99)00093-4

20. Angulo MC, Kozlov AS, Charpak S, Audinat E. Glutamate Released from Glial Cells Synchronizes Neuronal Activity in the Hippocampus. *J Neurosci*. 2004;24(31):6920 LP - 6927. doi:10.1523/JNEUROSCI.0473-04.2004

21. Bezzi P, Carmignoto G, Pasti L, et al. Prostaglandins stimulate calcium-dependent glutamate release in astrocytes. *Nature*. 1998;391(6664):281-285. doi:10.1038/34651

22. Fellin T, Pascual O, Gobbo S, Pozzan T, Haydon PG, Carmignoto G. Neuronal synchrony mediated by astrocytic glutamate through activation of extrasynaptic NMDA receptors. *Neuron*. 2004;43(5):729-743. doi:10.1016/j.neuron.2004.08.011

23. Kang J, Jiang L, Goldman SA, Nedergaard M. Astrocyte-mediated potentiation of inhibitory synaptic transmission. *Nat Neurosci*. 1998;1(8):683-692. doi:10.1038/3684

24. Pasti L, Volterra A, Pozzan T, Carmignoto G. Intracellular calcium oscillations in astrocytes: A highly plastic, bidirectional form of communication between neurons and astrocytes in situ. *J Neurosci*. 1997;17(20):7817-7830. doi:10.1523/jneurosci.17-20-07817.1997

25. Vladimir Parpura, Trent A. Basarsky, Fang Liutt, Ksenija Jeftinijatt, Srdija JeftinijaH PGH. Glutamate-mediated astrocyte-neuron signalling. *Nature*. 1994;369(JUNE):744-747. doi:10.1038/369744a0

26. Hertz L, Gibbs ME, Dienel GA. Fluxes of lactate into, from, and among gap junction-coupled astrocytes and their interaction with noradrenaline. *Front Neurosci*. 2014;8(SEP):1-8. doi:10.3389/fnins.2014.00261

27. Mächler P, Wyss MT, Elsayed M, et al. In Vivo Evidence for a Lactate Gradient from Astrocytes to Neurons. *Cell Metab*. 2016;23(1):94-102. https://pubmed.ncbi.nlm.nih.gov/26698914/. Accessed May 5, 2022.

28. Magistretti PJ, Allaman I. A Cellular Perspective on Brain Energy Metabolism and Functional Imaging. *Neuron*. 2015;86(4):883-901. doi:10.1016/j.neuron.2015.03.035

29. Zuend M, Saab AS, Wyss MT, et al. Arousal-induced cortical activity triggers lactate release from astrocytes. *Nat Metab*. 2020;2(2). doi:10.1038/s42255-020-0170-4

30. Kozlov AS, Angulo MC, Audinat E, Charpak S. Target cell-specific modulation of neuronal activity by astrocytes. *Proc Natl Acad Sci*. 2006;103(26):10058 LP - 10063. doi:10.1073/pnas.0603741103

31. Lee S, Yoon BE, Berglund K, et al. Channel-mediated tonic GABA release from glia.

Science (80-). 2010;330(6005):790-796. doi:10.1126/SCIENCE.1184334/SUPPL_FILE/LEE.SOM.PDF

32. Araque A, Carmignoto G, Haydon PG, Oliet SHR, Robitaille R, Volterra A. Gliotransmitters travel in time and space. *Neuron*. 2014;81(4):728-739. doi:10.1016/j.neuron.2014.02.007

33. Bonansco C, Couve A, Perea G, Ferradas CÁ, Roncagliolo M, Fuenzalida M. Glutamate released spontaneously from astrocytes sets the threshold for synaptic plasticity. *Eur J Neurosci*. 2011;33(8):1483-1492. doi:10.1111/J.1460-9568.2011.07631.X

34. Di Castro MA, Chuquet J, Liaudet N, et al. Local Ca2+ detection and modulation of synaptic release by astrocytes. *Nat Neurosci*. 2011;14(10):1276-1284. doi:10.1038/nn.2929

35. Gómez-Gonzalo M, Navarrete M, Perea G, et al. Endocannabinoids Induce Lateral Long-Term Potentiation of Transmitter Release by Stimulation of Gliotransmission. *Cereb Cortex*. 2015;25(10):3699-3712. https://academic-oup-com.uml.idm.oclc.org/cercor/article/25/10/3699/390461. Accessed May 31, 2022.

36. Jourdain P, Bergersen LH, Bhaukaurally K, et al. Glutamate exocytosis from astrocytes controls synaptic strength. *Nat Neurosci*. 2007;10(3):331-339. doi:10.1038/nn1849

37. Navarrete M, Perea G, de Sevilla DF, et al. Astrocytes mediate in vivo cholinergic-induced synaptic plasticity. *PLoS Biol*. 2012;10(2):e1001259. doi:10.1371/journal.pbio.1001259

38. Perea G, Araque A. Astrocytes potentiate transmitter release at single hippocampal synapses. *Science (80-)*. 2007;317(5841):1083-1086. doi:10.1126/science.1144640

39. Serrano A, Haddjeri N, Lacaille JC, Robitaille R. GABAergic network activation of glial cells underlies hippocampal heterosynaptic depression. *J Neurosci*. 2006;26(20):5370-5382. doi:10.1523/JNEUROSCI.5255-05.2006

40. Pascual O, Casper KB, Kubera C, et al. Astrocytic purinergic signaling coordinates synaptic networks. 2005;310(5745):113-116. https://pubmed.ncbi.nlm.nih.gov/16210541/. Accessed March 7, 2020.

41. Bergersen LH, Morland C, Ormel L, et al. Immunogold detection of L-glutamate and D-serine in small synaptic-like microvesicles in adult hippocampal astrocytes. *Cereb Cortex*. 2012;22(7):1690-1697. doi:10.1093/cercor/bhr254

42. Panatier A, Theodosis DT, Mothet JP, et al. Glia-derived D-serine controls NMDA receptor activity and synaptic memory. *Cell*. 2006;125(4):775-784. doi:10.1016/J.CELL.2006.02.051

43. Koh W, Park M, Chun YE, et al. Astrocytes render memory flexible. *bioRxiv*. March 2021:2021.03.25.436945. doi:10.1101/2021.03.25.436945

44. Bernardinelli Y, Randall J, Janett E, et al. Activity-dependent structural plasticity of perisynaptic astrocytic domains promotes excitatory synapse stability. *Curr Biol*. 2014;24(15):1679-1688. doi:10.1016/j.cub.2014.06.025

45. Molotkov D, Zobova S, Arcas JM, Khiroug L. Calcium-induced outgrowth of astrocytic peripheral processes requires actin binding by Profilin-1. *Cell Calcium*. 2013;53(5-6):338-348. doi:10.1016/j.ceca.2013.03.001

46. Tanaka M, Shih P-Y, Gomi H, et al. Astrocytic Ca2+ signals are required for the functional integrity of tripartite synapses. *Mol Brain*. 2013;6(1):6. doi:10.1186/1756-6606-6-6

47. Bernardinelli Y, Muller D, Nikonenko I. Astrocyte-synapse structural plasticity. *Neural Plast*. 2014;2014. doi:10.1155/2014/232105

48. Rosenegger DG, Tran CHTHT, Wamsteeker Cusulin JI, Gordon GR. Tonic local brain blood flow control by astrocytes independent of phasic neurovascular coupling. *J Neurosci*. 2015;35(39):13463-13474. doi:10.1523/JNEUROSCI.1780-15.2015

49. Haidey JN, Peringod G, Institoris A, et al. Astrocytes regulate ultra-slow arteriole oscillations via stretch-mediated TRPV4-COX-1 feedback. *Cell Rep*. 2021;36(5):109405. doi:10.1016/j.celrep.2021.109405

50. Gordon GRJ, Choi HB, Rungta RL, Ellis-Davies GCR, MacVicar BA. Brain metabolism dictates the polarity of astrocyte control over arterioles. *Nature*. 2008;456(7223):745-750. doi:10.1038/nature07525

51. Mulligan SJ, MacVicar BA. Calcium transients in astrocyte endfeet cause cerebrovascular constrictions. *Nature*. 2004;431(7005):195-199. doi:10.1038/nature02827

52. Zonta M, Angulo MC, Gobbo S, et al. Neuron-to-astrocyte signaling is central to the dynamic control of brain microcirculation. *Nat Neurosci*. 2003;6(1):43-50. doi:10.1038/nn980

53. Lind BL, Jessen SB, Lønstrup M, Joséphine C, Bonvento G, Lauritzen M. Fast Ca 2+ responses in astrocyte end-feet and neurovascular coupling in mice. *Glia*. 2018;66(2):348-358. doi:10.1002/glia.23246

54. Lind BL, Brazhe AR, Jessen SB, Tan FCCC, Lauritzen MJ. Rapid stimulus-evoked astrocyte Ca2+ elevations and hemodynamic responses in mouse somatosensory cortex in vivo. *Proc Natl Acad Sci U S A*. 2013;110(48). doi:10.1073/pnas.1310065110

55. Otsu Y, Couchman K, Lyons DG, et al. Calcium dynamics in astrocyte processes during neurovascular coupling. *Nat Neurosci*. 2015;18(2):210-218. doi:10.1038/nn.3906

56. Nizar K, Uhlirova H, Tian P, et al. In vivo stimulus-induced vasodilation occurs without IP3 receptor activation and may precede astrocytic calcium increase. *J Neurosci*. 2013;33(19):8411-8422. doi:10.1523/JNEUROSCI.3285-12.2013

57. Sharma K, Gordon GRJ, Tran CHT. Heterogeneity of Sensory-Induced Astrocytic Ca2+ Dynamics During Functional Hyperemia. *Front Physiol*. 2020;11(December). doi:10.3389/fphys.2020.611884

58. Tran CHT, Peringod G, Gordon GR. Astrocytes Integrate Behavioral State and Vascular Signals during Functional Hyperemia. *Neuron*. 2018;100(5):1133-1148.e3. doi:10.1016/j.neuron.2018.09.045

59. Poskanzer KE, Yuste R. Astrocytic regulation of cortical UP states. *Proc Natl Acad Sci U S A*. 2011;108(45):18453-18458. doi:10.1073/pnas.1112378108

60. Poskanzer KE, Yuste R. Astrocytes regulate cortical state switching in vivo. *Proc Natl Acad Sci U S A*. 2016;113(19):E2675-E2684. doi:10.1073/pnas.1520759113

61. Lines J, Martin ED, Kofuji P, Aguilar J, Araque A. Astrocytes modulate sensory-evoked

neuronal network activity. *Nat Commun 2020 111*. 2020;11(1):1-12. doi:10.1038/S41467-020-17536-3

62. Paukert M, Agarwal A, Cha J, Doze VA, Kang JU, Bergles DE. Norepinephrine controls astroglial responsiveness to local circuit activity. *Neuron*. 2014;82(6):1263-1270. doi:10.1016/j.neuron.2014.04.038

63. Ding F, O'Donnell J, Thrane AS, et al. α1-adrenergic receptors mediate coordinated Ca^{2+} signaling of cortical astrocytes in awake, behaving mice. *Cell Calcium*. 2013;54(6):387-394. doi:10.1016/j.ceca.2013.09.001

64. Agarwal A, Wu PH, Hughes EG, et al. Transient Opening of the Mitochondrial Permeability Transition Pore Induces Microdomain Calcium Transients in Astrocyte Processes. *Neuron*. 2017;93(3):587-605.e7. doi:10.1016/j.neuron.2016.12.034

65. Srinivasan R, Huang BS, Venugopal S, et al. Ca2+ signaling in astrocytes from Ip3r2−/− mice in brain slices and during startle responses in vivo. *Nat Neurosci*. 2015;18(5):708-717. doi:10.1038/nn.4001

66. Cao X, Li LP, Wang Q, et al. Astrocyte-derived ATP modulates depressive-like behaviors. 2013;19(6):773-777. https://www-nature-com.uml.idm.oclc.org/articles/nm.3162. Accessed June 2, 2022.

67. Wang Q, Kong Y, Wu DY, et al. Impaired calcium signaling in astrocytes modulates autism spectrum disorder-like behaviors in mice. *Nat Commun 2021 121*. 2021;12(1):1-13. doi:10.1038/S41467-021-23843-0

68. Khakh BS, Gittermann D, Cockayne DA, Jones A. ATP Modulation of Excitatory Synapses onto Interneurons. 2003.

69. Chen Z, Tang Z, Zou K, et al. d-Serine produces antidepressant-like effects in mice through suppression of BDNF signaling pathway and regulation of synaptic adaptations in the nucleus accumbens. *Mol Med*. 2021;27(1):1-13. doi:10.1186/S10020-021-00389-X/FIGURES/6

70. Losi G, Mariotti L, Sessolo M, Carmignoto G. New tools to study astrocyte Ca2+ signal dynamics in brain networks in vivo. *Front Cell Neurosci*. 2017;11. doi:10.3389/fncel.2017.00134

71. Mishchenko Y, Hu T, Spacek J, Mendenhall J, Harris KM, Chklovskii DB. Ultrastructural analysis of hippocampal neuropil from the connectomics perspective. *Neuron*. 2010;67(6):1009-1020. doi:10.1016/j.neuron.2010.08.014

72. Ventura R, Harris KM. Three-dimensional relationships between hippocampal synapses and astrocytes. *J Neurosci*. 1999;19(16):6897-6906. doi:10.1523/jneurosci.19-16-06897.1999

73. Reeves AMB, Shigetomi E, Khakh BS. Bulk loading of calcium indicator dyes to study astrocyte physiology: Key limitations and improvements using morphological maps. *J Neurosci*. 2011;31(25):9353-9358. doi:10.1523/JNEUROSCI.0127-11.2011

74. Fiacco TA, McCarthy KD. Intracellular Astrocyte Calcium Waves In Situ Increase the Frequency of Spontaneous AMPA Receptor Currents in CA1 Pyramidal Neurons. *J Neurosci*. 2004;24(3):722-732. doi:10.1523/JNEUROSCI.2859-03.2004

75. Parri HR, Gould TM, Crunelli V. Spontaneous astrocytic Ca2+ oscillations in situ drive

NMDAR-mediated neuronal excitation. *Nat Neurosci*. 2001;4(8):803-812. doi:10.1038/90507

76. James T. Porter and Ken D. McCarthy. Hippocampal Astrocytes In Situ Respond to Glutamate Released from Synaptic Terminals James. *J Neurosci*. 1996;16(16):5073-5081. doi:10.1523/jneurosci.16-16-05073.1996

77. Zhang Y, Chen K, Sloan SA, et al. An RNA-Sequencing Transcriptome and Splicing Database of Glia, Neurons, and Vascular Cells of the Cerebral Cortex. *J Neurosci*. 2014;34(36):11929 LP - 11947. doi:10.1523/JNEUROSCI.1860-14.2014

78. Cahoy JD, Emery B, Kaushal A, et al. A transcriptome database for astrocytes, neurons, and oligodendrocytes: A new resource for understanding brain development and function. *J Neurosci*. 2008;28(1):264-278. doi:10.1523/JNEUROSCI.4178-07.2008

79. Cai Z, Kimelberg HK. *Glutamate Receptor-Mediated Calcium Responses in Acutely Isolated Hippocampal Astrocytes*. Vol 21. Wiley-Liss, Inc; 1997. doi:10.1002/(SICI)1098-1136(199712)21:4

80. Sun W, McConnell E, Pare J-FF, et al. Glutamate-dependent neuroglial calcium signaling differs between young and adult brain. *Science (80-)*. 2013;339(6116):197-200. doi:10.1126/science.1226740

81. Patrushev I, Gavrilov N, Turlapov V, Semyanov A. Subcellular location of astrocytic calcium stores favors extrasynaptic neuron-astrocyte communication. *Cell Calcium*. 2013;54(5):343-349. doi:10.1016/j.ceca.2013.08.003

82. Fiacco TA, Agulhon C, Taves SR, et al. Selective Stimulation of Astrocyte Calcium In Situ Does Not Affect Neuronal Excitatory Synaptic Activity. *Neuron*. 2007;54(4):611-626. doi:10.1016/j.neuron.2007.04.032

83. Petravicz J, Fiacco TA, McCarthy KD. Loss of IP3 receptor-dependent Ca2+ increases in hippocampal astrocytes does not affect baseline CA1 pyramidal neuron synaptic activity. *J Neurosci*. 2008;28(19):4967-4973. doi:10.1523/JNEUROSCI.5572-07.2008

84. Agulhon C, Fiacco TA, McCarthy KD. Hippocampal short- and long-term plasticity are not modulated by astrocyte Ca2+ signaling. *Science (80-)*. 2010;327(5970):1250-1254. doi:10.1126/science.1184821

85. Bonder DE, McCarthy KD. Astrocytic Gq-GPCR-linked IP3R-Dependent Ca2+ signaling does not mediate neurovascular coupling in mouse visual cortex in vivo. *J Neurosci*. 2014;34(39):13139-13150. doi:10.1523/JNEUROSCI.2591-14.2014

86. Petravicz J, Boyt KM, McCarthy KD. Astrocyte IP3R2-dependent Ca2+ signaling is not a major modulator of neuronal pathways governing behavior. *Front Behav Neurosci*. 2014;8(November):1-13. doi:10.3389/fnbeh.2014.00384

87. Schulz K, Sydekum E, Krueppel R, et al. Simultaneous BOLD fMRI and fiber-optic calcium recording in rat neocortex. *Nat Methods*. 2012;9(6):597-602. doi:10.1038/nmeth.2013

88. Schummers, J., Yu, H. & Sur M. Tuned Responses of Astrocytes and Their Influence on Hemodynamic Signals in the Visual Cortex. *Science (80-)*. 2008;320(5883):1638-1643.

89. Wang X, Lou N, Xu Q, et al. Astrocytic Ca^{2+} signaling evoked by sensory stimulation *in vivo*. *Nat Neurosci*. 2006;9(6):816-823. doi:10.1038/nn1703

90. Arizono M, Inavalli VVGK, Panatier A, et al. Structural basis of astrocytic Ca2+ signals at tripartite synapses. *Nat Commun*. 2020;11(1):1906. doi:10.1038/s41467-020-15648-4

91. Bindocci E, Savtchouk I, Liaudet N, Becker D, Carriero G, Volterra A. Three-dimensional Ca2+ imaging advances understanding of astrocyte biology. *Science (80-)*. 2017;356(6339):eaai8185. doi:10.1126/science.aai8185

92. Shigetomi E, Bushong EA, Haustein MD, et al. Imaging calcium microdomains within entire astrocyte territories and endfeet with GCaMPs expressed using adeno-associated viruses. *J Gen Physiol*. 2013;141(5):633-647. doi:10.1085/jgp.201210949

93. Srinivasan R, Huang BS, Venugopal S, et al. Ca^{2+} signaling in astrocytes from Ip3r2 $^{-/-}$ mice in brain slices and during startle responses in vivo. *Nat Neurosci*. 2015;18(5):708-717. doi:10.1038/nn.4001

94. Stobart JL, Ferrari KD, Barrett MJP, et al. Cortical Circuit Activity Evokes Rapid Astrocyte Calcium Signals on a Similar Timescale to Neurons. *Neuron*. 2018;98(4):726-735.e4. doi:10.1016/j.neuron.2018.03.050

95. Stobart JL, Ferrari KD, Barrett MJPP, et al. Long-term in vivo calcium imaging of astrocytes reveals distinct cellular compartment responses to sensory stimulation. *Cereb Cortex*. 2018;28(1):184-198. doi:10.1093/cercor/bhw366

96. Grosche J, Matyash V, Möller T, Verkhratsky A, Reichenbach A, Kettenmann H. Microdomains for neuron-glia interaction: Parallel fiber signaling to Bergmann glial cells. *Nat Neurosci*. 1999;2(2):139-143. doi:10.1038/5692

97. Asada A, Ujita S, Nakayama R, et al. Subtle modulation of ongoing calcium dynamics in astrocytic microdomains by sensory inputs. *Physiol Rep*. 2015;3(10). doi:10.14814/phy2.12454

98. Denizot A, Arizono M, Valentin Nägerl U, Soula H, Berry H. *Simulation of Calcium Signaling in Fine Astrocytic Processes: Effect of Spatial Properties on Spontaneous Activity*. Vol 15.; 2019. doi:10.1371/journal.pcbi.1006795

99. Holtzclaw LA, Pandhit S, Bare DJ, Mignery GA, Russell JT. Astrocytes in adult rat brain express type 2 inositol 1,4,5-trisphosphate receptors. *Glia*. 2002;39(1):69-84. doi:10.1002/glia.10085

100. Rungta RL, Bernier LP, Dissing-Olesen L, et al. Ca2+ transients in astrocyte fine processes occur via Ca2+ influx in the adult mouse hippocampus. *Glia*. 2016;64(12):2093-2103. doi:10.1002/glia.23042

101. Shigetomi E, Jackson-Weaver O, Huckstepp RT, O'Dell TJ, Khakh BS. TRPA1 channels are regulators of astrocyte basal calcium levels and long-term potentiation via constitutive d-serine release. *J Neurosci*. 2013;33(24):10143-10153. doi:10.1523/JNEUROSCI.5779-12.2013

102. Zlatkine P, Mehul B, Magee AI. Retargeting of cytosolic proteins to the plasma membrane by the Lck protein tyrosine kinase dual acylation motif. *J Cell Sci*. 1997;110 (Pt 5)(5):673-679. doi:10.1242/JCS.110.5.673

103. Axel Nimmerjahn, Eran A. Mukamel and MJS. Motor Behavior Activates Bergmann Glial Networks. *Neuron*. 2009;62(3):400-412. doi:10.1038/jid.2014.371

104. Hirase H, Qian L, Barthó P, Buzsáki G. Calcium dynamics of cortical astrocytic networks

in vivo. *PLoS Biol*. 2004;2(4):494-499. doi:10.1371/journal.pbio.0020096

105. Kanemaru K, Sekiya H, Xu M, et al. In Vivo visualization of subtle, transient, and local activity of astrocytes using an ultrasensitive Ca 2+ indicator. *Cell Rep*. 2014;8(1):311-318. doi:10.1016/j.celrep.2014.05.056

106. Wang X, Lou N, Xu Q, et al. Astrocytic Ca2+ signaling evoked by sensory stimulation in vivo. *Nat Neurosci*. 2006;9(6):816-823. doi:10.1038/nn1703

107. Tang W, Szokol K, Jensen V, et al. Stimulation-evoked Ca2+ signals in astrocytic processes at hippocampal CA3-CA1 synapses of adult mice are modulated by glutamate and ATP. *J Neurosci*. 2015;35(7):3016-3021. doi:10.1523/JNEUROSCI.3319-14.2015

108. Graham L. Collingridge, Richard W. Olsen, John Peters and MS. A nomenclature for ligand-gated ion channels. *Neuropharmacology*. 2009;56(1):2-5. doi:10.1038/jid.2014.371

109. Vyklicky V, Korinek M, Smejkalova T, et al. Structure, function, and pharmacology of NMDA receptor channels. *Physiol Res*. 2014;63(SUPPL.).

110. Ciabarra AM, Sullivan JM, Gahn LG, Pecht G, Heinemann S, Sevarino KA. Cloning and characterization of chi-1: a developmentally regulated member of a novel class of the ionotropic glutamate receptor family. *J Neurosci*. 1995;15(10):6498-6508. doi:10.1523/JNEUROSCI.15-10-06498.1995

111. Ishii T, Moriyoshi K, Sugihara H, et al. Molecular Characterization of the Family of the N-Methyl-D-Aspartate Receptor Subunits*. *J Biol Chem*. 1993;268(4):2836-2843. doi:10.1016/S0021-9258(18)53849-7

112. Skowrońska K, Obara-Michlewska M, Zielińska M, Albrecht J. NMDA receptors in astrocytes: In search for roles in neurotransmission and astrocytic homeostasis. *Int J Mol Sci*. 2019;20(2). doi:10.3390/ijms20020309

113. Dingledine R, Borges K, Bowie D, Traynelis SF. The glutamate receptor ion channels. *Pharmacol Rev*. 1999;51(1):7-61.

114. Schüler T, Mesic I, Madry C, Bartholoma I, Laube B. Formation of NR1/NR2 and NR1/NR3 heterodimers constitutes the initial step in N-methyl-D-aspartate receptor assembly. *J Biol Chem*. 2008;283(1):37-46. doi:10.1074/jbc.M703539200

115. Qian A, Johnson JW. Permeant ion effects on external Mg2+ block of NR1/2D NMDA receptors. *J Neurosci*. 2006;26(42):10899-10910. doi:10.1523/JNEUROSCI.3453-06.2006

116. Henson MA, Roberts AC, Pérez-Otaño I, Philpot BD. Influence of the NR3A subunit on NMDA receptor functions. *Prog Neurobiol*. 2010;91(1):23-37. doi:10.1016/j.pneurobio.2010.01.004

117. Traynelis SF, Wollmuth LP, McBain CJ, et al. Glutamate receptor ion channels: Structure, regulation, and function. *Pharmacol Rev*. 2010;62(3):405-496. doi:10.1124/pr.109.002451

118. Lalo U, Pankratov Y, Kirchhoff F, North RA, Verkhratsky A. NMDA Receptors Mediate Neuron-to-Glia Signaling in Mouse Cortical Astrocytes. *J Neurosci*. 2006;26(10):2673 LP - 2683. doi:10.1523/JNEUROSCI.4689-05.2006

119. Palygin O, Lalo U, Pankratov Y. Distinct pharmacological and functional properties of

NMDA receptors in mouse cortical astrocytes. *Br J Pharmacol*. 2011;163(8):1755-1766. doi:10.1111/j.1476-5381.2011.01374.x

120. Sasaki YF, Rothe T, Premkumar LS, et al. Characterization and comparison of the NR3A subunit of the NMDA receptor in recombinant systems and primary cortical neurons. *J Neurophysiol*. 2002;87(4):2052-2063. doi:10.1152/JN.00531.2001

121. Roberts AC, Díez-García J, Rodriguiz RM, et al. Downregulation of NR3A-containing NMDARs is required for synapse maturation and memory consolidation. *Neuron*. 2009;63(3):342-356. doi:10.1016/J.NEURON.2009.06.016

122. Pérez-Otaño I, Larsen RS, Wesseling JF. Emerging roles of GluN3-containing NMDA receptors in the CNS. *Nat Rev Neurosci 2016 1710*. 2016;17(10):623-635. doi:10.1038/NRN.2016.92

123. Tong G, Takahashi H, Tu S, et al. Modulation of NMDA receptor properties and synaptic transmission by the NR3A subunit in mouse hippocampal and cerebrocortical neurons. *J Neurophysiol*. 2008;99(1):122-132. doi:10.1152/JN.01044.2006

124. Matsuda K, Fletcher M, Kamiya Y, Yuzaki M. Specific assembly with the NMDA receptor 3B subunit controls surface expression and calcium permeability of NMDA receptors. *J Neurosci*. 2003;23(31):10064-10073. doi:10.1523/JNEUROSCI.23-31-10064.2003

125. Lee MC, Ting KK, Adams S, Brew BJ, Chung R, Guillemin GJ. Characterisation of the expression of NMDA receptors in human astrocytes. *PLoS One*. 2010;5(11):e14123. doi:10.1371/journal.pone.0014123

126. Verkhratsky A, Chvátal A. NMDA Receptors in Astrocytes. *Neurochem Res*. 2020;45(1):122-133. doi:10.1007/s11064-019-02750-3

127. Dzamba D, Honsa P, Valny M, et al. Quantitative Analysis of Glutamate Receptors in Glial Cells from the Cortex of GFAP/EGFP Mice Following Ischemic Injury: Focus on NMDA Receptors. *Cell Mol Neurobiol*. 2015;35(8):1187-1202. doi:10.1007/s10571-015-0212-8

128. Lalo U, Palygin O, Rasooli-Nejad S, Andrew J, Haydon PG, Pankratov Y. Exocytosis of ATP From Astrocytes Modulates Phasic and Tonic Inhibition in the Neocortex. *PLoS Biol*. 2014;12(1). doi:10.1371/journal.pbio.1001747

129. Lalo U, Palygin O, North RA, Verkhratsky A, Pankratov Y. Age-dependent remodelling of ionotropic signalling in cortical astroglia. *Aging Cell*. 2011;10(3):392-402. doi:10.1111/j.1474-9726.2011.00682.x

130. Palygin O, Lalo U, Verkhratsky A, Pankratov Y. Ionotropic NMDA and P2X1/5 receptors mediate synaptically induced Ca2+ signalling in cortical astrocytes. *Cell Calcium*. 2010;48(4):225-231. doi:10.1016/j.ceca.2010.09.004

131. Mehina EMFF, Murphy-Royal C, Gordon GR. Steady-State Free Ca2+ in Astrocytes Is Decreased by Experience and Impacts Arteriole Tone. *J Neurosci*. 2017;37(34):8150-8165. doi:10.1523/JNEUROSCI.0239-17.2017

132. Schipke CG, Ohlemeyer C, Matyash M, Nolte C, Kettenmann H, Kirchhoff F. Astrocytes of the mouse neocortex express functional N-methyl-D-aspartate receptors. *FASEB J*. 2001;15(7):1270-1272. doi:10.1096/fj.00-0439fje

133. Letellier M, Park YK, Chater TE, et al. Astrocytes regulate heterogeneity of presynaptic

strengths in hippocampal networks. *Proc Natl Acad Sci U S A*. 2016;113(19):E2685-E2694. doi:10.1073/pnas.1523717113

134. Jimenez-Blasco D, Santofimia-Castanõ P, Gonzalez A, Almeida A, Bolanõs JP. Astrocyte NMDA receptors' activity sustains neuronal survival through a Cdk5-Nrf2 pathway. *Cell Death Differ*. 2015;22(11):1877-1889. doi:10.1038/cdd.2015.49

135. Chipman PH, Fernandez AP, Chung C, et al. Astrocyte GluN2C NMDA receptors control basal synaptic strengths of hippocampal CA1 pyramidal neurons in the stratum radiatum. *bioRxiv*. May 2021:2021.05.28.446253. doi:10.1101/2021.05.28.446253

136. King CM, Bohmbach K, Minge D, et al. Local Resting Ca2+ Controls the Scale of Astroglial Ca2+ Signals. *Cell Rep*. 2020;30(10):3466-3477.e4. doi:10.1016/j.celrep.2020.02.043

137. Zheng K, Bard L, Reynolds JP, et al. Time-resolved imaging reveals heterogeneous landscapes of nanomolar Ca2+ in neurons and astroglia. *Neuron*. 2015;88(2):277-288. doi:10.1016/j.neuron.2015.09.043

138. Woolsey TA, Van der Loos H. The structural organization of layer IV in the somatosensory region (S I) of mouse cerebral cortex. The description of a cortical field composed of discrete cytoarchitectonic units. *Brain Res*. 1970;17(2):205-242. doi:10.1016/0006-8993(70)90079-X

139. Simons DJ, Woolsey TA. Functional organization in mouse barrel cortex. *Brain Res*. 1979;165(2):327-332. doi:10.1016/0006-8993(79)90564-X

140. Deschênes M, Timofeeva E, Lavallée P. The Relay of High-Frequency Sensory Signals in the Whisker-to-Barreloid Pathway. *J Neurosci*. 2003;23(17):6778. doi:10.1523/JNEUROSCI.23-17-06778.2003

141. Arnold PB, Li CX, Waters RS. Thalamocortical arbors extend beyond single cortical barrels: an in vivo intracellular tracing study in rat. *Exp brain Res*. 2001;136(2):152-168. doi:10.1007/S002210000570

142. Feldmeyer D, Lübke J, Silver RA, Sakmann B. Synaptic connections between layer 4 spiny neurone- layer 2/3 pyramidal cell pairs in juvenile rat barrel cortex: physiology and anatomy of interlaminar signalling within a cortical column. *J Physiol*. 2002;538(Pt 3):803. doi:10.1113/JPHYSIOL.2001.012959

143. Lefort S, Tomm C, Floyd Sarria JC, Petersen CCH. The excitatory neuronal network of the C2 barrel column in mouse primary somatosensory cortex. *Neuron*. 2009;61(2):301-316. doi:10.1016/J.NEURON.2008.12.020

144. Ferezou I, Bolea S, Petersen CCH. Visualizing the Cortical Representation of Whisker Touch: Voltage-Sensitive Dye Imaging in Freely Moving Mice. *Neuron*. 2006;50(4):617-629. doi:10.1016/J.NEURON.2006.03.043

145. Petersen CCH, Crochet S. Synaptic computation and sensory processing in neocortical layer 2/3. *Neuron*. 2013;78(1):28-48. doi:10.1016/J.NEURON.2013.03.020

146. Petersen CCH. Sensorimotor processing in the rodent barrel cortex. *Nat Rev Neurosci*. 2019;20(9):533. doi:10.1038/S41583-019-0200-Y

147. Crochet S, Poulet JFA, Kremer Y, Petersen CCH. Synaptic mechanisms underlying sparse coding of active touch. *Neuron*. 2011;69(6):1160-1175.

doi:10.1016/J.NEURON.2011.02.022

148. Gentet LJ, Kremer Y, Taniguchi H, Huang ZJ, Staiger JF, Petersen CCH. Unique functional properties of somatostatin-expressing GABAergic neurons in mouse barrel cortex. *Nat Neurosci 2012 154*. 2012;15(4):607-612. doi:10.1038/NN.3051

149. Mayrhofer JM, Haiss F, Helmchen F, Weber B. Sparse, reliable, and long-term stable representation of periodic whisker deflections in the mouse barrel cortex. *Neuroimage*. 2015;115:52-63. doi:10.1016/j.neuroimage.2015.04.045

150. Field RE, D'amour JA, Tremblay R, et al. Heterosynaptic Plasticity Determines the Set Point for Cortical Excitatory-Inhibitory Balance. *Neuron*. 2020;106(5):842-854.e4. doi:10.1016/J.NEURON.2020.03.002

151. Pilz GA, Carta S, Stäuble A, Ayaz A, Jessberger S, Helmchen F. Functional Imaging of Dentate Granule Cells in the Adult Mouse Hippocampus. *J Neurosci*. 2016;36(28):7407-7414. doi:10.1523/JNEUROSCI.3065-15.2016

152. Ohkura M, Sasaki T, Kobayashi C, Ikegaya Y, Nakai J. An Improved Genetically Encoded Red Fluorescent Ca2+ Indicator for Detecting Optically Evoked Action Potentials. *PLoS One*. 2012;7(7):e39933. doi:10.1371/JOURNAL.PONE.0039933

153. Chang K, Marran K, Valentine A, Hannon GJ. Packaging shRNA retroviruses. *Cold Spring Harb Protoc*. 2013;2013(8):734-737. doi:10.1101/PDB.PROT076448

154. Fellmann C, Hoffmann T, Sridhar V, et al. An Optimized microRNA Backbone for Effective Single-Copy RNAi. *Cell Rep*. 2013;5(6):1704-1713. doi:10.1016/J.CELREP.2013.11.020

155. Barrett MJP, Ferrari KD, Stobart JL, Holub M, Weber B. CHIPS: an Extensible Toolbox for Cellular and Hemodynamic Two-Photon Image Analysis. *Neuroinformatics*. 2018;16(1):145-147. doi:10.1007/s12021-017-9344-y

156. Wu HPP, Ioffe JC, Iverson MM, Boon JM, Dyck RH. Novel, whisker-dependent texture discrimination task for mice. *Behav Brain Res*. 2013;237(1):238-242. doi:10.1016/j.bbr.2012.09.044

157. Mathis A, Mamidanna P, Cury KM, et al. DeepLabCut: markerless pose estimation of user-defined body parts with deep learning. *Nat Neurosci*. 2018;21(9):1281-1289. doi:10.1038/S41593-018-0209-Y

158. Ellefsen KL, Settle B, Parker I, Smith IF. An algorithm for automated detection, localization and measurement of local calcium signals from camera-based imaging. *Cell Calcium*. 2014;56(3):147-156. doi:10.1016/J.CECA.2014.06.003

159. Ali F, Kwan AC. Interpreting in vivo calcium signals from neuronal cell bodies, axons, and dendrites: a review. *Neurophotonics*. 2020;7(1):1. doi:10.1117/1.NPH.7.1.011402

160. de Melo Reis RA, Freitas HR, de Mello FG. Cell Calcium Imaging as a Reliable Method to Study Neuron–Glial Circuits. *Front Neurosci*. 2020;14:975. doi:10.3389/FNINS.2020.569361/BIBTEX

161. Georgiou L, Echeverría A, Georgiou A, Kuhn B. Ca+ activity maps of astrocytes tagged by axoastrocytic AAV transfer. *Sci Adv*. 2022;8(6):5371. doi:10.1126/SCIADV.ABE5371/SUPPL_FILE/SCIADV.ABE5371_MOVIES_S1_TO_S3.ZIP

162. Crochet S, Petersen CCH. Correlating whisker behavior with membrane potential in barrel cortex of awake mice. *Nat Neurosci 2006 95*. 2006;9(5):608-610. doi:10.1038/NN1690

163. Kerr JND, De Kock CPJ, Greenberg DS, Bruno RM, Sakmann B, Helmchen F. Spatial Organization of Neuronal Population Responses in Layer 2/3 of Rat Barrel Cortex. *J Neurosci*. 2007;27(48):13316-13328. doi:10.1523/JNEUROSCI.2210-07.2007

164. Margolis DJ, Lütcke H, Schulz K, et al. Reorganization of cortical population activity imaged throughout long-term sensory deprivation. *Nat Neurosci*. 2012;15(11):1539-1546. doi:10.1038/nn.3240

165. Brecht M, Roth A, Sakmann B. Dynamic receptive fields of reconstructed pyramidal cells in layers 3 and 2 of rat somatosensory barrel cortex. *J Physiol*. 2003;553(Pt 1):243. doi:10.1113/JPHYSIOL.2003.044222

166. Sato TR, Gray NW, Mainen ZF, Svoboda K. The Functional Microarchitecture of the Mouse Barrel Cortex. *PLOS Biol*. 2007;5(7):e189. doi:10.1371/JOURNAL.PBIO.0050189

167. Zhao J, Wang D, Wang JH. Barrel cortical neurons and astrocytes coordinately respond to an increased whisker stimulus frequency. *Mol Brain*. 2012;5(1):1-11. doi:10.1186/1756-6606-5-12/FIGURES/7

168. Lalo U, Pankratov Y, Parpura V, Verkhratsky A. Ionotropic receptors in neuronal-astroglial signalling: What is the role of “excitable” molecules in non-excitable cells. *Biochim Biophys Acta - Mol Cell Res*. 2011;1813(5):992-1002. doi:10.1016/j.bbamcr.2010.09.007

169. Mariotti L, Losi G, Lia A, et al. Interneuron-specific signaling evokes distinctive somatostatin-mediated responses in adult cortical astrocytes. *Nat Commun 2017 91*. 2018;9(1):1-14. doi:10.1038/S41467-017-02642-6

170. Winship IR, Plaa N, Murphy TH. Rapid astrocyte calcium signals correlate with neuronal activity and onset of the hemodynamic response in vivo. *J Neurosci*. 2007;27(23):6268-6272. doi:10.1523/JNEUROSCI.4801-06.2007

171. Montes de Oca Balderas P, Gonzalez Hernandez JR. NMDA Receptors in Astroglia: Chronology, Controversies, and Contradictions from a Complex Molecule. In: *Astrocyte-Physiology and Pathology*. InTech Open; 2018:51-89. doi:http://dx.doi.org/10.5772/57353

172. Jensen AM, Chiu SY. Fluorescence measurement of changes in intracellular calcium induced by excitatory amino acids in cultured cortical astrocytes. *J Neurosci*. 1990;10(4):1165-1175. doi:10.1523/jneurosci.10-04-01165.1990

173. Cornell-Bell AAH, Finkbeiner SM, Cooper MS, et al. Glutamate induces calcium waves in cultured astrocytes. *Science (80-)*. 1990;247(4941):470-473.

174. A V, M N, V P, S K. Sodium fluxes and astroglial function. *Adv Exp Med Biol*. 2013;961:295-305. doi:10.1007/978-1-4614-4756-6_25

175. Takuma K, Matsuda T, Hashimoto H, et al. Role of Na+-Ca2+ Exchanger in Agonist-Induced Ca2+ Signaling in Cultured Rat Astrocytes. *J Neurochem*. 1996;67(5):1840-1845. doi:10.1046/J.1471-4159.1996.67051840.X

176. WF G, PJ Y, M J, BK K, MP B. Sodium/calcium exchange in rat cortical astrocytes. *J Neurosci*. 1994;14(10):5834-5843. doi:10.1523/JNEUROSCI.14-10-05834.1994

177. Ziemens D, Oschmann F, Gerkau NJ, Rose CR. Heterogeneity of activity-induced sodium transients between astrocytes of the mouse hippocampus and neocortex: mechanisms and consequences. *J Neurosci*. 2019;39(14):2620-2634. doi:10.1523/jneurosci.2029-18.2019

178. Benz B, Grima G, Do KQ. Glutamate-induced homocysteic acid release from astrocytes: possible implication in glia-neuron signaling. *Neuroscience*. 2004;124(2):377-386. doi:10.1016/J.NEUROSCIENCE.2003.08.067

179. Reyes RC, Verkhratsky A, Parpura V. Plasmalemmal Na+/Ca2+ exchanger modulates Ca2+-dependent exocytotic release of glutamate from rat cortical astrocytes. *ASN Neuro*. 2012;4(1):33-45. doi:10.1042/AN20110059

180. Paluzzi S, Alloisio S, Zappettini S, et al. Adult astroglia is competent for Na+/Ca2+ exchanger-operated exocytotic glutamate release triggered by mild depolarization. *J Neurochem*. 2007;103(3):1196-1207. doi:10.1111/J.1471-4159.2007.04826.X

181. Boddum K, Jensen TP, Magloire V, et al. Astrocytic GABA transporter activity modulates excitatory neurotransmission. *Nat Commun*. 2016;7:1-10. doi:10.1038/ncomms13572

182. Catterall WA. Voltage-Gated Calcium Channels. *Cold Spring Harb Perspect Biol*. 2011;3(8):1-23. doi:10.1101/CSHPERSPECT.A003947

183. Yaguchi T, Nishizaki T. Extracellular high K+ stimulates vesicular glutamate release from astrocytes by activating voltage-dependent calcium channels. *J Cell Physiol*. 2010;225(2):512-518. doi:10.1002/JCP.22231

184. De Balderas PMO, Aguilera P. A Metabotropic-Like Flux-Independent NMDA Receptor Regulates Ca2+ Exit from Endoplasmic Reticulum and Mitochondrial Membrane Potential in Cultured Astrocytes. *PLoS One*. 2015;10(5). doi:10.1371/JOURNAL.PONE.0126314

185. Gérard F, Hansson E. Inflammatory activation enhances NMDA-triggered Ca2+ signalling and IL-1β secretion in primary cultures of rat astrocytes. *Brain Res*. 2012;1473:1-8. doi:10.1016/J.BRAINRES.2012.07.032

186. Hu B, Sun SG, Tong ET. NMDA and AMPA receptors mediate intracellular calcium increase in rat cortical astrocytes. *Acta Pharmacol Sin*. 2004;25(6):714-720. http://www.chinaphar.com/1671-4083/25/714.htm. Accessed June 13, 2022.

187. Zhang Q, Hu B, Sun S, Tong E. Induction of increased intracellular calcium in astrocytes by glutamate through activating NMDA and AMPA receptors. *J Huazhong Univ Sci Technolog Med Sci*. 2003;23(3):254-257. doi:10.1007/BF02829506

188. Helmchen F, Imoto K, Sakmann B. Ca2+ buffering and action potential-evoked Ca2+ signaling in dendrites of pyramidal neurons. *Biophys J*. 1996;70(2):1069. doi:10.1016/S0006-3495(96)79653-4

189. Lütcke H, Murayama M, Hahn T, et al. Optical recording of neuronal activity with a genetically-encoded calcium indicator in anesthetized and freely moving mice. *Front Neural Circuits*. 2010;4(APR). doi:10.3389/FNCIR.2010.00009

190. O'Connor DH, Peron SP, Huber D, Svoboda K. Neural activity in barrel cortex underlying vibrissa-based object localization in mice. *Neuron*. 2010;67(6):1048-1061. doi:10.1016/J.NEURON.2010.08.026

191. Sakata S, Harris KD. Laminar structure of spontaneous and sensory-evoked population

activity in auditory cortex. *Neuron*. 2009;64(3):404-418. doi:10.1016/J.NEURON.2009.09.020

192. Hebb, D. O. Organization of behavior. New York: Wiley, 1949, pp. 335, $4.00 - 1950 - Journal of Clinical Psychology - Wiley Online Library.

193. Shoham S, O'Connor DH, Segev R. How silent is the brain: is there a "dark matter" problem in neuroscience? *J Comp Physiol A 2006 1928*. 2006;192(8):777-784. doi:10.1007/S00359-006-0117-6

194. Brecht M, Schneider M, Manns ID. Silent Neurons in Sensorimotor Cortices: Implications for Cortical Plasticity. - PsycNET. *F F Ebner (Ed), Neural Plast adult Somat sensory-motor Syst*. 2005:1-19. https://psycnet.apa.org/record/2005-16432-001. Accessed June 13, 2022.

195. Avermann M, Tomm C, Mateo C, Gerstner W, Petersen CCH. Microcircuits of excitatory and inhibitory neurons in layer 2/3 of mouse barrel cortex. *J Neurophysiol*. 2012;107(11):3116-3134. doi:10.1152/JN.00917.2011/ASSET/IMAGES/LARGE/Z9K0111213530008.JPEG

196. Holmgren C, Harkany T, Svennenfors B, Zilberter Y. Pyramidal cell communication within local networks in layer 2/3 of rat neocortex. *J Physiol*. 2003;551(Pt 1):139. doi:10.1113/JPHYSIOL.2003.044784

197. Adesnik H, Bruns W, Taniguchi H, Huang ZJ, Scanziani M. A Neural Circuit for Spatial Summation in Visual Cortex. *Nature*. 2012;490(7419):226. doi:10.1038/NATURE11526

198. Atallah B V., Bruns W, Carandini M, Scanziani M. Parvalbumin-expressing interneurons linearly transform cortical responses to visual stimuli. *Neuron*. 2012;73(1):159-170. doi:10.1016/J.NEURON.2011.12.013

199. Gentet LJ, Avermann M, Matyas F, Staiger JF, Petersen CCH. Membrane potential dynamics of GABAergic neurons in the barrel cortex of behaving mice. *Neuron*. 2010;65(3):422-435. doi:10.1016/J.NEURON.2010.01.006

200. Yu J, Hu H, Agmon A, Svoboda K. Recruitment of GABAergic Interneurons in the Barrel Cortex during Active Tactile Behavior. *Neuron*. 2019;104(2):412-427.e4. doi:10.1016/J.NEURON.2019.07.027

201. Sachidhanandam S, Sermet BS, Petersen CCH. Parvalbumin-Expressing GABAergic Neurons in Mouse Barrel Cortex Contribute to Gating a Goal-Directed Sensorimotor Transformation. *Cell Rep*. 2016;15(4):700-706. doi:10.1016/J.CELREP.2016.03.063

202. Fino E, Yuste R. Dense inhibitory connectivity in neocortex. *Neuron*. 2011;69(6):1188. doi:10.1016/J.NEURON.2011.02.025

203. Kapfer C, Glickfeld LL, Atallah B V., Scanziani M. Supralinear increase of recurrent inhibition during sparse activity in the somatosensory cortex. *Nat Neurosci*. 2007;10(6):743. doi:10.1038/NN1909

204. Lee S, Kruglikov I, Huang ZJ, Fishell G, Rudy B. A disinhibitory circuit mediates motor integration in the somatosensory cortex. *Nat Neurosci 2013 1611*. 2013;16(11):1662-1670. doi:10.1038/NN.3544

205. Pala A, Petersen CCH. State-dependent cell-type-specific membrane potential dynamics and unitary synaptic inputs in awake mice. *Elife*. 2018;7. doi:10.7554/ELIFE.35869

206. Karnani MM, Jackson J, Ayzenshtat I, et al. Opening Holes in the Blanket of Inhibition: Localized Lateral Disinhibition by VIP Interneurons. *J Neurosci*. 2016;36(12):3471. doi:10.1523/JNEUROSCI.3646-15.2016

207. Pfeffer CK, Xue M, He M, Huang ZJ, Scanziani M. Inhibition of inhibition in visual cortex: the logic of connections between molecularly distinct interneurons. *Nat Neurosci 2013 168*. 2013;16(8):1068-1076. doi:10.1038/NN.3446

208. Pi HJ, Hangya B, Kvitsiani D, Sanders JI, Huang ZJ, Kepecs A. Cortical interneurons that specialize in disinhibitory control. *Nat 2013 5037477*. 2013;503(7477):521-524. doi:10.1038/NATURE12676

209. Sachidhanandam S, Sreenivasan V, Kyriakatos A, Kremer Y, Petersen CCH. Membrane potential correlates of sensory perception in mouse barrel cortex. *Nat Neurosci 2013 1611*. 2013;16(11):1671-1677. doi:10.1038/NN.3532

210. Poulet JFA, Petersen CCH. Internal brain state regulates membrane potential synchrony in barrel cortex of behaving mice. *Nat 2008 4547206*. 2008;454(7206):881-885. doi:10.1038/NATURE07150

211. Kyriakatos A, Sadashivaiah V, Zhang Y, Motta A, Auffret M, Petersen CCH. Voltage-sensitive dye imaging of mouse neocortex during a whisker detection task. *Neurophotonics*. 2017;4(3):031204. doi:10.1117/1.NPH.4.3.031204

212. Kerkhofs A, Canas PM, Timmerman AJ, et al. Adenosine A2A receptors control glutamatergic synaptic plasticity in fast spiking interneurons of the prefrontal cortex. *Front Pharmacol*. 2018;9(MAR):133. doi:10.3389/FPHAR.2018.00133/BIBTEX

213. Manzoni OJ, Manabe T, Nicoll RA. Release of adenosine by activation of NMDA receptors in the hippocampus. *Science*. 1994;265(5181):2098-2101. doi:10.1126/SCIENCE.7916485

214. Newman EA. Glial Cell Inhibition of Neurons by Release of ATP. *J Neurosci*. 2003;23(5):1659-1666. /pmc/articles/PMC2322877/. Accessed March 6, 2020.

215. Zhang JM, Wang HK, Ye CQ, et al. ATP Released by Astrocytes Mediates Glutamatergic Activity-Dependent Heterosynaptic Suppression. *Neuron*. 2003;40(5):971-982. doi:10.1016/S0896-6273(03)00717-7

216. Rombo DM, Newton K, Nissen W, et al. Synaptic mechanisms of adenosine A2A receptor-mediated hyperexcitability in the hippocampus. *Hippocampus*. 2015;25(5):566-580. doi:10.1002/HIPO.22392

217. Zhang P, Bannon NM, Ilin V, Volgushev M, Chistiakova M. Adenosine effects on inhibitory synaptic transmission and excitation-inhibition balance in the rat neocortex. *J Physiol*. 2015;593(4):825-841. doi:10.1113/JPHYSIOL.2014.279901

218. Lalo U, Palygin O, Verkhratsky A, Grant SGN, Pankratov Y. ATP from synaptic terminals and astrocytes regulates NMDA receptors and synaptic plasticity through PSD-95 multi-protein complex. *Sci Rep*. 2016;6(May):1-20. doi:10.1038/srep33609

219. Chistiakova M, Volgushev M. Heterosynaptic plasticity in the neocortex. *Exp Brain Res*. 2009;199(3):377. doi:10.1007/S00221-009-1859-5

220. Chistiakova M, Ilin V, Roshchin M, et al. Distinct Heterosynaptic Plasticity in Fast Spiking and Non-Fast-Spiking Inhibitory Neurons in Rat Visual Cortex. *J Neurosci*.

2019;39(35):6865-6878. doi:10.1523/JNEUROSCI.3039-18.2019

221. Feldman DE. Synaptic Mechanisms for Plasticity in Neocortex. *Annu Rev Neurosci*. 2009;32:33. doi:10.1146/ANNUREV.NEURO.051508.135516

222. Kourosh-Arami M, Hosseini N, Komaki A. Brain is modulated by neuronal plasticity during postnatal development. *J Physiol Sci*. 2021;71(1):1-16. doi:10.1186/S12576-021-00819-9/TABLES/1

223. Volgushev M, Chen JY, Ilin V, Goz R, Chistiakova M, Bazhenov M. Partial Breakdown of Input Specificity of STDP at Individual Synapses Promotes New Learning. *J Neurosci*. 2016;36(34):8842. doi:10.1523/JNEUROSCI.0552-16.2016

224. Carcea I, Froemke RC. Cortical Plasticity, Excitatory–Inhibitory Balance, and Sensory Perception. *Prog Brain Res*. 2013;207:65. doi:10.1016/B978-0-444-63327-9.00003-5

225. Wang Q, Kong Y, Wu D-Y, et al. Impaired calcium signaling in astrocytes modulates autism spectrum disorder-like behaviors in mice. *Nat Commun*. 2021;12(1). doi:10.1038/s41467-021-23843-0

226. Balderas PM de O, GonzálezHernández JR. NMDA Receptors in Astroglia: Chronology, Controversies, and Contradictions from a Complex Molecule. *Astrocyte - Physiol Pathol*. March 2018. doi:10.5772/INTECHOPEN.72975